Hydrodynamics and Sediment Transport at the River-Ocean Interface: Analytical and Laboratory Investigations

Anthony Poggioli

A dissertation
submitted in partial fulfillment of the
requirements for the degree of

Doctor of Philosophy

University of Washington

2015

Reading Committee:

Alexander R. Horner-Devine, Chair

James Thomson

Peter Rhines

Program Authorized to Offer Degree:
Civil & Environmental Engineering

University of Washington

Abstract

Hydrodynamics and Sediment Transport at the River-Ocean Interface: Analytical and Laboratory Investigations

Anthony Poggioli

Chair of the Supervisory Committee:
Allan and Inger Osberg Associate Professor Alexander R. Horner-Devine
Civil & Environmental Engineering

This study presents a combination of numerical and analytical investigations of fluid and sediment transport mechanics through the river-ocean interface. This region is defined broadly as the region within the river that is influenced by the receiving basin–both the salinity and the oscillating and mean basin heights–as well as the portion of the river influenced by the presence of a distinct fluvial buoyant water mass. More narrowly, we consider in this study an atidal salt wedge, the upstream hydraulic transition zone in the unstratified river, and the near-field river plume.

The first main chapter presents a hydraulic model of the salt wedge estuary in sloped and landward-converging channels. It is found that the non-dimensionalized intrusion length is a function of the freshwater Froude number F_f, as noted in previous studies, as well as new parameters describing the channel geometry. Further, it is found that the primary geometric influence on the intrusion length is the channel bottom slope. Comparison to field data is given indicating that the influence of nonzero bottom slope may account for the discrepancy between observation and the canonical flat estuary theory (Schijf & Schönfeld, 1953).

Next, we link our hydraulic model of the salt wedge to a hydraulic model of the upstream river transition zone, which is influenced by the depth of the receiving basin and is not in normal flow. We add to this a parameterization of total sediment transport in the unstrat-

ified river (Engelund & Hansen, 1967) and a newly developed hydraulic model of sediment transport in the salt wedge. The model retains the key mechanistic features of sediment transport in highly stratified estuaries and is ideal for morphodynamic applications. We find that the principle influence of the salt wedge is an increase in net deposition in the lower river and the introduction of a secondary maximum aggradation length scale in addition to the backwater length discussed in Chatanantavet *et al.* (2012).

Finally, we present experimental simulations of the steady state estuary and river plume. The results of the estuary experiments quantify the influence of bottom slope on the reduction of sensitivity of intrusion length to river discharge and confirm the results of the hydraulic model. The plume experiments indicate that the plume transitions to a jet-like outflow for sufficiently large values of F_f in which the spreading rate is determined by lateral entrainment instead of the plume buoyancy and the liftoff is pushed far offshore. This transition is not gradual but rather step-like, being concentrated on one value (or a narrow band of values of) F_f. Both this critical value of F_f and the jet spreading rate depend crucially on the plume inflow aspect ratio. This jet-like behavior is anticipated to have crucial implications for delta progradation processes and the magnitude of sediment erosion in the lower river during flood events.

TABLE OF CONTENTS

LIST OF FIGURES

LIST OF TABLES

ACKNOWLEDGMENTS

First and foremost, I should thank my advisor, Alex Horner-Devine. Every one of Alex's students has remarked to me at one time or another, and I to them, how undoubtedly lucky we were to end up with Alex as a mentor. I know of no one else possessing such a confluence of intelligence, patience, passion, and good nature. He has always made himself available to me, whenever need be, whatever my issue, and with undoubted expertise. For teaching me how to be a scientist, I will be forever grateful to him.

I thank also my committee, Jim Thomson, Parker MacCready, Peter Rhines, and Jim Riley. Each member of my committee has provided to me at one time or another invaluable guidance, whether it be in research, in coursework, or in life. Particular thanks to Jim Thomson for consistently asserting my accomplishments as a researcher (I still don't think I'm half as competent as he seems to), Peter Rhines for stepping in during a last minute pinch, and Jim Riley for numerous conversations on various subjects, endlessly fruitful for myself.

Thank you as well to the Environmental Fluid Mechanics Group at UW. I should like to single out everyone in the group, because they have all at one time or another provided me with guidance in research or on a problem set, or just a welcome distraction from the unparalleled joy of sustained contemplation of the nature of highly stratified estuaries. But I will settle to single out only one member, Maggie McKeon, who has been a colleague and a friend. Her insights, particularly on the first paper contained in this thesis, were formative.

I have to also thank several undergraduate students who at various times helped me with construction, experiments, data processing, coding, and calculation: James Neher, Rick Punt, Noah Johnson, Robert Gunn, and Lexie England. In particular, I want to thank James,

Noah, and Lexie, who were tireless in their efforts and showed an uncanny precociousness for advanced research. I could never have done this in the time that I did without their help.

Finally, I thank my friends and family: My sisters, Melissa and Megan, my father Robert, my stepmother Darlene, my mother Lori, and my grandparents Joyce and Robert. There's little I can say to express my gratitude to them, but I will say that their unwavering support of all of my endeavours, as well as the occasional reminder that I'm not so smart really, meant the world to me.

Reflecting back on my time as a graduate student at UW, I can't help but feel what everyone must feel at this point in their graduate career: I'd very much like to do it all over again, but this time in French. (That's an inside joke.)

DEDICATION

To my mother

Chapter 1

INTRODUCTION

The river-ocean interface comprises the lower reaches of the unstratified river, the estuary, and the buoyant plume that forms in the coastal ocean. It is illustrated schematically in Figure 1.1. A detailed understanding of the dynamics of this region has important consequences for human life on both short and long timescales. Rivers deliver freshwater, biology, and terrestrial nutrients, contaminants, and sediment to the coastal ocean, altering the structure and productivity of coastal ecosystems. Riverine water introduces stratification into estuaries and coastal oceans, inhibiting the vertical transport of, e.g., nutrients and oxygen, and generates circulation that alters and inhibits transport pathways and the distribution of biology along the coast (Hickey *et al.*, 2010). The flow in this region ultimately determines the net deposition of sediment in the lower river, as well as the sediment export to the coastal shelf, and acts as a fundamental control on both deltaic and continental sedimentation (Syvitski & Saito, 2007; Syvitski *et al.*, 2009). Additionally, the dynamics of river-ocean interaction has important implications for global circulation and climate modeling, the nature of freshwater delivery from rivers to oceans being a key unknown in these models with potentially dramatic influences on predicted long term impacts of anthropogenic stresses on the climate system (e.g., Hordoir *et al.*, 2008).

Forty-four percent of the global population lives within 150 kilometers of a coast, and this proportion is increasing at an accelerating rate (UN-OCEANS, n.d.). As human populations migrate to densely packed urban regions near coasts and estuaries, the anthropogenic pressures on these environments increases: the natural topography of estuaries is altered and repurposed to suit urban demands, the rate of waste discharge (e.g., sewage) to rivers

and estuaries increases, and the demand on the coastal ecosystem is increased. Additionally, as agricultural activity expands to suit a growing population, the nutrient loading to rivers grows. Together, these anthropogenic pressures act to shape and alter coastal ecosystems, which are biologically diverse and highly productive, and a primary source of human food supplies. The manner in which increased anthropogenic pressures will alter coastal ecosystems is determined by the hydrodynamics of the river-ocean interface. Rivers introduce stratification into estuaries and coastal oceans, inhibiting the vertical diffusion of oxygen, nutrients, contaminants, sediment, and biology, and the buoyant plumes formed by the discharge of relatively fresh estuarine water into the ocean introduce buoyancy forcing and induce a complex coastal circulation that entrains, supplies, and transports nutrients, contaminants, and biology, and alters ambient transport pathways along the coast and thus the distribution of biomass and productivity in shelf ecosystems (Hickey *et al.*, 2010).

On a longer time scale, it is recognized that the magnitude and manner of freshwater injection to the coastal ocean has an important effect on local circulation that is not accounted for suitably in current general ocean circulation (GOCMs) and global climate models (GCMs) (Hordoir *et al.*, 2008). GCMs are sensitive to both the amount and the location of freshwater injection, making quantification of freshwater delivery from the river to the coastal ocean, as well a more complete understanding of the dynamics of river-ocean interaction as it determines the location of freshwater injection, an important step in improving climate forecasting. It has been shown by, e.g., Rahmstorf (1995) that deep water convection in the ocean is sensitive to even small fluctuations in freshwater delivery to the ocean, with the location of injection determining the manner in which the convection cell is disrupted or altered as well as the time scale of adjustment associated with the disruption. Thus, a more complete understanding of the pathway of terrestrial freshwater as it is delivered to the coastal ocean is crucial to improving our understanding of the evolution of the climate system.

The river-ocean interface is a transitional zone between river and marine transport processes, and it determines the ultimate fate of fluvial sediment. The imbalance between

delivery of sediment to this region and ultimate export to the shelf determines the volume of material available for bed and land surface evolution, influencing its susceptibility to inundation from river flooding, subsidence, and sea level rise (Syvitski & Saito, 2007; Syvitski *et al.*, 2009). Additionally, this flux imbalance, and the distribution of sediment deposition in the lower river, is a key control on the processes of delta formation and growth (Jerolmack, 2009; Chatanantavet *et al.*, 2012; Lamb *et al.*, 2012). Furthermore, the net export of sediment from the river mouth provides active sediment to the shelf and is thus a control on continental sedimentation (e.g., Blum & Törnqvist, 2000). An understanding of the sediment dynamics through this region is crucial for understanding the threat posed to coastal human communities by the catastrophic inundation, as well as the morphological evolution of the river, delta, and continental shelf. The fundamental hydrodynamic questions investigated in this thesis are motivated by, and ultimately applied to (see especially Chapter 3), basic questions about the sediment transport in this region and how it affects the long term morphological evolution of the river.

1.0.1 Definition of the River-Ocean Interface

The river-ocean interface is defined in this thesis to be comprised of the lower reaches of the unstratified river, which are influenced hydraulically by the coastal ocean but are upstream of the estuary; the estuary, which is the region of density-driven salt water penetration into the river; and the buoyant plume that forms seaward of the river mouth. The river plume can be further subdivided into three regions: an energetic near-field region, characterized by a relative insensitivity of the discharging buoyant water to forcing from winds, ambient coastal circulation, and earth's rotation; a far-field, which is an along-coast geostrophic current that ultimately transports freshwater away from the mouth; and the mid-field, a retentive anticyclonic gyre that forms near the river mouth and mediates delivery of water from the estuary to the geostrophic current (Horner-Devine *et al.*, 2009). Each of these regions is illustrated schematically in Figure 1.1. The present study focuses only on the near-field plume, for two reasons. First, this region contributes significantly to the transformation of

the water mass as it passes from the river ultimately to the far-field plume (Hetland, 2010). Ultimately, getting the dynamics in this region right is crucial for predicting the ultimate fate of riverine freshwater. Secondly, this region is directly linked to the estuary and lower river and therefore it is the dynamic feedback between the lower river and near-field plume that ultimately influences the flux of sediment from the river to the coastal ocean.

We further limit this study by concentrating only on estuaries with high vertical stratification, typically referred to as salt wedges. Such estuaries are formed when river forcing, which introduces stratification into the estuary, dominates over tidal forcing, which generates mixing that tends to destroy stratification (e.g., Geyer & MacCready, 2014). There are two reasons to do this: First, we are interested primarily in the influene of the dynamics of the river-ocean interface on sediment deposition in the lower river and delivery to the shelf. This is most important when sediment flux is large which, like the maintenance of vertical stratification in the estuary, is associated with high river volume (e.g. Nash, 1994). And second, there are interesting hydrodynamic questions associated with salt wedge estuary that in themselves motivate a consideration of their dynamics (see Chapter 2).

1.0.2 Layout of the Thesis

In Chapter 2, we present a hydraulic description of the salt wedge in sloping and converging channels. The results of this section address a discrepancy between the theoretical prediction for the intrusion length of salt water into the river and field observations, and our results indicate that this discrepancy can be resolved by considering the influence of channel bottom slope. Getting the intrusion length and structure of the salt wedge right was a necessary first step for Chapter 3, which presents a simple model of the sediment dynamics in the estuary that is appropriate for incorporation in hydraulic models of the river morphology (e.g. Lamb *et al.*, 2012). We then use this model to quantify the influence of salt wedge formation on the volume and distribution of deposition in the lower river, as well as on export to the shelf. Finally, in Chapter 4, we detail experimental work that confirms our theory for the structure of the salt wedge and extends our results to the high discharge case, for which the estuary

is expelled from the river channel and the sediment dynamics become highly dependent on the structure of the near-field river plume. Concluding remarks and recommendations for further work are presented in Chapter 5.

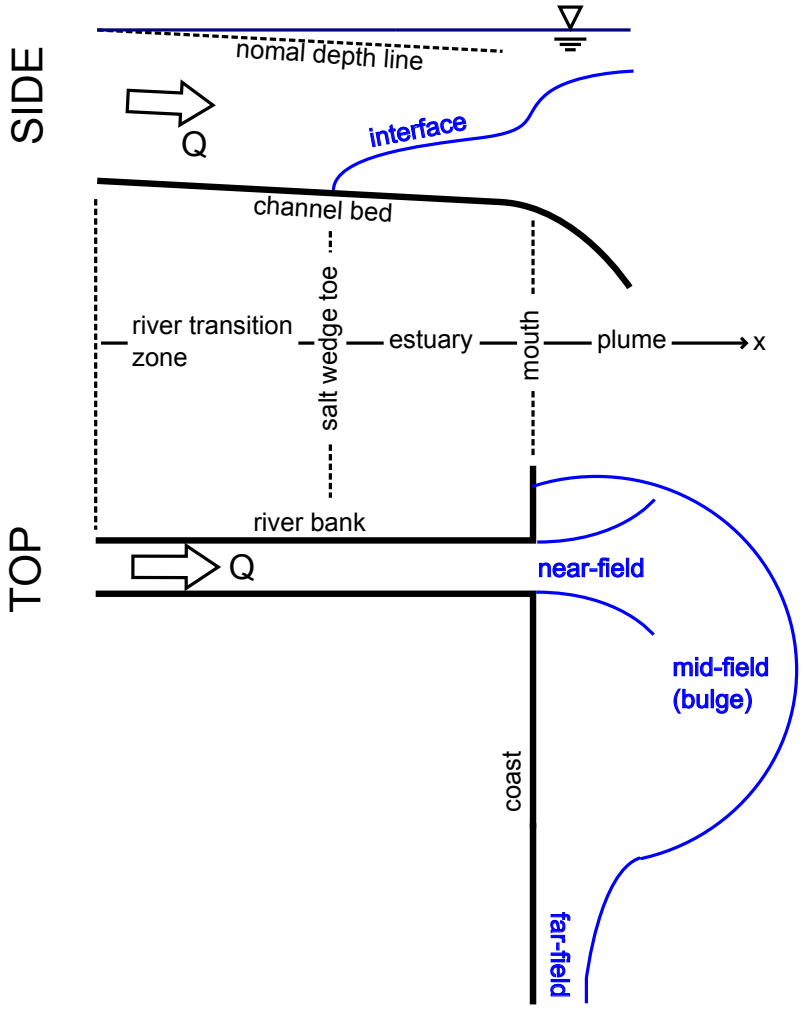

Figure 1.1: A schematic illustrating the river-ocean interface, comprising the hydraulic transition zone of the lower river, the estuary, and the buoyant river plume that forms seaward of the river mouth, in side (top) and plan view (bottom). The interface indicated in the figure is between fresh and saltwater. The plume can be further divided into the near-field, the initial energetic discharge region, relatively insensitive to rotational forcing and ambient coastal currents, a far-field, characterized by along-coast transport in geostrophic balance, and a transitional mid-field, characterized by the formation of a retentive anticyclonic gyre, the bulge. We focus here only on the near-field.

Chapter 2

SALT WEDGE HYDRAULICS IN SLOPING AND CONVERGING ESTUARIES

2.1 Introduction

A salt wedge forms when an estuary is dominated by the stratifying influence of a freshwater inflow, in opposition to the vertically homogenizing influence of tides (Geyer & MacCready, 2014). Salt wedges are characterized by strong vertical stratification confined to a narrow pycnocline, which divides a nearly fresh layer of out-flowing water from the layer of ocean water beneath it (Geyer & Ralston, 2011). The dynamics of this flow are described effectively by two layer hydraulic theory as developed by Armi (1986) and others, perhaps modified by the inclusion of bottom and/or interfacial friction as described by, e.g., Schijf & Schönfeld (1953); Pratt (1986); Geyer & Farmer (1989); Geyer & Ralston (2011). The lower layer propagates upstream under the influence of the baroclinic pressure gradient until it is arrested by an adverse net barotropic flow in the presence of variable topography and/or interfacial friction. The structure of the salt wedge varies depending on whether it is arrested by barotropic forcing or interfacial friction. The dynamics of frictionless barotropic arrest of a salt wedge in a diverging channel upstream of a constriction are described by Armi & Farmer (1986), and those of a frictionally arrested salt wedge in a prismatic channel are described by Schijf & Schönfeld (1953). Here we describe the dynamics of an arrested salt wedge under the influence of both friction and variable topography.

Schijf & Schönfeld (1953) develop an analytical theory for the structure of a frictionally arrested salt wedge in a flat channel of uniform width. They derive an explicit formula for the intrusion length as a function of river discharge (a length-discharge relationship), and their model is used by Harleman (1961) to obtain an implicit expression for the shape of

the intrusion. Over much of the relevant parameter space, the length-discharge relationship they derive predicts $L \sim Q^{-2\ to\ -2.5}$ (Geyer & Ralston, 2011). Keulegan (1966) finds experimentally that for a flat channel of uniform width L varies with $Q^{-2.5}$, and Harleman (1961) shows that the analytical expression he derives for the shape of the salt wedge agrees with the experimental profiles reported by Keulegan (1957). This model thus appears to correctly describe the physics of the frictionally arrested salt wedge, at least in the absence of topographic variation. However, in real salt wedges, the dependence of L on Q, typically quantified by the exponent n in a power law relationship of the form $L \sim Q^{-n}$, is consistently observed to be an order-of-magnitude smaller than the canonical values discussed above. This is illustrated in Figure 2.1, which shows field [Fraser, from Ward (1976), and Duwamish, from McKeon *et al.* (2014)] and validated realistic numerical model [Merrimack, from Ralston *et al.* (2010)] data, along with the best-fit power law and corresponding exponent for each data set. The power law exponent varies between 0.18 and 0.49 and is always much smaller than the $n = 2$ exponent from Schijf & Schönfeld (1953). The primary goal of this work is to determine if topographic effects–in particular a non-zero mean bottom slope and/or upstream convergence of channel width–may explain the deviation of observation from the solution for a flat, prismatic estuary due to Schijf & Schönfeld (1953).

In most estuaries, the structure of the salt wedge is strongly modified by tidal currents (e.g., Geyer & Farmer, 1989). The quasi-steady arrested layer model of the salt wedge is an accurate description of the wedge at arrest, occurring soon after the upper layer begins to ebb (Geyer & Farmer, 1989). The length predicted is thus an indication of the maximum intrusion. However, the arresting discharge must then be understood as the sum of the fluvial and an effective tidal discharge (Geyer & Ralston, 2011). The prediction of hydraulic theory for the dependence of intrusion length on tidal amplitude as well as river discharge can only be found using a more sophisticated time-dependent model of the estuary. However, the work presented here will give a qualitative indication of the sensitivity of salt wedge length to river discharge in tidal systems, and we hope that the results will serve to indicate whether the discrepancy between observation and theory is a result of a breakdown in the

assumed physics [e.g., a transition from the hydraulic to a partially mixed regime dominated by exchange flux, for which $L \sim Q^{-1/3}$ (Chatwin, 1976; Monismith *et al.*, 2002; MacCready & Banas, 2011)] or an oversimplification in the application of the hydraulic equations.

In Section 2.2, we present an overview of the theory of hydraulic descriptions of the estuary, developing equations and boundary conditions governing the structure of the two layered arrested salt wedge, and determine the principle governing dimensionless parameters. Section 2.3 briefly reviews the analytical results of Schijf & Schönfeld (1953) and Harleman (1961) for the length and structure of a frictionally arrested salt wedge in a flat, prismatic channel, which is the canonical theory for the sensitivity of intrusion length to discharge to which we will compare our results. In Section 2.4, we present the results for the dependence of intrusion length on discharge in a sloped channel of uniform width, and in Section 2.5, those for the dependence of intrusion length on discharge in an exponentially converging estuary of both zero and non-zero bottom slope. In Section 4.5, we compare our results for the dependence of intrusion length on river discharge to a numerically modeled L versus Q relationship in the Merrimack River estuary and a measured L versus Q relationship in the Duwamish River estuary–see Figure 2.1–and discuss some key implications of this work.

2.2 Theory

Following Schijf & Schönfeld (1953), we develop a frictional two layer hydraulic model of the salt wedge. A freshwater layer with uniform velocity varying only in the along-flow direction passes without mixing over a uniform, stationary layer of ocean water, the salt wedge. Figure 2.2 shows the geometry of this configuration; in general, a subscript 1 indicates a quantity in the buoyant layer, and a subscript 2 indicates a quantity in the salt wedge. We drop the subscript 1 on the velocity u because only the upper layer is flowing. Tides are not considered, and the river discharge is assumed steady. The model is one-dimensional, and the effects of lateral topographic variation on the flow are included only in the continuity equation. We parameterize the interfacial shear stress τ_i using a quadratic drag coefficient

C_i that is assumed constant, such that

$$\tau_i = C_i \rho u^2, \tag{2.1}$$

where ρ is the density, and u is the upper layer velocity. The difference in the value of C_i depending on whether the upper or lower layer density is used in Equation 2.1 is neglected, given the small density differences in estuarine applications. The momentum and continuity equations are

$$q \equiv \frac{Q}{b} = u h_1 \tag{2.2}$$

$$u\frac{du}{dx} + g\frac{d\eta}{dx} + C_i\frac{u^2}{h_1} = 0 \tag{2.3}$$

$$g\frac{d\eta}{dx} - g'\frac{dh_1}{dx} - C_i\frac{u^2}{h_2} = 0, \tag{2.4}$$

where q is the specific river discharge, Q is the river discharge, b is the channel width, assumed invariant with depth, $\eta = h_1 + h_2 + h_b$ is the free surface elevation, h_j is the thickness of the j-th layer, h_b is the channel bottom elevation, g is gravitational acceleration, $g' \equiv (\Delta\rho/\rho_2)\, g$ is reduced gravitational acceleration, and $\Delta\rho \equiv \rho_2 - \rho_1$ is the density anomaly. These correspond to the equations developed by Schijf & Schönfeld (1953) with the time derivatives and lower layer velocity set to zero and the upper layer continuity equation integrated over x. Note that these equations apply only within the salt wedge and not upstream.

If Equations 2.2 through 2.4 are solved for dh_1/dx and dh_2/dx and integrated, there are numerical difficulties associated with rapidly varying topography because the gradients of the topographic variables appear explicitly. Additionally, the resulting equations become unbounded when the upper layer internal Froude number $F_{i1} = Q/b\sqrt{g' h_1^3} = 1$. This happens at the hydraulic control, where integration begins–see Section 2.2.1. For these reasons, it is useful to combine the momentum and continuity equations and rewrite the result in terms of the buoyant hydraulic head:

$$\frac{d}{dx}\left[\frac{Q^2}{2g' b^2 h_1^2} + \left(\frac{\Delta\rho}{\rho_2}\right)^{-1}\eta\right] = \frac{dH_1'}{dx} = -C_i F_{i1}^2 \tag{2.5}$$

$$\frac{d}{dx}\left[\left(\frac{\Delta\rho}{\rho_2}\right)^{-1}\eta - h_1\right] = \frac{dH_2'}{dx} = C_i F_{i1}^2 \frac{h_1}{h_2}, \tag{2.6}$$

where H_j' is the buoyant hydraulic head of the j-th layer. An equation eliminating the free surface slope is obtained by taking the difference of Equations 2.5 and 2.6:

$$\frac{d}{dx}\left(\frac{Q^2}{2g'b^2h_1^2} + h_1\right) = \frac{d\Delta H'}{dx} = -C_i F_{i1}^2 \left(1 + \frac{h_1}{h_2}\right), \tag{2.7}$$

where $\Delta H' \equiv H_1' - H_2'$ is here termed the buoyant hydraulic head anomaly. Our solution procedure, explained in Section 2.2.3 below, will be to integrate for H_1' and $\Delta H'$ and then solve for the layer thicknesses.

2.2.1 Boundary Conditions

We follow Schijf & Schönfeld (1953) in assuming that the mouth is the control–i.e., the flow is critical ($F_{i1}^2 = 1$) there–in the absence of varying channel topography. However, if there are significant lateral constrictions present in the estuary, the relevant control may be a channel constriction and not the river mouth. This is because flow constrictions satisfy the regularity conditions, which are necessary local topographic conditions (e.g., $db/dx = 0$) for the existence of a hydraulic control (Armi, 1986).

Denoting the location of the control as $x = 0$, the first boundary condition, that $F_{i1}^2 = 1$, can be written as

$$h_1(x=0) = h_{1c}(x=0) = h_{1c0} = \left(\frac{Q^2}{b_0^2 g'}\right)^{1/3}, \tag{2.8}$$

where h_{1c} is the critical thickness, the thickness of the upper layer when $F_{i1}^2 = 1$, h_{1c0} is the critical thickness at the control, and $b_0 = b(x=0)$ is the channel width at the control. A second boundary condition is obtained by assuming that the total water depth at the control h_S is known:

$$\eta(x=0) = h_S. \tag{2.9}$$

We refer to h_S as the shoreline depth because the control is typically at the mouth, where the channel intersects the coastal shoreline. This terminology follows Lamb *et al.* (2012),

who investigate in part the sensitivity of the shoreline depth to river discharge. We will not take into account the potential dependence of h_S on discharge here. The solutions presented in Sections 2.3 through 2.5 assume control occurs at the estuary mouth. When comparing to data obtained in the Duwamish (see Section 2.6.2) it will be necessary to identify controls associated with lateral constrictions and occurring at locations other than the mouth.

Together, these boundary conditions are sufficient to determine the values of the upper layer buoyant hydraulic head and hydraulic head anomaly at the control:

$$H_1'(x=0) = \frac{h_{1c0}}{2} + \left(\frac{\Delta\rho}{\rho_2}\right)^{-1} h_S = \frac{1}{2}\left(\frac{Q^2}{b_0^2 g'}\right)^{1/3} + \left(\frac{\Delta\rho}{\rho_2}\right)^{-1} h_S \tag{2.10}$$

$$\Delta H'(x=0) = \frac{3}{2} h_{1c0} = \frac{3}{2}\left(\frac{Q^2}{b_0^2 g'}\right)^{1/3}. \tag{2.11}$$

2.2.2 Non-Dimensionalization of Governing Equations

We now non-dimensionalize Equations 2.5 and 2.7 and Boundary Conditions 2.8 through 2.11. This will elucidate the governing dimensionless parameters and simplify the solution of this system of equations.

We non-dimensionalize all vertical length scales using the total water depth at the control, h_S. We will eliminate the free surface elevation η in favor of h_1 and h_2 using the general relation $\eta = h_1 + h_2 + h_b$. We do this to reduce the number of dependent hydraulic variables to two: h_1 and h_2. We non-dimensionalize all horizontal length scales by the so-called friction length (Geyer & Ralston, 2011), h_S/C_i, the buoyant hydraulic heads by the critical depth at the control h_{1c0}, and the channel width b by the width at the control b_0. We denote dimensionless variables by a subscript $*$. A list of the dimensioned and corresponding non-dimensionalized independent and dependent model variables is shown in Table 2.1. This procedure results in the following equations:

$$H_{1*}' = \frac{1}{2}\frac{F_f^{4/3}}{b_*^2 h_{1*}^2} + \frac{1}{F_f^{2/3}}\left(\frac{\Delta\rho}{\rho_2}\right)^{-1}(h_{1*} + h_{2*} + h_{b*}) \tag{2.12}$$

$$\Delta H'_* = \frac{1}{2}\frac{F_f^{4/3}}{b_*^2 h_{1*}^2} + \frac{h_{1*}}{F_f^{2/3}} \tag{2.13}$$

$$\frac{dH'_{1*}}{dx_*} = -\frac{F_f^{4/3}}{b_*^2 h_{1*}^3} \tag{2.14}$$

$$\frac{d\Delta H'_*}{dx_*} = -\frac{F_f^{4/3}}{b_*^2 h_{1*}^3}\left(1 + \frac{h_{1*}}{h_{2*}}\right) \tag{2.15}$$

$$h_{1*}\left(x_* = 0\right) = F_f^{2/3} \tag{2.16}$$

$$h_{1*}\left(x_* = 0\right) + h_{2*}\left(x_* = 0\right) = 1 \tag{2.17}$$

$$H'_{1*}\left(x_* = 0\right) = \frac{1}{2} + \frac{1}{F_f^{2/3}}\left(\frac{\Delta\rho}{\rho_2}\right)^{-1} \tag{2.18}$$

$$\Delta H'_*\left(x_* = 0\right) = \frac{3}{2}. \tag{2.19}$$

We have defined the freshwater Froude number $F_f = Q/b_0\sqrt{g' h_S^3} = \left(h_{1c0}/h_S\right)^{3/2}$ (Geyer & Ralston, 2011). This number is equivalent to the non-dimensionalized net barotropic flow U_0 discussed in Armi (1986) and Armi & Farmer (1986); it is the key dynamical parameter governing two layer hydraulic flow.

By examining Equations 2.12 through 2.19, we conclude that the solution is in general a function of F_f, $\Delta\rho/\rho_2$, $b_*(x_*)$, and $h_{b*}(x_*)$. In Sections 2.4 and 2.5, when we investigate the behavior of this model in simple topographies, we will derive explicit geometric parameters that influence the solution.

2.2.3 Solution Methodology

The simplified geometry of the model domain is specified by an assumed topography, characterized by the non-dimensionalized channel bottom elevation and channel width as functions

of x_*. Boundary conditions 2.16 through 2.19 are applied at the control (assumed in Sections 2.3 through 2.5 to be the mouth), and Equations 2.14 and 2.15 are numerically integrated landward from the control using a second order method. At each step we solve Equation 2.13 for h_{1*} and then solve for h_{2*} by using Equation 2.12. When solving for h_{1*}, we choose the subcritical root because a supercritical solution would correspond to an upper layer thickness that decreases landward and therefore to an infinitely long salt wedge. We integrate until the point $x_* = -L_*$ where $h_{2*} = 0$ and the interface therefore intersects with the channel bottom. $L_* = C_i L/h_S$ is the non-dimensionalized intrusion or salt wedge length.

2.3 Solution for a Flat Estuary of Uniform Width

Before exploring the results of this model in non-uniform topographies, it is useful to rederive the results of Schijf & Schönfeld (1953) and Harleman (1961) for the shape and length of the salt wedge in a flat estuary of uniform width, since this is the canonical theory describing the structure of an arrested salt wedge. The above authors apply the rigid lid approximation, assuming that the along-estuary variation in the free surface elevation is negligible in the friction terms. The free surface slope term is not explicitly set to zero, however; this would produce inconsistent results if applied to the individual layer momentum equations. Rather, an equation eliminating the free surface slope must be obtained by taking the difference of the momentum equations before the rigid lid approximation can be applied.

In order to apply the rigid lid approximation, $h_{1*} + h_{2*} + h_{b*} = 1$, we must start with Equation 2.15 because it was obtained by taking the difference of the momentum equations. We insert Equation 2.13 into Equation 2.15, eliminate h_{2*} by applying the rigid lid approximation, and insert $h_{b*} = 0$ and $b_* = 1$, since the estuary is assumed to be flat and prismatic. After rearranging the result, we obtain

$$(1 - h_{1*}) \left(\frac{h_{1*}^3}{F_f^2} - 1 \right) \frac{dh_{1*}}{dx_*} + 1 = 0. \tag{2.20}$$

To obtain an explicit expression for the intrusion length, we integrate Equation 2.20,

using Boundary Condition 2.16 and the fact that at the toe $x_* = -L_*$ and $h_{1*} = 1$:

$$\int_1^{F_f^{2/3}} (1 - h_{1*}) \left(\frac{h_{1*}^3}{F_f^2} - 1 \right) dh_{1*} + \int_{-L_*}^0 dx_* = 0$$

$$\implies L_* = -\frac{1}{20} \left(6F_f^{4/3} - 15F_f^{2/3} - F_f^{-2} + 10 \right). \tag{2.21}$$

Equation 2.21 is equivalent to the expressions derived by Schijf & Schönfeld (1953) and Harleman (1961, Equation 26.22). It can be approximated by a power law of the form $L \sim Q^{-n}$, where n is always ≥ 2 and is < 2.5 over most of the relevant parameter space. These power laws are often cited in the literature (e.g., Lerczak *et al.*, 2009; Geyer & Ralston, 2011). This solution and these power laws are shown in Figure 2.3a. As noted earlier, however, n is observed to be an order of magnitude smaller in real systems, suggesting that the solution does not account for all of the relevant physics. An implicit expression for the shape of the salt wedge is derived by integrating from either the toe or the mouth to an arbitrary point $(x_*,\ h_{1*})$:

$$\int_1^{h_{1*}} (1 - h_{1*}) \left(\frac{h_{1*}^3}{F_f^2} - 1 \right) dh_{1*} + \int_{-L_*}^{x_*} dx_* = 0$$

$$\implies \frac{1}{20} F_f^{-2} \left(5h_{1*}^4 - 4h_{1*}^5 - 1 \right) + \frac{1}{2} \left(h_{1*}^2 + 1 \right) - h_{1*} + x_* + L_* = 0. \tag{2.22}$$

This is equivalent to the expression derived by Harleman (1961, Equation 26.21). The shape of the intrusion is plotted in Figure 2.3b. The Figure shows the salt wedge thickness normalized by the maximum thickness at the mouth, $h_2/(h_S - h_{1c0}) = (1 - h_{1*})/(1 - F_f^{2/3})$, versus $-x_*/L_* = -x/L$ for several values of F_f. The freshwater Froude number is constrained to be between zero and one; a value of $F_f > 1$ corresponds to a critical depth that is greater than the total water depth, in which case the salt wedge is completely expelled from the channel.

We noted above that, in addition to F_f, the solution is also a function of the non-dimensionalized density anomaly $\Delta\rho/\rho_2$. However, this parameter vanishes when we make

the rigid lid approximation. It can be shown that $d\eta/dx \sim O(C_i\Delta\rho/\rho_2)$, whereas $dh_1/dx \sim O(C_i)$ in the bulk of the salt wedge. Because $\Delta\rho/\rho_2$ is on the order of 0.01, this suggests that the change in upper layer thickness is dominated by the change in interface height, and therefore that neglecting changes in free surface elevation when calculating layer depths in the friction term is a good approximation. We anticipate that free surface effects will only become important for large values of $\Delta\rho/\rho_2$. We test this hypothesis by comparing a solution of Equations 2.14 and 2.15 for a flat estuary, which include all free surface effects, to Equation 2.21, which neglects free surface effects, for values of $\Delta\rho/\rho_2$ ranging from 0.001 to 0.025. This corresponds to a salinity difference ranging from 1.3 to 33.3 psu. The solution incorporating the influence of the changing free surface elevation on the layer thicknesses consistently predicted values of the intrusion length larger than the rigid lid solution of Schijf & Schönfeld (1953); however, the largest difference was less than 4% over this parameter range. Therefore, the differences due to free surface effects are of secondary importance compared with those resulting from the bottom slope and width variation (Sections 2.4 and 2.5), which result in predictions for L_* that deviate from Schijf & Schönfeld (1953) by orders-of-magnitude. In these Sections, we will ignore variation in $\Delta\rho/\rho_2$ in order to simplify our calculations and reduce the parameter space. We will assume a typical value of 0.02 corresponding to a salinity difference of 26.5 psu.

2.4 Solution for a Sloped Estuary of Uniform Width

In this section, we present the solution for the length-discharge relationship in a channel of uniform width and mean bottom slope α; see Figure 2.2. In this case, because the channel bottom elevation varies with x_*, it is not possible to explicitly solve a separable equation as we did for the flat, prismatic estuary, even if the rigid lid approximation is made. We therefore integrate Equations 2.14 and 2.15 numerically. In Figure 2.4 we present a comparison of the interface height predicted with the current solution with a sloped channel bottom ($C_i/\alpha = 10$) to that predicted by the Schijf & Schönfeld (1953) and Harleman (1961) solution for a flat estuary with the rigid lid approximation. The comparison illustrates that

the bottom slope has a dynamic effect on the salt wedge (modifying the baroclinic pressure gradient and interfacial friction, see Section 2.6.1), which significantly reduces the intrusion length relative to the flat bottom solution. We also observe that the discrepancy between the two solutions decreases as the river discharge increases. At the highest F_f, the intrusion lengths are close to equal, although differences in the interface and water surface profiles are evident (Figure 2.4e and f). The free surface profile upstream of the salt wedge is predicted using a typical open channel flow hydraulic model (see, e.g., Chow, 1959).

The assumed channel bottom elevation has the form $h_b = -\alpha x$. Applying the above non-dimensionalization to this expression produces $h_{b*} = -(\alpha/C_i)\, x_*$. This introduces a new variable into the dependence, C_i/α, which is the non-dimensional value of the slope-limited maximum intrusion length. Unlike the flat estuary case, in which the salt wedge may penetrate arbitrarily far upstream in the limit of small discharge, the intrusion in a sloped estuary is slope-limited as Q decreases. As $Q \to 0$ and the upper layer thickness at the mouth $\left[h_{1c0} = (q^2/g')^{1/3}\right]$ shrinks so that the initial wedge thickness approaches h_S, the intrusion length approaches a slope-limited value of h_S/α and L_* approaches C_i/α. This mechanism is discussed in detail in Section 2.6.1 and illustrated schematically in Figure 2.10a. We therefore anticipate that the family of $L_*(F_f)$ curves will branch depending on this limiting value of L_*, with the difference between curves becoming more pronounced as F_f becomes smaller and the limiting values of L_* are approached. This is observed in Figure 2.5, where we plot three L_* versus F_f solution curves for $C_i/\alpha = 0.1$, 1, 10, along with the Schijf & Schönfeld (1953) solution, which corresponds to a flat bed and therefore the limit $C_i/\alpha \to \infty$. Figure 2.5 confirms that L_* is a function of F_f, and C_i/α.

The value of the exponent n in Figure 2.5 corresponds to the slope of these curves because they are plotted in logarithmic space. We note from the discrepancy in slope between the Schijf & Schönfeld (1953) curve and those corresponding to finite values of C_i/α the strong dependence of n on C_i/α and therefore the mean bottom slope α. Also shown in Figure 2.5 are tangent lines corresponding to $n = 0.2$ and $n = 0.6$. These values of n were selected because they correspond approximately to the lower and upper limits reported in

the literature (Ralston *et al.*, 2010; McKeon *et al.*, 2014). The value of n predicted by the model is within the range observed in the field roughly for $0.01 < F_f < 0.1$. The exact range of F_f values that correspond to predicted n values coincident with those observed in the field is dependent on C_i/α. This range of freshwater Froude numbers is consistent with typical values observed in the field–see Section 4.5 and Figure 2.11b. Furthermore, typical values of C_i are on the order of 10^{-4} (Sorgard *et al.*, 1990; MacDonald & Geyer, 2004), and we see in Figure 2.5 that C_i/α values as large as 10 significantly modify n. Therefore, mean bottom slopes as small as 10^{-5} are enough to reduce n below the canonical value of 2 to 2.5 derived from the theory of Schijf & Schönfeld (1953). This suggests that slope effects may explain the deviation of observed length-discharge relationships in salt wedge estuaries from the flat estuary solution.

Unlike in the flat, prismatic channel solution presented above, n is now a function of the parameter C_i/α. Prediction of this parameter is complicated by the variation of channel bottom slope about the mean value. The local variation in α is comparable to the uncertainty in C_i. However, model runs using the full bathymetric profile of the Merrimack River, discussed in Section 2.6.2, suggest that the model is insensitive to variations in bottom slope about the mean, when compared to the results obtained assuming a constant bottom slope. More significant is the dependence on C_i, which is both an uncertain parameter and a global parameter within the model, affecting the entire intrusion and modifying the dependence of L on Q. This makes it difficult to predict the exact value of n *a priori*, and therefore to use the observed length-discharge relationship to diagnose the dynamic regime. However, we show in Section 4.5 that this solution is a significant improvement over the results of Schijf & Schönfeld (1953).

2.5 Solution for Flat and Sloped Estuaries of Converging Width

We next consider the solution for intrusion length in an exponentially converging estuary– that is, an estuary of landward-decreasing width that can be described by

$$b(x) = b_\infty + (b_0 - b_\infty)\, e^{x/a} \tag{2.23}$$

where $b(x)$ is the width at a given location x in the channel, b_∞ is the uniform width in the channel upstream of the estuary, b_0 is the width of the channel at the mouth, and a is the convergence length. This configuration is shown schematically in Figure 2.2, bottom right. Salt wedges typically occur in coastal plain estuaries (Valle-Levinson, 2011), where an exponential equilibrium profile often exists (Savenije, 2005). In Section 2.6.2, we compare our model to data for the Duwamish and Merrimack River estuaries. The Duwamish is a highly urbanized and channelized estuary and so is not effectively described by a simple exponential model. However, the Merrimack, outside of an expansive tidal embayment, is described very effectively by an exponential profile of the above form ($R = 0.64$, fit not shown). In both cases, we will begin by examining a uniform width solution and then incorporate a simplified width model based on the observed geometry of the estuary.

We non-dimensionalize this width profile by dividing by the width at the mouth b_0:

$$b_*(x_*) = \frac{1}{R_c} + \left(1 - \frac{1}{R_c}\right) e^{x_*/a_*}, \tag{2.24}$$

where we have defined the convergence ratio $R_c = b_0/b_\infty$, which is the ratio of the width at the mouth to that in the upstream river, and the non-dimensionalized convergence length $a_* = C_i a/h_S$, which is non-dimensionalized in the same manner as x_* and L_*. These parameters indicate the magnitude (R_c) and rate ($1/a_*$) of exponential convergence.

2.5.1 Existence of Hydraulic Solutions in a Converging Estuary

A subcritical hydraulic solution for an arrested saline intrusion in a converging estuary does not necessarily exist. Rearranging Equation 2.13 produces a cubic equation relating h_{1*} to

$\Delta H'_*$:

$$h_{1*}^3 - \Delta H'_* h_{1*}^2 + \frac{1}{2}\frac{F_f^{4/3}}{b_*^2} = 0 \tag{2.25}$$

This relationship indicates that there is a minimum allowable value of $\Delta H'_*$, equal to $3/2b_*^{2/3}$, that is a function of the local width $b_*(x_*)$ and therefore position x_*. This is the non-dimensionalized local critical buoyant hydraulic head anomaly $\Delta H'_{*c}$. If the value of $\Delta H'_*$ falls below the local value of $\Delta H'_{*c}$, then no subcritical hydraulic solution in which the mouth acts as control exists. If the mouth acts as control, the value of $\Delta H'_*(x_* = 0) = \Delta H'_{*c}(x_* = 0)$. In a converging estuary, the local value of the critical buoyant hydraulic head anomaly increases upstream as the width decreases because $\Delta H'_{*c} \sim b_*^{-2/3}$. Thus, $\Delta H'_*$ must at least initially increase upstream at a faster rate than $\Delta H'_{*c}$ if a solution is to exist in which the mouth acts as control. If the solution considered were frictionless, $\Delta H'_*$ would be conserved and no solution could exist in a converging channel. However, if friction at the interface is considered, $\Delta H'_*$ increases upstream at the rate given by Equation 2.15:

$$-\frac{d\Delta H'_*}{dx_*} = \frac{F_f^{4/3}}{b_*^2 h_{1*}^3}\left(1 + \frac{h_{1*}}{h_{2*}}\right),$$

where the negative sign is included because we are interested in the rate of increase *upstream*, but the positive x_*-direction is taken to be downstream. Therefore, a solution for a subcritical salt wedge controlled at the mouth can exist only if interfacial friction is considered.

It is not possible to determine all necessary and sufficient conditions for existence of a hydraulic solution because the solution will fail anywhere that $\Delta H'_*$ falls below $\Delta H'_{*c}$, but $\Delta H'_*$ is a property of the solution that cannot be determined *a priori*. We may, however, formulate a necessary condition for existence based on the behavior of the solution at the mouth. The specific head anomaly is equal to the local critical specific head anomaly at the control (by definition). Thus, the upstream rate of increase of $\Delta H'_*$ at the mouth, given by

$$-\left(\frac{d\Delta H'_*}{dx_*}\right)_{x_*=0} = \frac{1}{F_f^{2/3}\left(1 - F_f^{2/3}\right)}, \tag{2.26}$$

must exceed the rate of increase $\Delta H'_{*c}$ at the same location, given by

$$-\left(\frac{d\Delta H'_{*c}}{dx_*}\right)_{x_*=0} = -\frac{d}{dx_*}\left(\frac{3}{2b_*^{2/3}}\right)_{x_*=0} = \left(\frac{db_*}{dx_*}\right)_{x_*=0}. \tag{2.27}$$

From Equation 2.24, we find that

$$\left(\frac{db_*}{dx_*}\right)_{x_*=0} = \frac{1}{a_*}\left(1-\frac{1}{R_c}\right), \tag{2.28}$$

Combining Equations 2.26, 2.27, and 2.28, and requiring that $\Delta H'_*$ increase at a rate faster than $\Delta H'_{*c}$, we find a necessary (though not sufficient) condition for existence of a hydraulic arrested salt wedge solution in an exponentially converging estuary:

$$\frac{a_*}{1-R_c^{-1}} > F_f^{2/3}\left(1-F_f^{2/3}\right). \tag{2.29}$$

The uniform width solution is obtained when the convergence ratio $R_c = 1$ or when the non-dimensionalized convergence length $a_* \to \infty$. In either case, the left hand side of Equation 2.29 goes to infinity, consistent with the fact that a hydraulic solution always exists in the uniform width case. The right hand side has a maximum of $1/4$ at $F_f = 1/(2\sqrt{2}) \approx 10^{-0.452}$. We anticipate that there will be regions where a hydraulic solution does not exist centered on $F_f = 10^{-0.452}$ for sufficiently small convergence lengths and/or sufficiently large convergence ratios. This will be examined in the following section.

2.5.2 Length-Discharge Relationship

We now explore the length-discharge relationship in flat and sloped converging estuaries. We recall that, having now introduced the convergence ratio R_c and non-dimensionalized convergence length a_*, and suppressing the dependence on $\Delta\rho/\rho_2$, L_* is a function of F_f, C_i/α, R_c, and a_*.

Flat Estuary

The solution for intrusion length in a flat, converging estuary is shown in Figures 2.6 and 2.7. In Figure 2.6, we compare the flat, prismatic estuary solution (labeled "L_* vs. F_f"),

four solution curves with $R_c = 5$ and values of a_* ranging from 0.1 to 100 as labeled, and a modified version of the flat, prismatic estuary solution (labeled "L'_* vs. F_f"). The value of L'_* is obtained based on a modified freshwater Froude number

$$F'_f = \frac{Q}{b_\infty \sqrt{g' h_S^3}} = \frac{b_0}{b_\infty} \frac{Q}{b_0 \sqrt{g' h_S^3}} = R_c F_f \tag{2.30}$$

using Equation 2.21, the solution for L_* in a flat estuary of uniform width developed by Schijf & Schönfeld (1953). The solution asymptotes to these two bounding solutions, corresponding to uniform estuaries of width equal to the width at the mouth and in the river, for high and low freshwater Froude numbers, respectively. The transition between the bounding solutions occurs when L_* is roughly between one and ten times a_*. This is discussed extensively in Section 2.6.1 below and shown schematically in Figure 2.10b. The gaps on each of the curves correspond to regions where a hydraulic solution does not exist. The region of nonexistence shrinks for increasing non-dimensionalized convergence length a_*, as Equation 2.29 would predict. However, Equation 2.29 predicts existence where it was found that hydraulic solutions do not exist. This is an indication that it indeed is not a sufficient criterion to guarantee existence, as discussed above.

Figure 2.7 shows the solution for a constant value of the non-dimensionalized convergence length $a_* = 1$ and different values of the convergence ratio R_c. We show the uniform width Schijf & Schönfeld (1953) solution, which corresponds to $R_c = 1$, and the solution curves for $R_c = 10$ and 100; these curves display the same asymptotic behavior as observed in Figure 2.6. We have also plotted the solution obtained in the limit that $R_c \to \infty$, which corresponds to a width at the mouth that is infinitely larger than that in the upstream river. We see that the finite R_c length-discharge relationships follow the $R_c \to \infty$ curve in the transition region. By investigating the behavior of infinite R_c solutions with different values of a_* (figure not shown), we found that n is nearly independent of a_* and $O(0.1)$ for $F_f < 10^{-3}$. This indicates that convergence by itself in a flat estuary could potentially account for the discrepancy between the Schijf & Schönfeld (1953) solution and observations. However, topography data from the Duwamish and Merrimack, examined in Section 2.6.2

below, as well as from the Fraser River estuary indicate values of R_c on the order of 5 to 10. In this case, though n is reduced in the transition region, it remains $O(1)$, and the reduction is not enough to account for the discrepancy.

Sloped Estuary

Figures 2.8 and 2.9 show the effects of varying R_c and a_*, respectively, on the intrusion length when the bottom slope α is nonzero and C_i/α is therefore finite. In Figure 2.8, the non-dimensionalized convergence length a_* is held constant at 1 while the convergence ratio R_c is varied between 1 and 10. We expect from above that the modification of the solution curve due to contracting width effects occurs when $L_* > a_*$. Thus, we anticipate that significant modification of the solution curve will occur only when the maximum possible value of L_*, C_i/α, is greater than a_*. Additionally, since the limiting value of L_* is independent of width, the effects of variable width should become less apparent as $L_* \to C_i/\alpha$, i.e., as $F_f \to 0$. This is precisely what is observed in Figure 2.8. Noticeable deviation of L_* from the constant width values occurs only for the curve for which $C_i/\alpha > a_*$ ($C_i/\alpha = 10$ and $a_* = 1$). The deviation associated with R_c also decreases with decreasing F_f, as anticipated, and increases with R_c, as would also be expected. The magnitude of the effect of converging width on the intrusion length is highly dependent on the geometry of the estuary, in particular on how the slope-limited value of the intrusion length compares to the width convergence length of the estuary. Synthesizing our observations, we conclude that exponential estuary convergence has a significant impact on intrusion length only when $(C_i/\alpha)/a_* = h_S/(\alpha a) > 1$.

In Figure 2.9, as in Figure 2.6, R_c is held constant at 5 while a_* is varied between 0.1 and 100. As we would expect, the larger the ratio of C_i/α to a_*, the greater the effect of the variable width. Additionally, the effect of the variable width becomes less apparent at lower values of F_f as the slope limiting mechanism becomes more important. Depending on how greatly C_i/α exceeds a_*, the predicted intrusion length may deviate by as much as an order of magnitude from the uniform width value. However, the intrusion length is bounded by that which would be obtained in an estuary of uniform width b_∞. This is the gray dashed

lower bounding curves for each set of curves corresponding to a different value of C_i/α in Figure 2.9. We observe that width convergence can indeed significantly affect the value of n when the estuary slope is non-zero. However, we note from Figure 2.8 that, even when the effects of width convergence are most pronounced, they are still secondary to those of slope limitation on the value of n. We therefore conclude that mean bottom slope likely has the more significant effect on n in real salt wedge estuaries.

2.6 Discussion

We have developed solutions for the dependence of intrusion length in a highly stratified salt wedge estuary on river discharge for estuaries with nonzero bottom slope and converging width. Our solutions indicate that 1) nonzero bottom slope strongly modifies the magnitude of dependence of L on Q (characterized by the value of n in the relationship $L \sim Q^{-n}$) for even modest bottom slopes, 2) there is a transition region where convergence tends to decrease n in both flat and sloped estuaries, 3) within the typical parameter space, the influence of nonzero bottom slope is greater than the influence of convergence on the length-discharge relationship in a salt wedge estuary, and 4) the reduction of n in the sloped estuary solutions is enough to account for the deviation of observations from the theory for flat, prismatic channels developed by Schijf & Schönfeld (1953). In Section 2.6.2, we will assess whether our solution is consistent with available data.

2.6.1 Slope-Limitation and Estuary Convergence

The slope-limitation mechanism is described in Section 2.4 and is shown schematically in Figure 2.10a. Unlike in the flat estuary case, there is a finite limit to the distance the salt wedge can penetrate upstream. As the discharge approaches zero, the thickness of the salt wedge at the mouth approaches the shoreline depth, and the intrusion length approaches h_S/α. This corresponds to a limiting value of the non-dimensionalized intrusion length $L_* = C_i/\alpha$. Physically, as the salt wedge intrudes into an estuary of nonzero mean bottom slope, the change in elevation of the pycnocline from mouth to toe is less than in a flat estuary. This

corresponds to a smaller mean interfacial slope and therefore a weaker mean baroclinic pressure gradient forcing the upstream propagation than in the flat estuary case. Additionally, the reduced water depth results in reduced layer thicknesses and correspondingly enhanced friction. These mechanisms allow the slope-limitation mechanism to be felt over the entire parameter space and have such a strong impact on the value of n, decreasing it by an order of magnitude relative to the flat bottom case.

In our simplified model of a variable width estuary, in which we assumed the width decreased exponentially from its value at the mouth to a uniform value in the upstream river, we found that the solution for intrusion length as a function of discharge asymptotes between solutions based on the width at the mouth and the width in the upstream river. As illustrated in Figure 2.10b, the transition zone between these two solutions was observed to lie between one and ten convergence lengths landward of the mouth. For intrusion lengths less than the convergence length, the intrusion does not feel the change in width, behaving as if the channel width were constant and equal to the width at the mouth, b_0. When the intrusion length is greater than ten convergence lengths, the intrusion feels only the width of the upstream river, b_∞. In between, it transitions between the two asymptotic solutions, as observed in Figures 2.6 and 2.9. Within the transition zone, the value of n is decreased in both flat and sloped estuaries.

We can combine these two observations to determine a criterion for when width convergence has an effect on intrusion length. The salt wedge can only penetrate a distance h_S/α into the estuary. Convergence effects only become relevant when $L > a$. Therefore, convergence alters intrusion length only if $h_S/(\alpha a) > 1$. This is apparent in Figures 2.8 and 2.9, in which we see there is no deviation of the converging estuary solution from the uniform width solution when $a_* = C_i a/h_S < C_i/\alpha$.

2.6.2 Comparison of L vs. Q to Real Estuaries

In this section we compare the sloped estuary solution for intrusion length to numerical data from an extensively validated realistic numerical model of the Merrimack River estuary

(Ralston *et al.*, 2010) and field data from the Duwamish River estuary (McKeon *et al.*, 2014). In both cases, we begin with a sloped uniform width model and then examine the influence of a simplified version of the observed width profile on the solution. Both estuaries are observed to be salt wedges (Ralston *et al.*, 2010; McKeon *et al.*, 2014). Data for intrusion length, tidal amplitude, and river discharge from a Finite Volume Ocean Costal Model (FVCOM) of the Merrimack was provided by Dr. D.K. Ralston. A detailed description of the model can be found in Ralston *et al.* (2010). The intrusion length provided is the landward-most location of the intersection of the 2 psu isohaline with the channel bottom. Maximum intrusion occurs soon after high water. Ideally, we would compare to intrusion length determined as the landward-most extent of the point of maximum bottom salinity gradient, since our model predicts the structure of the pycnocline. Using the 2 psu isohaline instead introduces some error when comparing the numerical data to our model owing to the finite thickness of the density front in real estuaries. However, we assume that the extent of the salinity front is small compared to the intrusion length so that the associated error is small. We compare data for the smallest modeled tidal amplitude (2 m) to the hydraulic solution presented here to assess whether the hydraulic solution accurately characterizes the dependence of intrusion length on discharge. The lowest tidal amplitude was selected so that tidal effects, which are not considered here, are minimized.

Assuming the mouth acts as control, it is necessary to determine the width and depth at the mouth to calculate the freshwater Froude number. Based on bathymetric data provided for the Merrimack, the width of the estuary at the mouth is $b_0 = 320\,m$, the mean bottom slope is $2.3(10^{-4})$, and the shoreline depth is $h_S = 7.75\,m$.

From these values of h_S and b_0, along with the discharges corresponding to the modeled salinity intrusions, we can determine the values of the freshwater Froude number $F_f = Q/b_0\sqrt{g'h_S^3}$, provided that we know the value of $\Delta\rho/\rho_2$. Given the uncertainty in the estuary-averaged top-to-bottom salinity difference at arrest, we allow the stratification to vary when finding a best-fit of the hydraulic solution to the data and then confirm that this value is reasonable.

The values of $L_* = C_i L/h_S$ and C_i/α also depend on the value of C_i, which is found to be in the range 1 to $5(10^{-4})$ (Sorgard *et al.*, 1990; MacDonald & Geyer, 2004). The model is fit to the data by systematically varying C_i and $\Delta\rho/\rho_2$ and determining the values of C_i and $\Delta\rho/\rho_2$ for which the sum of the normalized squared residuals is minimized. In finding the best fit, C_i is allowed to vary over the range 10^{-6} to 10^{-2} in order to robustly test if the model will settle on a value falling within the typically observed range, and $\Delta\rho/\rho_2$ over the range 0.01 to 0.023. The stratification value represents an average over different discharges and longitudinally through the salt wedge at the moment of arrest; therefore, it is not clear *a priori* what value is appropriate. The goodness of fit (assessed by visual inspection and normalized absolute error) and the values of $\Delta\rho/\rho_2$ and C_i provide an indication of whether or not the variable slope hydraulic solution for intrusion length accurately describes the data. The values of C_i and $\Delta\rho/\rho_2$ obtained are $4(10^{-4})$ and 0.013, respectively. That C_i was allowed to vary over four orders of magnitude and converged to a value within the typically observed range suggests that the hydraulic model accurately describes the behavior of the system. The value of $\Delta\rho/\rho_2 = 0.013$ corresponds to a top-to-bottom salinity difference of 17 psu, roughly midrange between oceanic (30 psu) and freshwater salinity. In reality, the value of $\Delta\rho/\rho_2$ will vary with location in the salt wedge and river discharge, but these complexities are neglected here. This fit produces a mean normalized absolute error of 48%; however, much of this error is due to the underprediction of intrusion length near the mouth in the vicinity of the tidal embayment (discussed further below). Excluding these points, the normalized error is 30%. The graphical comparison of the numerical model data to the prediction of the hydraulic model, along with the corresponding solution for a flat, prismatic estuary (Schijf & Schönfeld, 1953), is shown in Figure 2.11b. The hydraulic model incorporating bottom slope is a significant improvement over the Schijf-Schönfeld solution; the model predicts the correct order of magnitude for the salinity intrusions when the freshwater Froude number is below ~ 0.3 (the majority of the data), as well as for the magnitude of dependence of salinity intrusion on discharge, characterized by n, the slope of the $L_* - F_f$ curve in logarithmic space. In contrast, the Schijf-Schönfeld solution predicts salinity intrusions that are as much

as three orders of magnitude greater than the numerical model data and a value of n that is an order of magnitude larger than observed.

In Figure 2.11b, we see that the (uniform width, uniform slope) hydraulic solution underpredicts intrusion length for $F_f >\sim 0.2$ and overpredicts intrusion length for $F_f <\sim 0.1$. Possible reasons for the failure of this simple hydraulic model include the effects of variable width, local variations in the channel bottom elevation about the mean bottom slope, the variation of mean top-to-bottom stratification with discharge, tides, and the inapplicability of the assumptions of the hydraulic theory (e.g., the flow is not quasi-steady and/or one-dimensional, there is not a predominantly two-layer flow structure, the pycnocline occupies a significant portion of the water column). Also shown in Figure 2.11b (dot-dashed line) is the hydraulic model solution incorporating a variable width profile. From the constriction landward, the variation in width allows the saline intrusion to penetrate further upestuary than it would have otherwise. This suggests that some of the increased intrusion at higher discharges may be explained by the effects of variable width. However, within and seaward of the embayment, the predicted intrusion length is now smaller than predicted by the uniform width model. Thus, it is unlikely that variable width explains the divergence for high discharges. The normalized absolute error is 50%, nearly unchanged from the uniform width model.

The tendency for the hydraulic model to overpredict intrusion length for lower discharges and underpredict intrusion length for higher discharges would be consistent with stratification ($\Delta\rho/\rho_2$) that increased with discharge. However, the solution curves corresponding to a top-to-bottom salinity difference of 5 and 30 were calculated (not shown), and it was found that the corresponding differences in predicted intrusion length are relatively small compared to the difference between the numerical data and prediction of the hydraulic model. The hydraulic model was also run with the true channel bottom elevation profile (not shown), but the results were not significantly different from the solution obtained using a constant slope and did not explain the deviation of the hydraulic prediction from the numerical model data.

Underprediction of intrusion length at high discharges and overprediction at low discharges is also consistent with the effects of tidal forcing. We would anticipate that, at high discharges, when the intrusion length that would be obtained under the river discharge alone is small, tidal advection during the flood will force the intrusion far past this equilibrium point, whereas, at low discharges, when the intrusion length under the action of the river discharge alone is large, the salt wedge will not have time to reach the equilibrium point with the river within half of the tidal period. This is consistent with the behavior observed in Figure 2.11b. The good performance of this hydraulic solution in predicting the intrusion length suggests that the behavior of L with Q is in fact consistent with the previously observed hydraulic behavior of these estuaries.

The predicted intrusion length was also compared to field data taken in the Duwamish (McKeon *et al.*, 2014). McKeon *et al.* (2014) define intrusion length as the landward-most point with a top-to-bottom salinity difference greater than 5. This presumably gives a better indication of the location of the toe than the 2 psu isohaline. The intrusion lengths have been interpolated to one-quarter of the way through flood tide (hereafter referred to as "quarter-flood") because this was the most reliably sampled phase of the tide. The model introduced here predicts the maximum intrusion length at the time of arrest before lower layer reversal. However, the comparison of the model to this data will still give an idea of whether or not it is able to predict the magnitude of dependence of intrusion length on discharge accurately.

Figure 2.11d shows the field data, this time in terms of L and Q–not L_* and F_f. Dimensional variables are plotted because we consider a hydraulic model with variable control points. We find that a uniform width solution assuming control at the mouth, similar to the solution applied to the Merrimack, overpredicts intrusion length by as much as 4 km, larger than the 3.6 km tidal excursion of the salt wedge toe reported by Dawson & Tilley (1972), and does not accurately reproduce the observed dependence on discharge. We hypothesize that this is because the flow is not controlled at the mouth under low discharge conditions and that the relevant control point may vary between the mouth and significant flow constrictions associated with the 1st and 16th Avenue Bridge piers, located at river kilometers

5.2 and 7.3, respectively (Figure 2.11c).

To test this, we modified the model to include a linearly converging width profile superimposed with the two pier constrictions (Figure 2.11c) and allowed the control location to vary. The control is assumed to be the landward most potential control point that is accessible by the intrusion. Thus, an iterative method of determining the location of control, wherein the seaward most control is assumed and the solution is integrated landward until either the toe or the next potential control point is reached, is implemented. We could also have obtained a solution by assuming that a control was not activated when it became accessible–that is, by assuming that intrusions extending past the more landward 16th Avenue Bridge pier were still controlled at the 1st Avenue Bridge pier. This creates some ambiguity in the solution; however, evidence is presented in McKeon *et al.* (2014) suggesting that the 16th Avenue Bridge pier does indeed control the flow when the lower layer extends that far landward. The variable control point model consistently overpredicts the intrusion length, as we would expect because the data is taken at quarter-flood, and accurately reproduces the value of $n \approx 0.2$, again an order of magnitude smaller than the canonical value from Schijf & Schönfeld (1953) (McKeon *et al.*, 2014). Note that for both of the hydraulic models of the Duwamish we chose typical values of the interfacial drag coefficient and density anomaly–$C_i = 10^{-4}$ (Sorgard *et al.*, 1990; MacDonald & Geyer, 2004) and $\Delta\rho/\rho_2 = 0.02$, roughly corresponding to the ocean-basin salinity difference of 28 psu (McKeon *et al.*, 2014)–rather than fitting the data. Because the data come from quarter-flood, a fit to the data produces unreasonably high values of C_i ($O(10^{-3})$) to account for the fact that the intrusions have not reached the arrest point.

When mean bottom slope is included, the predictions of the hydraulic model are consistent with field observations in the Duwamish and a well-validated numerical model of the Merrimack, which are both observed to behave as salt wedge estuaries (Ralston *et al.*, 2010; McKeon *et al.*, 2014). This potentially eliminates the need to appeal to more complex momentum balances and scalings for the intrusion length based on the dominance of tidal or exchange flux in estuaries that otherwise behave hydraulically, as is suggested by some

authors (e.g. Ralston *et al.*, 2010; Lerczak *et al.*, 2009). This is a significant result insofar as the behavior of L with Q is to be used as a diagnostic criterion for the dynamics of an estuary. Additionally, the potential resolution of the uncomfortable disparity between the clearly hydraulic behavior of salt wedge estuaries and the predictions of hydraulic theory is a significant result in itself.

2.7 Conclusion

We have found that even modest bottom slopes ($O(10^{-5})$) significantly reduces the magnitude of dependence of intrusion length on discharge for freshwater Froude numbers $F_f \sim O(0.1)$ or smaller, owing to the finite value of the maximum intrusion length in a sloped estuary. The solution for a sloped estuary of uniform width presented here predicts exponents n in a relationship of the form $L \sim Q^{-n}$ in the observed range (0.2 to 0.6) for freshwater Froude numbers roughly in the range 0.01 to 0.1 (Figure 2.5, Figure 2.11b). This solution shows that the value of n is highly dependent on C_i, an uncertain parameter, making it difficult to predict its value *a priori*. However, the solution presented here is a significant improvement over the solution of Schijf & Schönfeld (1953), giving an order of magnitude improvement in the prediction of n.

In an estuary of convergence length a, we find that the effect of convergence on the length-discharge relationship becomes significant only for intrusion lengths $L > a$. Convergence decreases the intrusion length from the value that would be obtained for the same discharge in an estuary of uniform width equal to the width at the mouth (Figures 2.6, 2.8, and 2.9). The intrusion length is bounded by the solutions for uniform width estuaries of width equal to that at the mouth of the estuary and in the upstream river (Figures 2.6 and 2.9). Within the transition zone ($a < L < 10a$), convergence tends to decrease the magnitude of n in both flat and sloped estuaries (Figures 2.6 and 2.9). Convergence can strongly modify the particular value of n in an estuary, but nonzero slope is the more significant influence for reasonable bottom slopes $C_i/\alpha \leq 10$ and convergence ratios $R_c \leq 10$.

The results from our comparison with field data from the Duwamish and numerical data

from the Merrimack indicate that the solution presented here is consistent with observed values of n in salt wedge estuaries. The actual intrusion length is not captured as accurately by the simple hydraulic solution owing to complications due to topography, tides, and other influences. However, these results suggest that the discrepancy between observed values of n and the canonical values of 2 to 2.5 is consistent with the influence of geometry on the hydraulic solution, primarily the effect of nonzero mean bottom slope, potentially eliminating the need to appeal to other dynamic influences or regimes to resolve this discrepancy.

Table 2.1: Dimensioned variables and their dimensionless equivalents. The subscript j indicates that the corresponding quantity for both layers 1 and 2 are non-dimensionalized in the same manner.

Dimensioned variables	Non-dimensioned variables and definitions
x	$x_* = C_i x/h_S$
b	$b_* = b/b_0$
h_b	$h_{b*} = h_b/h_S = -(\alpha/C_i)x_*$
Q	$F_f = Q/b\sqrt{g' h_S^3}$
η	$\eta_* = \eta/h_S$
h_j	$h_{j*} = h_j/h_S$
H_j'	$H_{j*}' = H_j'/h_{1c0}$

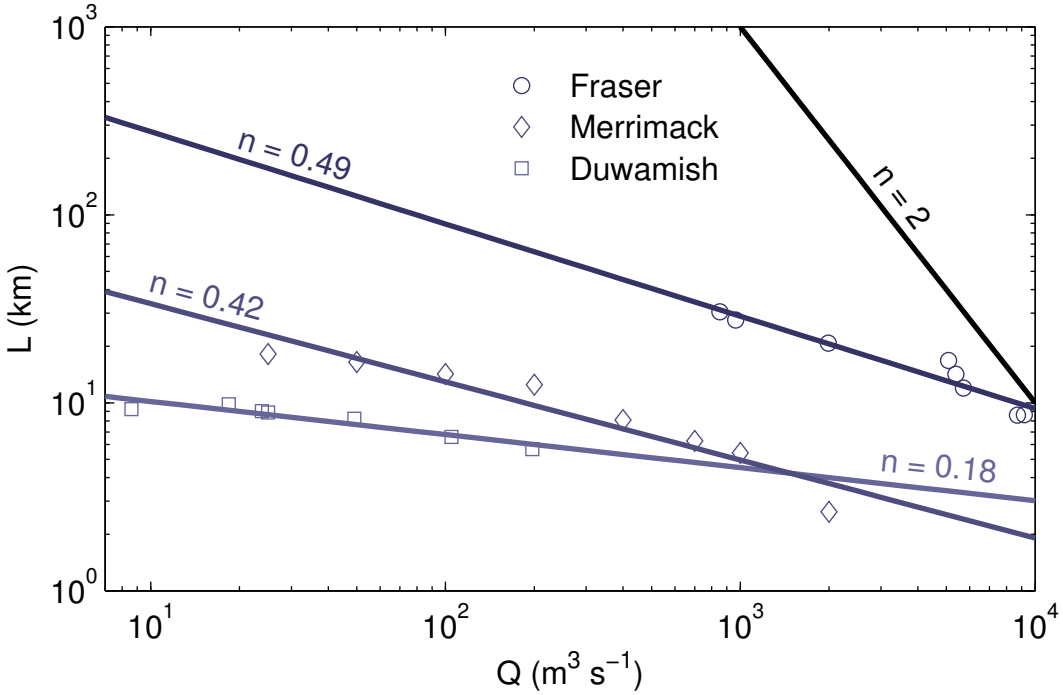

Figure 2.1: Comparison of length-discharge solution for flat, prismatic estuary (Schijf & Schönfeld, 1953), the $n = 2$ line, to field (Fraser, from Ward (1976), and Duwamish, from McKeon *et al.* (2014)) and numerical model (Merrimack, from Ralston *et al.* (2010)) data. Best-fit exponents for each estuary are shown.

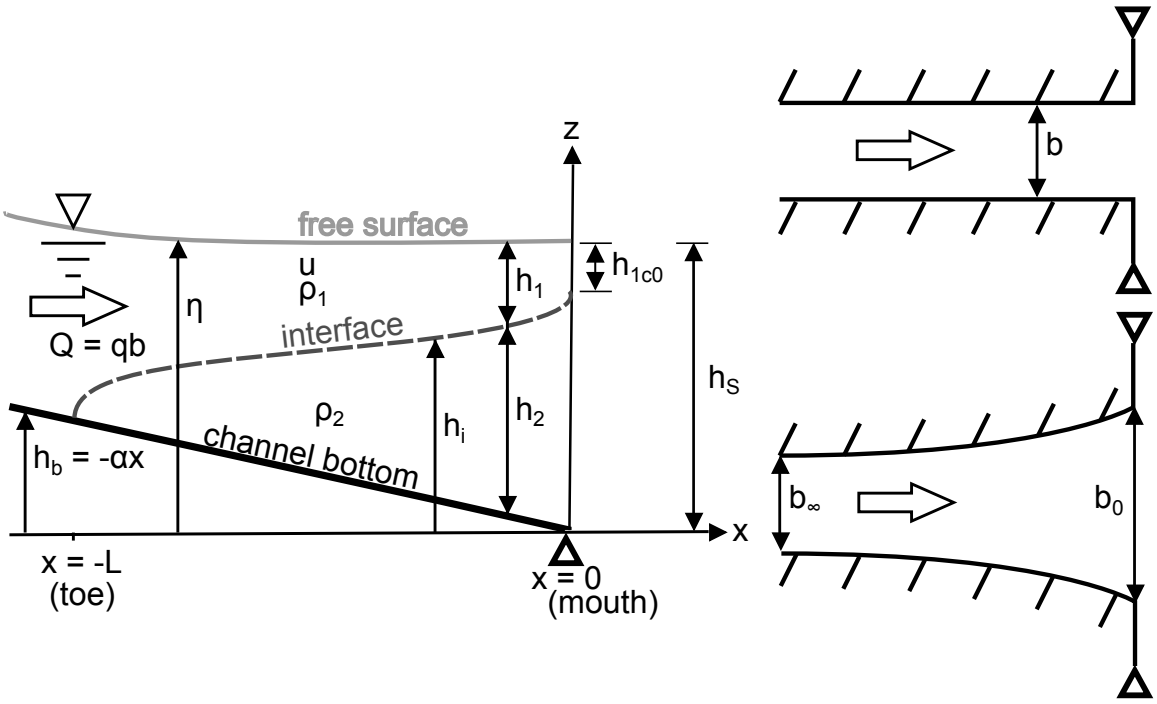

Figure 2.2: (Left) side view sketch and (right) plan view sketches of model configuration. Independent and dependent model variables are shown. The plan view shows the two width configurations considered here–uniform, top right, and converging, bottom right. The thick-lined triangles indicate hydraulic control.

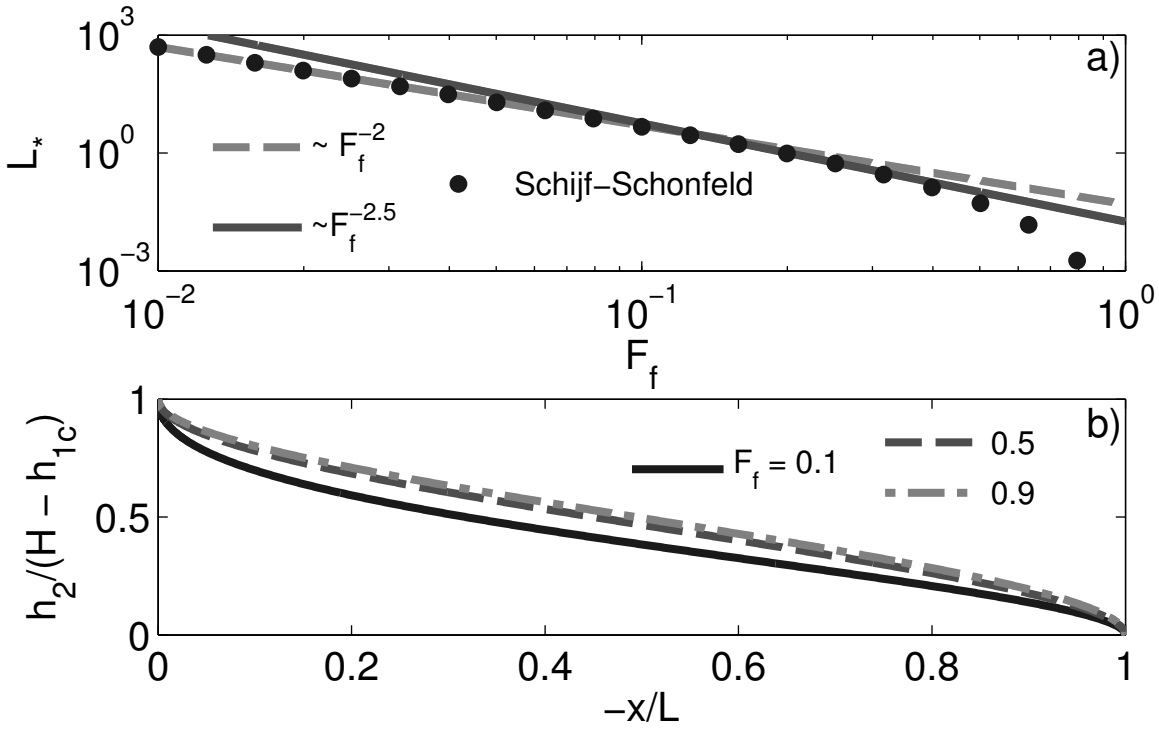

Figure 2.3: a) Non-dimensionalized intrusion length L_* versus freshwater Froude number F_f for a flat estuary of uniform width (Schijf & Schönfeld, 1953). The $L_* \sim F_f^{-2}$ and $\sim F_f^{-2.5}$ lines are also plotted. b) Normalized salt wedge shape (Harleman, 1961) for several values of F_f.

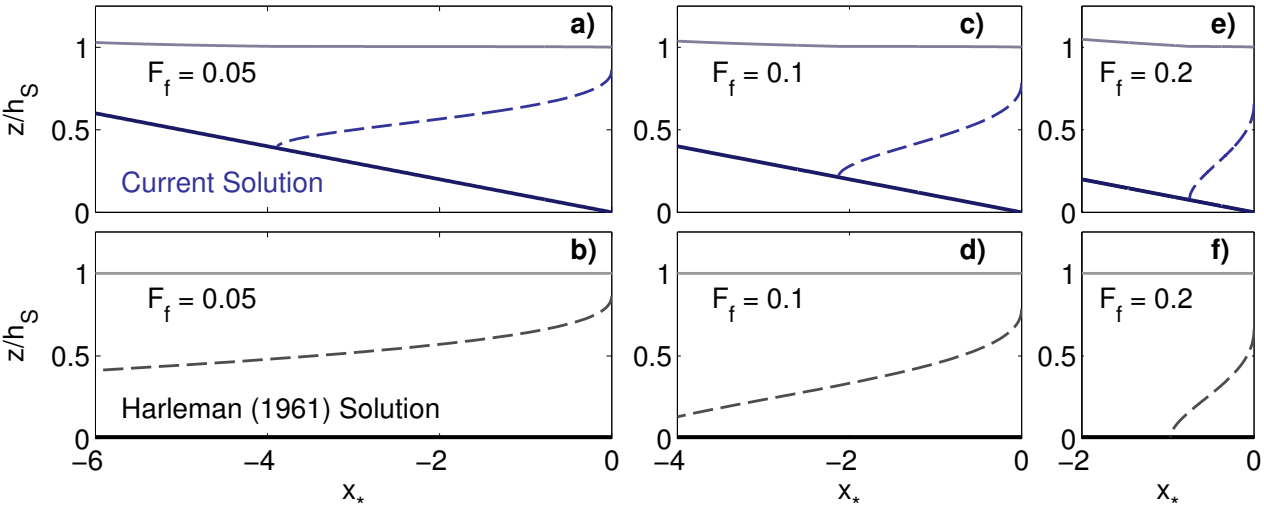

Figure 2.4: Comparison of interface profile with Harleman (1961) flat bottom solution. Panels a), c), and e) show three example model runs with increasing freshwater Froude number in a sloped estuary of uniform width. The dashed purple, solid purple, and gray lines correspond to the density interface, channel bottom, and free surface, respectively. Panels b), d), and f) show the Harleman (1961) solution for a flat estuary with a rigid lid for the same freshwater Froude numbers. The horizontal dimension of each column is scaled with the distance shown on the x-axis.

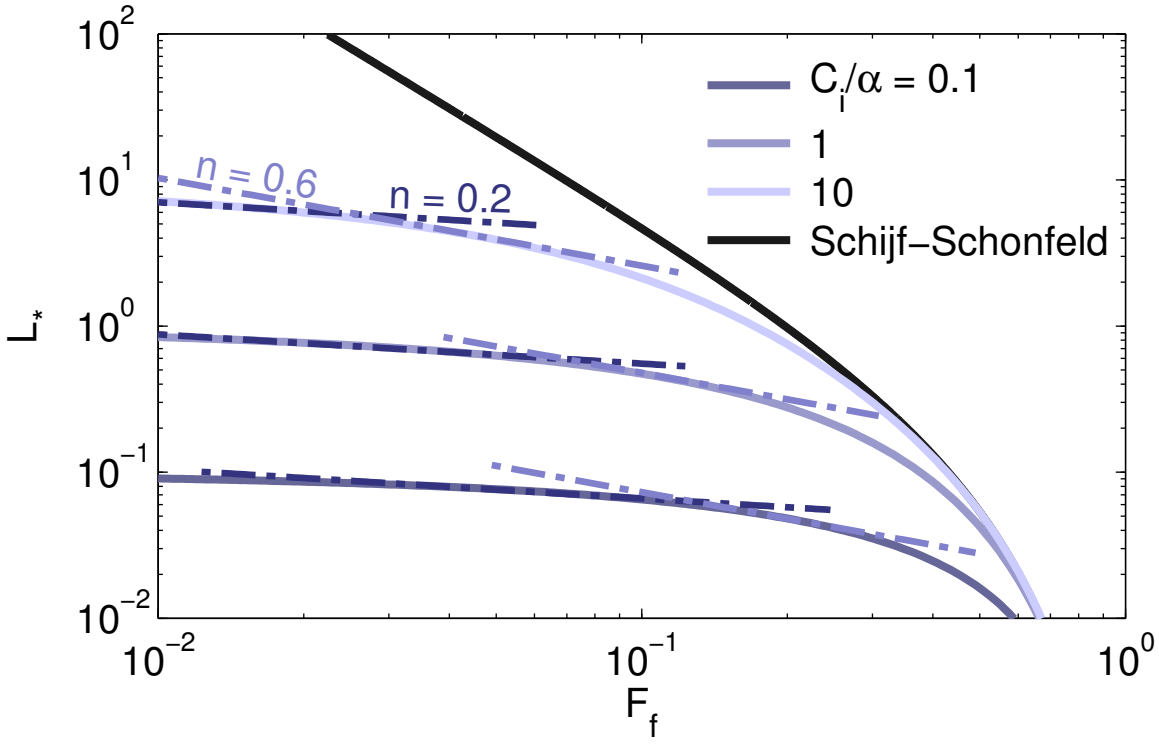

Figure 2.5: Intrusion length in a channel of uniform width and nonzero mean bottom slope α. The curves are segregated by the value of the parameter C_i/α. The flat estuary solution (Schijf & Schönfeld, 1953) is also shown. This corresponds to the limit $C_i/\alpha \to \infty$. Also shown are the $n = 0.2$ and 0.6 tangent lines.

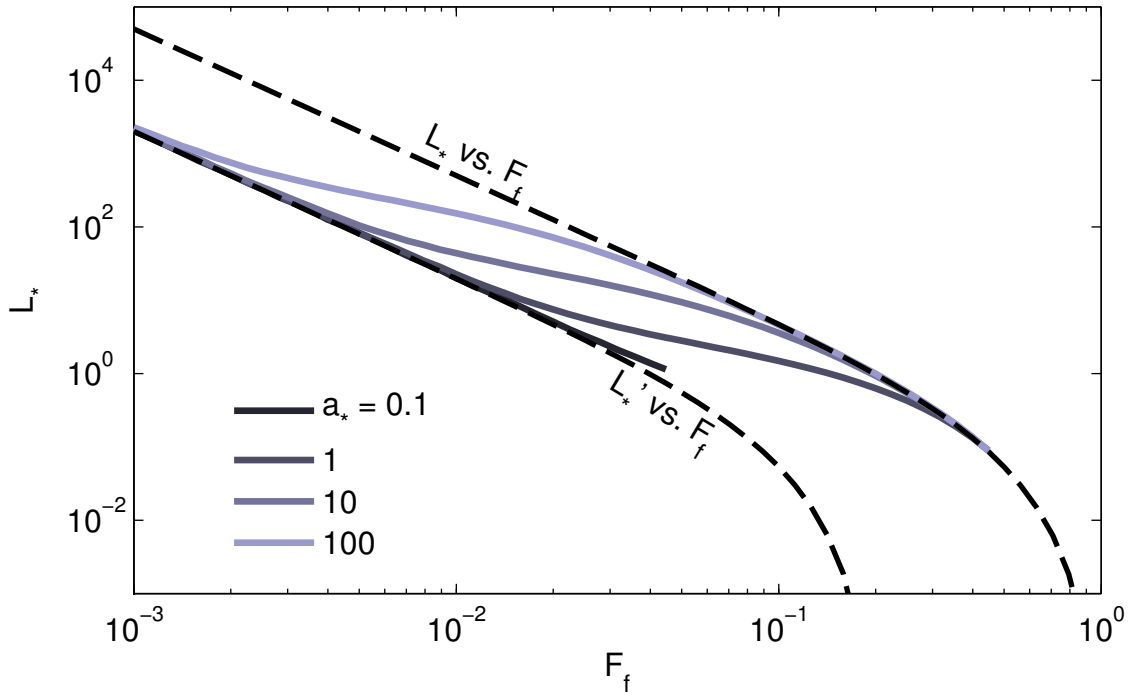

Figure 2.6: Intrusion length in a flat channel ($\alpha = 0$) with varying convergence length a_* and constant convergence magnitude $R_c = 5$. The black dashed lines show the asymptotic solutions discussed in the text. All solid curves are colored based on the value of the non-dimensionalized convergence length a_*.

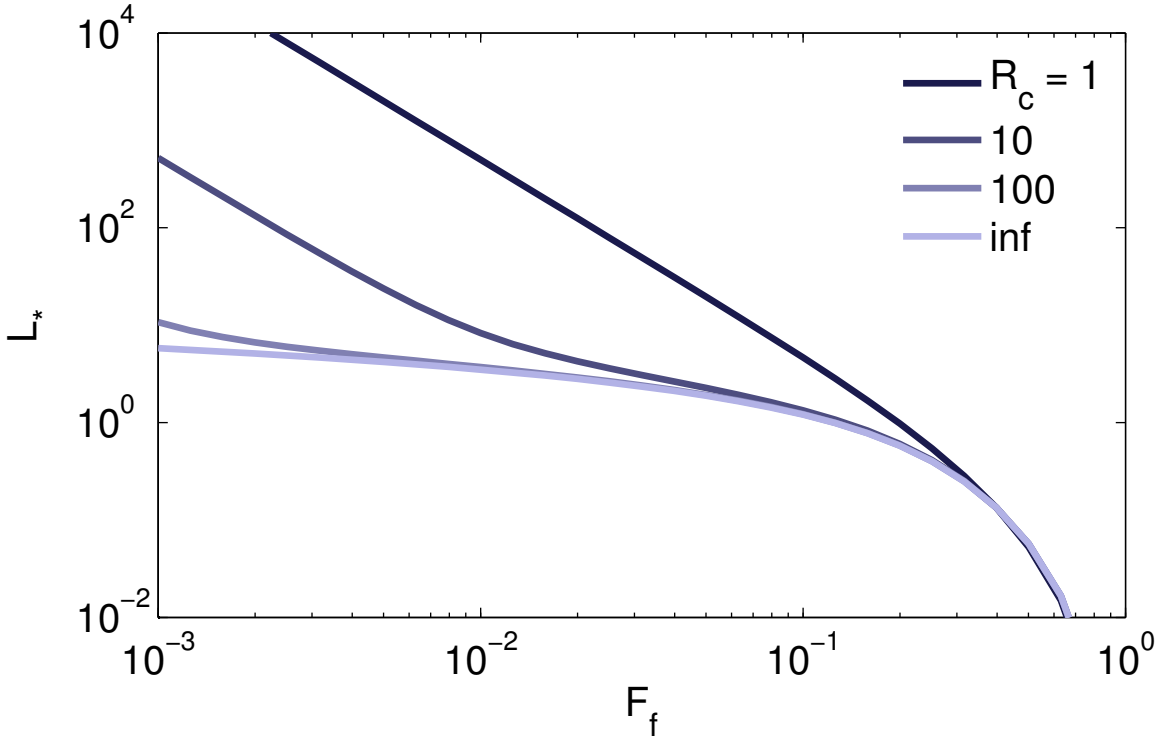

Figure 2.7: Intrusion length in a flat channel ($\alpha = 0$) with constant convergence length $a_* = 1$ and variable convergence magnitude R_c. All solid curves are colored based on the value of the convergence ratio R_c. The $R_c = 1$ line correspons to the Schijf & Schönfeld (1953) solution.

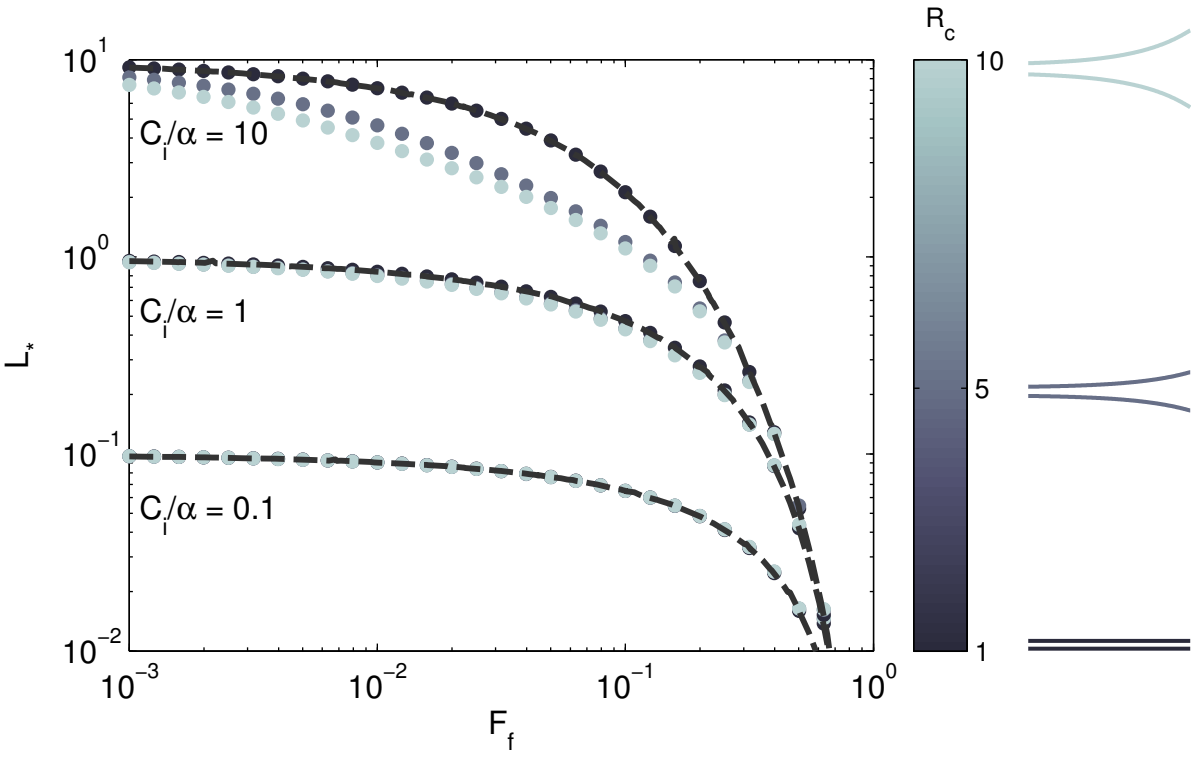

Figure 2.8: Intrusion length in a sloped channel ($\alpha \neq 0$) with constant convergence length $a_* = 1$ and variable convergence magnitude R_c. The dashed black lines indicate the prismatic channel solution (from Figure 2.5). All converging solution curves (dots) are colored based on the value of the convergence ratio R_c. Illustrations to the right of the Figure indicate how the estuary shape changes as R_c is modified and a_* is held constant.

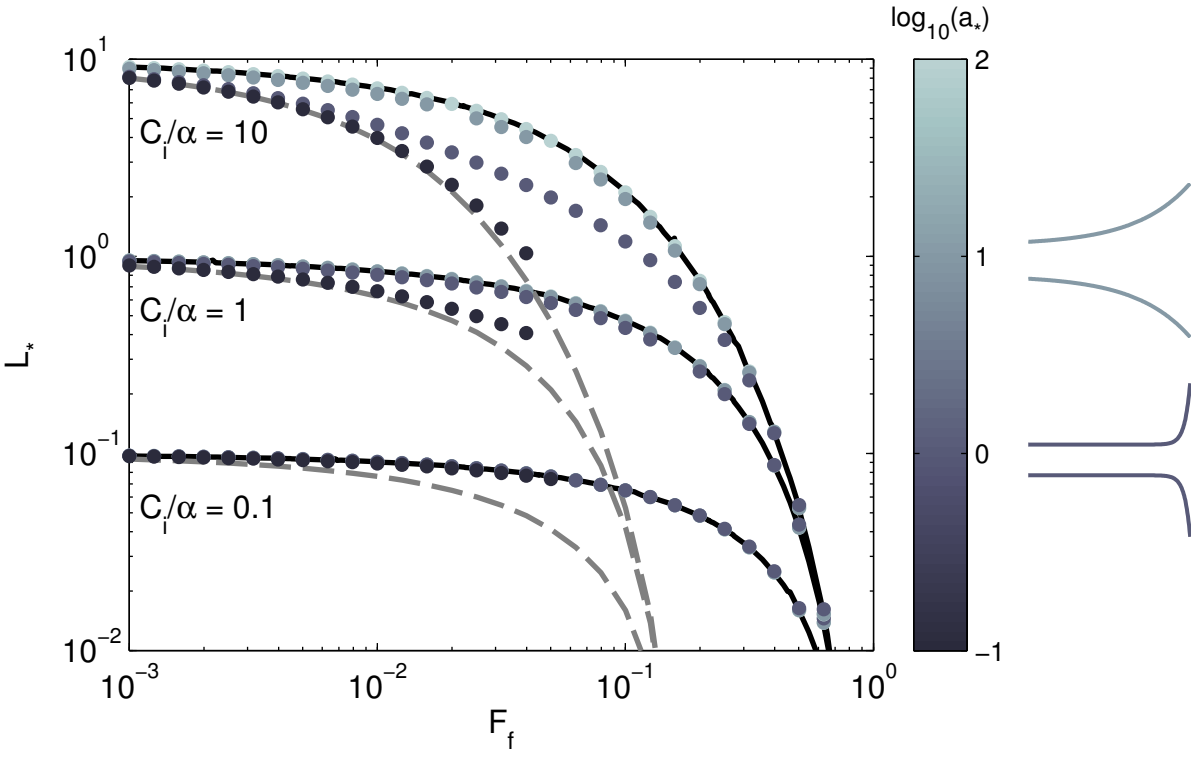

Figure 2.9: Intrusion length in a sloped channel ($\alpha \neq 0$) with varying convergence length a_* and constant convergence magnitude $R_c = 5$. The solid black and dashed gray lines indicate the asymptotic prismatic channel solutions. The black lines correspond to uniform width solutions with $b = b_0$, the width at the mouth; the dashed gray lines correspond to uniform width solutions with $b = b_\infty$, the width in the upstream river. All converging solution curves (dots) are colored based on the value of a_*. Illustrations to the right of the Figure indicate how the estuary shape changes as a_* is modified and R_c is held constant.

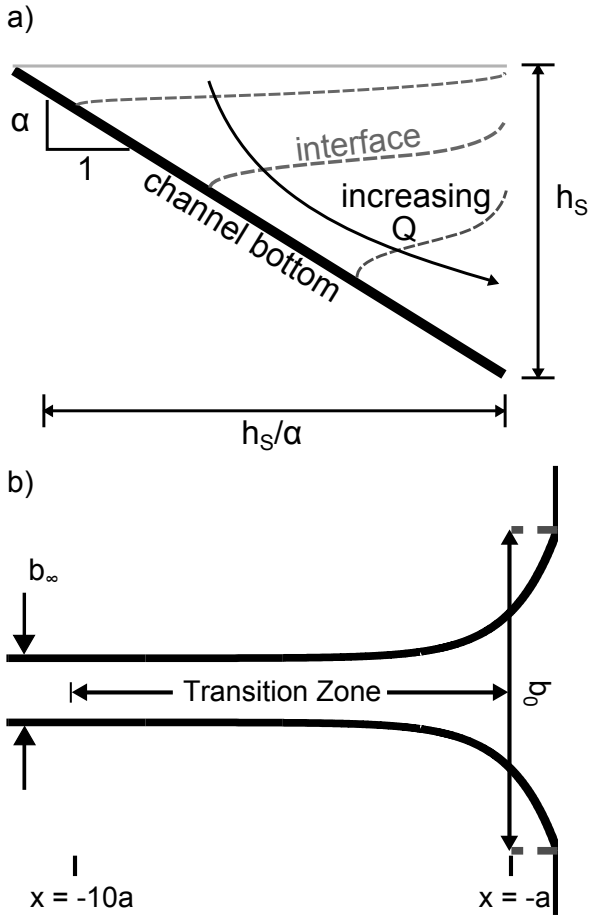

Figure 2.10: a) Schematic showing slope-limited salt wedge. b) Schematic showing location of the transition zone. For $L < a$, the intrusion is set by the width at the mouth b_0. For $L > 10a$, the intrusion is set by the width in the upstream river b_∞. In between, the intrusion length transitions between these two asymptotic solutions.

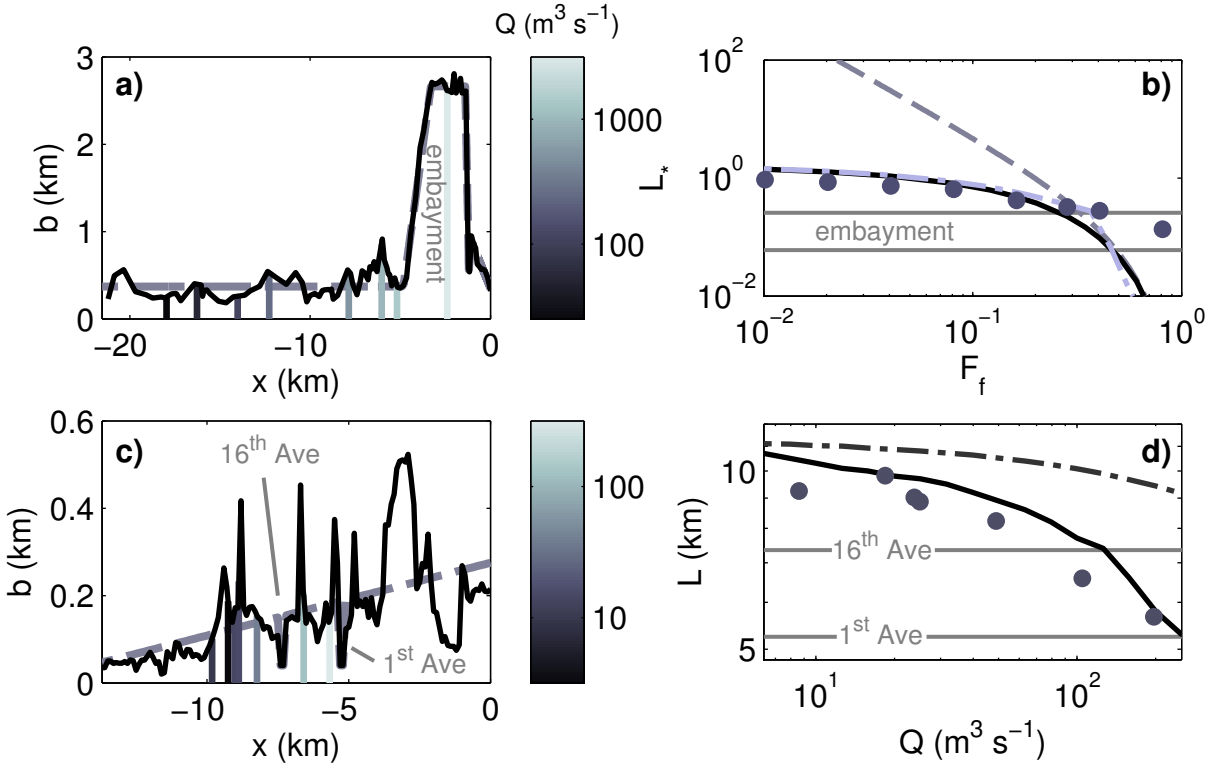

Figure 2.11: Top-width profiles of the a) Merrimack and c) Duwamish (solid black), salt wedge toe locations as function of discharge (solid, colored), and simplified width profile used in analysis (gray, dashed). b) Comparison of Merrimack numerical model data (Ralston *et al.*, 2010, gray-blue dots) to flat, prismatic estuary solution (Schijf & Schönfeld, 1953, dashed gray) and current solution without (solid black) and with (light blue dot-dash) variable width. d) Comparison of Duwamish field data (gray-blue dots) to the current solution assuming either control at the mouth and constant width (dot-dash gray) or variable width and control location (solid black).

Chapter 3

HYDRAULIC MODEL OF SEDIMENT TRANSPORT IN THE SALT WEDGE

3.1 Introduction

The lower river is a transitional zone from fluvial to marine hydrodynamic and sediment transport processes and is a key component of the source-to-sink pathway of fluvial sediment. The sediment flux imbalance across this region controls the availability of material for bed and land surface evolution, influencing its susceptibility to inundation from river flooding, subsidence, and sea level rise (Syvitski & Saito, 2007; Syvitski *et al.*, 2009), and controlling processes of channel avulsion and delta progradation (Jerolmack, 2009; Chatanantavet *et al.*, 2012; Lamb *et al.*, 2012). Furthermore, the net export of sediment from the river mouth provides active sediment to the shelf and is thus a control on continental sedimentation (e.g., Blum & Törnqvist, 2000). Understanding the processes by which sediment is deposited, eroded, or transited through the lower river is crucial for understanding river and shelf geomorphology and the ultimate fate of fluvial sediment. This goal is complicated by the complex interplay of tidal, riverine, density, wind, and wave forcing (e.g., Wright, 1977; Geyer *et al.*, 2004; Geyer & Ralston, 2011; Geyer & MacCready, 2014).

Several previous studies have applied hydraulic models of the river hydrodynamics and sediment transport to quantify bed evolution and depositional and erosional patterns in the lower river (Snow & Slingerland, 1987; Hotchkiss & Parker, 1991; Chatanantavet *et al.*, 2012; Lamb *et al.*, 2012). This work was motivated in part by the observation that rivers behave fundamentally differently in the vicinity of their mouths than they do further upstream. The river depth tends to the uniform normal depth h_N in the upstream direction; the normal flow region is characterized by spatially uniform velocity and net sediment bypass. Near

the mouth, however, the river is influenced by the static water level in the receiving basin (e.g., sea level), resulting in a hydraulic transition zone (see Figure 3.1). For discharges less than the 1.5 to 2 year flood, the depth imposed at the shoreline by the static water level in the basin, here referred to as the shoreline depth h_S, exceeds the normal depth, h_N (Lamb *et al.*, 2012). The free surface therefore must diverge from the channel bed, resulting in flow deceleration and net sediment deposition (Sturm, 2010; Lamb *et al.*, 2012). The extent of the backwater zone is expansive; at low flows it scales with the ratio of the shoreline depth to the channel bed slope, h_S/S_0, which can be on the order of 100 to 1000 km (Lamb *et al.*, 2012). The results of Chatanantavet *et al.* (2012) suggest that channel avulsion may be the consequence of sediment deposition as the flow enters the backwater region; these authors show that the avulsion length scales with the backwater length in many natural systems.

Absent in early hydraulic models of river morphodynamics was the dynamic variation of the extent and character of the hydraulic transition zone with changing river discharge. Previous studies assumed a single characteristic discharge, resulting in eventual filling of the backwater zone and the extension of the normal flow region of sediment bypass (Snow & Slingerland, 1987; Hotchkiss & Parker, 1991). Chatanantavet *et al.* (2012) and Lamb *et al.* (2012) improved upon this previous work by incorporating variable discharge and therefore the dynamic character of the hydraulic transition zone. In addition to decrease in length of the hydraulic transition zone with increasing discharge, these models allowed for transition from backwater to drawdown at discharges large enough that $h_N > h_S$ (see Figure 3.1). Drawdown is confined to a more compact region than backwater and is characterized by flow acceleration, convergence of the free surface and channel bed, and net erosion (see Figure 3.1) (Sturm, 2010; Lamb *et al.*, 2012). It has been suggested that the transition to drawdown at high flows explains the persistence of erosional zones near mouths and bifurcations in some rivers (Lane, 1957; Lamb *et al.*, 2012).

In most rivers, salt water penetrates some distance upstream from the sea forming an estuary. In highly stratified (salt wedge) estuaries especially, this results in a dramatic modification of the hydrodynamics and sediment dynamics and introduces another length

scale, the estuary length L_e, in addition to hydraulic transition length L_t that may be relevant to the morphology of the lower river. In salt wedge estuaries, the estuary intrusion length is less than the hydraulic transition length, except in the limit of zero discharge, when both scale as h_S/S_0 (Lamb *et al.*, 2012; Poggioli & Horner-Devine, 2015); thus, the estuary is contained within, and possibly modifies the extent and character of, the hydraulic transition zone. Whether the formation of an estuary significantly modifies the magnitude or distribution of deposition and erosion in the estuary, and the magnitude of sediment export to the shelf, remains an open question. We refer to the upstream river as the portion of the unstratified river directly upstream of the estuary that is not at normal depth. The lower river consists of the upstream river and the estuary. Our goals in this study are 1) to present a coupled hydraulic model of the hydrodynamics and sediment transport in a salt wedge estuary and the upstream river, and 2) to quantify the influence of estuary formation on the spatial distribution of sediment deposition in the channel and on export of sediment to the shelf. We apply a flux balance to the model to determine if and when the salt wedge modifies a) export to the shelf, and b) net deposition in the lower river. We also examine the location and magnitude of peak sediment deposition and therefore peak bed aggradation within and upstream of the estuary to c) characterize the spatial distribution of the deposition profile. We examine the location of peak bed aggradation because the results of Chatanantavet *et al.* (2012) suggest that this may set the avulsion length. We focus on highly stratified estuaries because high freshwater discharge is associated both with large sediment flux and the maintenance of vertical stratification in the estuary (e.g., Nash, 1994; Geyer & MacCready, 2014).

Numerous field and numerical studies have investigated sediment trapping in highly stratified estuaries; an excellent review of these studies is presented in the introduction of Nijs *et al.* (2010). This work has focused on sediment transport processes on intratidal and fortnightly (spring-neap) time scales. A quasi-steady hydraulic model of the salt wedge is ideal for morphodynamic applications (with model time scales on the order of 10^3 years) because it is not computationally intensive. Though it neglects the intratidal and three-dimensional

complexities inherent in a detailed analysis of sedimentary patterns in the salt wedge, it retains the key mechanistic features of the along-flow transport: 1) reduction in bed stress and particle resuspension owing to the separation of the outflowing freshwater layer from the channel bottom (e.g., Fugate & Chant, 2005); 2) the reduction in turbulence intensity and the resulting reduction in turbulent particle suspension capacity (Kostaschuk *et al.*, 1992; Geyer, 1993); 3) flocculation, resulting in enhanced deposition rates for fine sediments (e.g., Geyer *et al.*, 2004); and 4) the reduction in residence time caused by acceleration of the flow over the salt wedge, resulting in reduced deposition rates.

In Sections 3.2 and 3.3 we introduce the hydrodynamic and sediment models of the salt wedge and upstream river. However, we confine a detailed treatment of the salt wedge sediment model to Appendix A. In Section 3.4, we apply a flux balance to the model to determine if and when salt wedge formation modifies a) the magnitude of sediment export to the shelf, and b) the magnitude of deposition in the lower river, we also examine c) the peak sediment deposition rates in the estuary and upstream river. In Section 4.5, we discuss the implications of our findings for the importance of the salt wedge in morphodynamic processes in the lower river.

3.2 Hydrodynamic Model

We describe the flow hydraulically, meaning only the vertically averaged along-flow (x-direction) momentum and mass balances are considered. The hydraulic description of the salt wedge follows that presented by Poggioli & Horner-Devine (2015), who modified earlier descriptions of the salt wedge (Schijf & Schönfeld, 1953; Harleman, 1961) to include the effects of nonzero channel bed slope and variable channel width; we will consider only nonzero bed slope here. The river hydraulics are described by the gradually varied flow (GVF) equation (see, e.g., Sturm, 2010). The GVF equation was applied to sediment transport and morphodynamics in the lower river by Lamb *et al.* (2012) and Chatanantavet *et al.* (2012), though these authors did not model estuary formation. The model geometry and dependent and independent variables are shown in Figure 3.2.

We neglect tides and transients associated with changing river discharge, and therefore all unsteady terms in the equations. Shear stresses exerted on the freshwater outflow by the channel bottom in the unstratified river and by the fresh-saltwater interface in the estuary are parameterized using quadratic bottom and interfacial drag coefficients, C_b and C_i, respectively. All cross-channel and vertical fluxes of mass and momentum are neglected. We assume the salt wedge is arrested so that there is no velocity in the lower layer (layer 2 in Figure 3.2). The model geometry is characterized by a uniform channel width and bottom slope.

3.2.1 Salt Wedge

By applying conservation of momentum and fluid mass to the two-layered arrested salt wedge, we find equations for the slope of the free surface elevation η and the freshwater layer thickness h_1:

$$\frac{dh_1}{dx} = C_i \frac{F_d^2}{1 - F_d^2} \left(1 + \frac{h_1}{h_2}\right) \tag{3.1}$$

$$\frac{d\eta}{dx} = -C_i \frac{\Delta\rho}{\rho_2} \frac{F_d^2}{1 - F_d^2} \left(1 + F_d^2 \frac{h_1}{h_2}\right), \tag{3.2}$$

where h_2 is the thickness of the salt wedge, $F_d \equiv q/\sqrt{g' h_1^3}$ is the densimetric Froude number, $q \equiv Q/b$ is the specific river discharge, Q is the river discharge, b is the channel width, $g' \equiv (\Delta\rho/\rho_2)g$ is reduced gravity, and $\Delta\rho \equiv \rho_2 - \rho_1$ is the difference in density between salt and freshwater. Note that the densimetric Froude number F_d is related to the familiar open channel Froude number F by $F = \sqrt{\Delta\rho/\rho_2} F_d$. The free surface elevation is related to the layer depths and channel bed elevation by the geometric relation $\eta = h_1 + h_2 + h_b = h_1 + h_2 - S_0 x$, where S_0 is the bed slope (see Figure 3.2). The salt wedge model is derived and discussed in detail in Poggioli & Horner-Devine (2015). Note that Equations 3.1 and 3.2 apply only in the estuary because the salt wedge thickness h_2 is assumed nonzero and the freshwater layer is decoupled from the bottom and therefore experiences interfacial as opposed to bed friction.

3.2.2 Boundary Conditions

Two boundary conditions are necessary to uniquely determine the flow in the salt wedge. We obtain the first boundary condition by recognizing that the mouth of the river acts as a hydraulic control on the two layered flow, meaning that the densimetric Froude number $F_d = q/\sqrt{g' h_1^3}$ must be one at this location (Stommel & Farmer, 1952; Geyer & Ralston, 2011). This requirement uniquely relates the upper layer thickness to the river discharge. Defining $x = 0$ to be the river mouth, as shown in Figure 3.2, setting $F_d = 1$, and solving for $h_1(x = 0)$, our first boundary condition is

$$h_1(x = 0) = \left(\frac{q^2}{g'}\right)^{1/3}. \tag{3.3}$$

We obtain the second boundary condition by assuming that the elevation of the free surface at the river mouth is equal to sea level, and the water depth is therefore the shoreline depth h_S. The second boundary condition is

$$h_2(x = 0) = h_S - \left(\frac{q^2}{g'}\right)^{1/3}. \tag{3.4}$$

Integration of the coupled Equations 3.1 and 3.2 begins at the mouth and is continued landward until the lower layer thickness h_2 goes to zero at $x = -L_e$ (see Figure 3.2). A more detailed explanation of our numerical solution method is provided in Poggioli & Horner-Devine (2015).

3.2.3 Unstratified River

By following the same procedure in the unstratified river upstream of the salt wedge, we can derive the gradually varied flow (GVF) equation:

$$\frac{dh_1}{dx} = C_b \frac{F_N^2 - F^2}{1 - F^2}, \tag{3.5}$$

where $F \equiv q/\sqrt{g h_1^3} = \sqrt{\Delta\rho/\rho_2} F_d$ is the open channel Froude number, h_N is the normal depth, and $F_N \equiv q/\sqrt{g h_N^3} = \sqrt{S_0/C_b}$ is the normal flow open channel Froude number. Equation 3.5 is derived in, e.g., Sturm (2010).

A single boundary condition is needed to integrate Equation 3.5. This is provided by the solution to Equations 3.1 and 3.2, in particular the predicted water depth at the salt wedge toe, h_1^{toe}, and its location, L_e:

$$h_1^{GVF}(x = -L_e) = h_1^{toe}, \tag{3.6}$$

where h_1^{GVF} indicates the river depth profile predicted by the GVF equation, Equation 3.5. This condition expresses the requirement that the water depth be continuous at the salt wedge toe.

Integration of Equation 3.5 gives the free surface profile in the river upstream of the salt wedge. In the case of a channel of uniform width and channel bed slope, it can be solved analytically (see Bresse, 1860; Sturm, 2010).

3.2.4 Non-Dimensionalization

Too many independent dimensioned parameters have been introduced to make any headway without reducing the dimension of the parameter space. We accomplish this by non-dimensionalizing all independent and dependent variables; this procedure as applied to the salt wedge is discussed in detail in Poggioli & Horner-Devine (2015). The same procedure is applied here to the GVF equation. We divide the layer thicknesses and free surface elevation by the shoreline depth h_S, and we divide the x-coordinate and estuary length by the interfacial friction length h_S/C_i (Geyer & Ralston, 2011). This procedure, when applied to Equations 3.1, 3.2, and 3.5, and to conditions 3.3, 3.4, and 3.6, indicates that the coupled river-estuary system is governed by four independent dimensionless parameters:

$$F_f = \frac{q}{\sqrt{g' h_S^3}} \tag{3.7}$$

$$F_N = \sqrt{\frac{S_0}{C_b}} \tag{3.8}$$

$$\frac{\Delta\rho}{\rho_2} \tag{3.9}$$

$$\gamma = \frac{C_i}{C_b}. \tag{3.10}$$

The first parameter, F_f, is the freshwater Froude number. It is discussed at length in, e.g., Geyer & Ralston (2011); Poggioli & Horner-Devine (2015); Armi & Farmer (1986); in the final reference, it is referred to as the net barotropic flow and given the symbol U_0. The freshwater Froude number is an index of the ratio of the inertial and buoyant forces experienced by the river outflow, and a salt wedge forms only when $F_f < 1$ (Schijf & Schönfeld, 1953; Armi & Farmer, 1986; Geyer & Ralston, 2011; Poggioli & Horner-Devine, 2015).

The second parameter is the normal flow Froude number, already familiar to us. The third parameter, $\Delta\rho/\rho_2$ is the density difference between salt and freshwater normalized by the salt water density. It is referred to hereafter as the normalized stratification. The final parameter, $\gamma = C_i/C_b$ is the ratio of the interfacial and bottom drag coefficients; it is the reduction in drag experienced by the flow as it detaches from the channel bottom.

There are two additional physically significant parameters that may be formed from those defined in 3.7 - 3.10:

$$L^0_{e*} = \frac{C_i}{S_0} = \frac{\gamma}{F_N^2} \tag{3.11}$$

$$\frac{h_S}{h_N} = \left[\left(\frac{\Delta\rho}{\rho_2}\right)^{-1}\left(\frac{F_N}{F_f}\right)^2\right]^{1/3}. \tag{3.12}$$

The first parameter, L^0_{e*}, is the maximum salt wedge intrusion length, $L^0_e = h_S/S_0$, non-dimensionalized as all other horizontal length scales by the interfacial friction length, h_S/C_i. The subscript star indicates in general that a quantity has been non-dimensionalized, and the superscript zero indicates that the maximum intrusion length occurs in the limit that the river discharge goes to zero. This quantity, and the implications of slope-limitation for the structure and extent of the salt wedge, are discussed by Poggioli & Horner-Devine (2015). We note here that, for a given freshwater Froude number, the value of L^0_{e*}, and therefore the non-dimensionalized salt wedge length $L_{e*} = C_i L_e/h_S$ decreases with increasing bottom slope.

The second parameter indicates whether a river of normal depth h_N flowing into a basin of the same density and shoreline depth h_S would be in a state of backwater, $h_S/h_N > 1$, or drawdown $h_S/h_N < 1$. The case presented here is complicated by the formation of the

salt wedge, and we cannot determine whether the flow is in backwater or drawdown from the value of h_S/h_N alone.

The ratio h_S/h_N, and possibly the slope limited non-dimensionalized intrusion length L^0_{e*}, may be regarded as more intuitively appealing parameters than any of the drag coefficient ratio $\gamma = C_i/C_b$, the non-dimensionalized stratification $\Delta\rho/\rho_2$, or even the freshwater Froude number F_f; However, we retain the latter parameters because they are more well-constrained than h_S/h_N, which varies greatly with discharge, and L^0_{e*}, which, like F_N, varies with the bottom slope. Our model differs from that presented in Lamb *et al.* (2012) and Chatanantavet *et al.* (2012) only when a salt wedge forms, and a salt wedge forms only when $F_f < 1$; therefore, we need only consider the range $0 < F_f < 1$. Typical values of $\Delta\rho/\rho_2$ are around 0.02 (e.g. Rattray & Mitsuda, 1974). The interfacial drag coefficient has been found to be approximately $4 - 5(10^{-4})$ (Sorgard *et al.*, 1990; MacDonald & Geyer, 2004), and the bottom drag coefficient is on the order of $3(10^{-3})$ (e.g., Fugate & Chant, 2005). Together this gives $\gamma \approx 0.13$. Though we have explored the sensitivity of our results to both γ and $\Delta\rho/\rho_2$, we will present our results assuming $\gamma = 0.13$ and $\Delta\rho/\rho_2 = 0.02$; our results are relatively insensitive to the normalized stratification, and, while interesting effects do occur when the drag coefficient is not constrained to be $O(0.1)$, these occur only for values of γ to small to be physically realistic.

3.3 Sediment Model Development

3.3.1 Unstratified River

In the upstream river, we model the specific (per unit width) total volumetric sediment load q_{sed} using the results of Engelund & Hansen (1967):

$$\frac{q_{sed}}{(q_{sed})_N} = \left(\frac{h_1}{h_N}\right)^{-5}, \tag{3.13}$$

where we have normalized q_{sed} by the specific sediment load at normal flow, $(q_{sed})_N$. The latter can be found by using

$$q_{sed} = \sqrt{Rgd_{50}^3}\left(\frac{0.05}{C_b}\right)\tau_*^{5/2}, \tag{3.14}$$

where R is the submerged sediment specific gravity (1.65 for quartz), d_{50} is the median grain size, and $\tau_* \equiv \tau/R\rho g d_{50}$ is the Shields parameter. In normal flow in a wide channel, $\tau_* = S_0 h_N/Rd_{50}$.

3.3.2 Salt Wedge

Within the salt wedge, we model the sediment load as a vertically homogeneous plug that settles with the particle settling velocity w_s, as shown in Figure 3.3a. We integrate w_s over the particle transit time from the toe to the mouth to find the vertical distance settled by the sediment column before it leaves the estuary. We then calculate the fraction of sediment that has been settled into the salt wedge as the ratio of the settled distance to freshwater thickness at the mouth. Dividing by the local freshwater layer thickness takes account of the tendency of the sediment to be advected with the flow over the salt wedge. Implicitly, by assuming the net settling rate of the sediment is equal to its settling velocity, we have assumed that the capacity of the turbulence in the upper layer to keep particles in suspension is negligible. Turbulence suppression and associated deposition is indeed a key feature of flow over the salt wedge (e.g., Kostaschuk *et al.*, 1992; Geyer, 1993; Nijs *et al.*, 2010). We have further assumed that the salt wedge acts as a trap of sediment; sediment can be resuspended only by an increase in discharge forcing the toe to move seaward and exposing previously deposited sediment. (We will not examine this process here.)

A more complete mathematical treatment of this model is given in Appendix A; there we derive equations for the fraction of sediment deposited in the estuary f_D and the sediment flux to the shelf, normalized by the normal flow specific sediment discharge, $E \equiv q_{sed}(x = 0)/(q_{sed})_N$ (Equations A.5 and A.7). They are

$$E = (1 - f_D)E_0(h_{1*}^{toe})^{-5} \tag{3.15}$$

$$f_D = \min\left(\frac{Ro_d}{F_f^{5/3}}\int_{-L_{e*}}^{0} h_{1*}dx_*, 1\right), \tag{3.16}$$

where $E_0 = (h_S/h_N)^{-5}$ is the export in the case of no salt wedge formation, and h_{1*}^{toe} is the water depth at the toe normalized by h_S. The parameter $Ro_d \equiv w_s/C_i\sqrt{g'h_S}$ is referred to here as the densimetric Rouse number; $\sqrt{g'h_S}$ is a scale of the velocity over the salt wedge, so that $\sqrt{C_i g'h_S}$ is a scale of the friction velocity $u_f = \sqrt{\tau/\rho}$, and therefore the parameter $Ro_d \sim w_s/u_f$, like the ordinary Rouse number. We take the minimum of the integral in Equation 3.16 and 1 because $f_D = 1$ indicates all of the sediment in the water column has settled out.

We assume predominantly fine sediments and a mean flocculated settling velocity of 1 mm/s (Geyer *et al.*, 2004). Assuming a typical normalized stratification of $0.01 - 0.02$, an interfacial drag coefficient of $4(10^{-4})$, and shoreline depths in the range $10 - 30$ m gives values of Ro_d in the range $1 - 3$. We will take a mean value of 2 to be characteristic of flocculated fine sediment. In Section 3.4.1, we will investigate the sensitivity of the export fraction E/E_0 to densimetric Rouse number.

In addition to the export to the shelf, we are interested in the depositional fluxes in the estuary and in the upstream river, D_e and D_u, respectively, the total deposition in the lower river, $D = D_e + D_u$, and the export from the upstream river into the estuary E_{toe}. An equation for E_{toe} is found in Appendix A (Equation A.6). The remaining fluxes are found by performing a sediment mass balance on the control volumes sketched in Figure 3.3b:

$$1 = D_u + E_{toe} \tag{3.17}$$

$$E_{toe} = D_e + E \tag{3.18}$$

$$1 = D + E. \tag{3.19}$$

Note that the fluxes D, D_u, and D_e are *net* depositional fluxes–in our definition, erosion is negative net deposition, corresponding to, e.g., $D < 0$.

Equations 3.17 - 3.19 are equally valid when salt wedge formation is neglected. In this case, we add a subscript 0; D_{e0}, e.g., is then interpreted as the deposition in the region

that would be occupied by the salt wedge if it were modeled. The interpretations of D_{u0} and E_{toe0} follow similarly. This approach allows us to directly quantify the difference in the predictions between the present model and one that neglects salt wedge formation for both the magnitude and spatial distribution of sediment export and deposition.

3.4 Results

In this section, we address our three questions regarding the influence of the salt wedge on the sediment dynamics in the lower river: does the salt wedge modify, and if so under what conditions, a) sediment export to the shelf, b) the net deposition in the lower river, and c) the distribution of deposited sediment in the lower river? We address the first question by calculating the ratio of the normalized sediment export to the export when salt wedge formation is neglected, E/E_0; whether this ratio is greater or less than one tells us whether salt wedge formation attenuates or enhances export to the shelf. We determine the effect of salt wedge formation on net deposition in the lower river by calculating the ratio of the net normalized depositional fluxes with and without a salt wedge, D/D_0. Again, whether this ratio is greater or less than one tells us if salt wedge formation enhances or diminishes the total net deposition in the lower river. Finally, we assess a shift in the location of maximum deposition rate within the lower river due to salt wedge formation. The deposition rate $d = dD/dx = -dq_{sed}/dx$ is proportional to rate of increase of channel bottom elevation $\partial h_b/\partial t$. The location of the point of maximum deposition / bed aggradation is important because it has been suggested that the process of bed aggradation / channel filling is what ultimately motivates channel avulsion Chatanantavet *et al.* (2012). Thus, the peak in deposition rate may be related to the avulsion length.

We plot each of these quantities against freshwater Froude number, which is our non-dimensional proxy for the river discharge ($F_f \sim Q$). Typically, we will also plot for a range of values of F_N, which is our proxy for bed slope ($F_N \sim S_0^{1/2}$). Unless noted otherwise, we assume $C_i = 4(10^{-4})$, $C_b = 3(10^{-3})$, $\Delta\rho/\rho_2 = 0.02$, and $Ro_d = 2$.

3.4.1 Export of Sediment to the Shelf

Figure 3.4 shows the export ratio E/E_0 as a function of freshwater Froude number for several values of the normal flow Froude number. The curves are colored based on the value of F_N, as indicated in the colorbar. We give approximate values of the bed slope, assuming $C_b = 3(10^{-3})$, next to the colorbar. In all cases, $E/E_0 \rightarrow 1$ as $F_f \rightarrow 1$; this is because, as $F_f \rightarrow 1$, the estuary is washed out of the channel and there is no salt wedge to modify the export. Each of the curves also falls to zero for a finite value of F_f that decreases with increasing bottom slope. This is the freshwater Froude number for which $f_D = 1$. The freshwater Froude numbers are large compared to values of F_f that are often seen in the field, which are on the order of 0.01 to 0.1 (Poggioli & Horner-Devine, 2015). That rivers do not export large volumes of sediment during low discharge events is unsurprising, except that the cutoff freshwater Froude number is large compared to typical values, indicating that the estuary is a very effective trap of sediment during ordinary discharge conditions. In the Mississippi, for example, the slope in the lower reach is $\sim 4.5(10^{-5})$, giving $F_N \approx 0.12$ and a minimum F_f for export of ~ 0.4 (see Figure 3.4, Section 3.4.2). The depth at Head of Passes, which in this case is the hydraulic control point (Rattray & Mitsuda, 1974), is ~ 30 m, and the depth-averaged bottom width is ~ 520 m (Lamb *et al.*, 2012). This gives a minimum discharge to force export of $Q \approx 1.5(10^4)$, the one-year flood (Lamb *et al.*, 2012). This highlights the efficiency of the salt wedge as a sediment trap during typical flow conditions.

The behavior of the export fraction varies substantially in the intermediate freshwater Froude number range. Examining the inset in Figure 3.4, we see that for $F_N >\sim 0.4$ ($S_0 \approx 5(10^{-4})$), there is a peak in E/E_0 that is greater than one, indicating an enhancement of export caused by the intrusion of the salt wedge. This peak rapidly grows in magnitude and shifts to lower values of F_f as the bottom slope increases. This enhancement of sediment export is due to the decrease in residence time caused by the salt wedge; the intrusion of salt water confines the flow to a narrower portion of the water column, and it must therefore accelerate to conserve fluid mass. This effect is in competition with the suppression

of sediment resuspension caused by the decoupling of the outflow from the channel bed. Ultimately, for sufficiently low freshwater Froude numbers, the latter mechanism wins out, and the estuary inhibits export to the shelf, retaining all of the sediment delivered to it from the upstream river.

We note that, though the enhancement of sediment export caused by the salt wedge can be significant–the peak of the $F_N = 1$ curve in Figure 3.4 is ~ 5.5–this effect occurs only when the discharge is low to moderate and the bed slope is steep ($S_0 >\sim 4.8(10^{-4})$). This corresponds to large values of h_S/h_N and consequently small values of $E_0 = (h_S/h_N)^{-5}$. Thus, though the export may be enhanced relative to the export that would be predicted if salt wedge formation were neglected, i.e., E_0, E_0 itself is a small fraction of the normal sediment load. Enhancement of export is confined to a region of parameter space where essentially all of the sediment is deposited in the river (see Section 3.4.2).

In Figure 3.5, we show the behavior of the export fraction with F_f for $F_N = 1$ (for which the peak in E/E_0 is maximized) for four different values of the densimetric Rouse number: 1, 2, 3, and 10. The first three values are within those typical of flocculated fine sediments; the fourth value, $Ro_d = 10$ is typical of fine sand. The magnitude and location of the peak in E/E_0, as well as the cutoff freshwater Froude number below which the estuary is fully retentive, is highly sensitive to Ro_d. However, we note that the enhancement of the export is present across the range of values of Ro_d anticipated for flocculated fine sediment, and that there is minor enhancement even for fine sand, as shown in the inset in the Figure. In addition to being directly proportional to the mean settling velocity, Ro_d is inversely proportional to the square root of the shoreline depth, indicating that relative export enhancement (large peak in E/E_0) increases with estuary depth. However, the peak in E/E_0 also shifts to lower values of F_f for increasing Ro_d, eventually resulting in diminished values of E_0. Therefore, the absolute maximum in peak export is anticipated to occur at finite values of Ro_d.

3.4.2 Deposition of Sediment in the River

Figure 3.6 shows the deposition ratio D/D_0 as a function of freshwater Froude number for several values of the normal flow Froude number, similar to 3.4. We again give approximate values of S_0. For each value of F_N, $D/D_0 \to 1$ as $F_f \to 1$; as noted above, this is because the models are indistinguishable when the salt wedge is washed out at $F_f = 1$. Moving in the direction of decreasing F_f, we next note that $D/D_0 \to \pm\infty$ for only two of the curves, those with the lowest normal flow Froude numbers ($F_N = 0.1$, 0.13, $S_0 \approx 3(10^{-5})$, $5(10^{-5})$). This discontinuity corresponds to the point where $h_S/h_N = 1$; in this case, if there were no salt wedge, the normal flow zone would extend all the way to the mouth, and there would be no deposition in the channel. For these small slopes, a salt wedge can intrude when $h_S = h_N$; intuitively, one would expect that this is the result of enhanced deposition within the salt wedge; however, Figure 3.7 (discussed below) indicates that this is not the case. $D/D_0 \to +\infty$ as we approach from the left (lower F_f / Q) because, in this direction, we transition from backwater $h_S/h_N > 1$ to drawdown $h_S/h_N < 1$, and the deposition in the no salt wedge case (D_0) is positive but approaching zero. D remains finite when D_0 approaches zero, and $D/D_0 \to +\infty$. Similarly, as we approach from the right, we transition from drawdown to backwater; drawdown causes erosion, resulting in $D_0 < 0$. The salt wedge always has the effect of increasing the deposition, and in a very small region in the vicinity of the transition ($h_S/h_N = 1$), this effect is enough to overwhelm erosion caused by drawdown, and $D/D_0 < 0$. However, by comparing with Figure 3.4, we see that, at these low slopes / normal flow Froude numbers, even though the intrusion of the salt wedge causes deposition in the channel where there would be bypass or erosion, E/E_0 remains within a few percent of 1.

To the left of this discontinuity (lower F_f / Q), each curve shows a peak in D/D_0. This peak coincides with the value of F_f at which all of the sediment that enters the salt wedge is deposited within the salt wedge; this is illustrated in the inset, which shows the normalized deposition with and without the salt wedge D, D_0. When the salt wedge is

modeled, $D \to 1$ for a nonzero value of F_f. At low slopes, this discrepancy is significant; when $F_N = 0.1$ ($S_0 \approx 3(10^{-3})$), the salt wedge results in up to nearly 15% (see Figure 3.7) more deposition in the vicinity of $F_f \approx 0.4$, where the salt wedge becomes completely depositional. However, this effect is reduced dramatically with increasing bottom slope; h_S/h_N increases with increasing F_N (slope) for a given F_f (discharge), resulting in a more extreme backwater and a larger D_0, and consequently reducing the discrepancy in deposition between the salt wedge and no salt wedge cases.

Figure 3.7 shows the total deposition anomaly $D - D_0$ and the deposition anomaly in the estuary $D_e - D_{e0}$ for $F_N = 0.1$. The total deposition anomaly is colored based on whether $D > 0$, indicating net deposition (blue), or $D < 0$, indicating net erosion (red). When the two curves coincide, excess deposition caused by the salt wedge is contained within the salt wedge. This is the case for the peak in D/D_0 located at $F_f \approx 0.4$ (see Figure 3.6). However, it is not the case in the vicinity of the freshwater Froude number for which $h_S/h_N = 1$. This indicates that the enhanced deposition for increasing flows approaching the transition from backwater to drawdown, and the diminished erosion for decreasing flows approaching the transition from drawdown to backwater, is not caused by the deposition of sediment in the salt wedge. Instead, it is caused by the influence of the salt wedge on the upstream water surface profile. It can be shown that water surface slope in the salt wedge scales as $d\eta_{SW}/dx \sim -C_i$ over the bulk of the intrusion, whereas the elevation of the normal depth line follows the channel bed slope by definition and therefore has a slope of $-S_0$. If $S_0 \ll C_i$, the free surface slope over the salt wedge can force the upstream profile from normal flow or drawdown into backwater, thus enhancing deposition upstream of the salt wedge. The inverse scenario, in which the intruding salt wedge forces drawdown, requires $S_0 \gg C_i$ and is unlikely to be observed in real systems because this requires that F_N ($\sim S_0^{1/2}$) be large, and thus the freshwater Froude number at which $h_S/h_N = 1$, $(F_f)_{trans} = (\Delta\rho/\rho_2)^{-1/2} F_N$ (from Equation 3.12) is likely to be > 1, preventing salt wedge formation.

3.4.3 Location of Maximum Deposition

Figure 3.9 shows the magnitude of the peak deposition in the upstream river and in the salt wedge as a function of freshwater Froude number for three different values of the normal flow Froude number: $F_N = 0.1$, 0.2, and 0.25. The deposition is calculated as the negative gradient of the normalized specific sediment flux: $d_* = -d/dx_*[q_{sed}/(q_{sed})_N]$, where the subscript $*$ on d_* indicates that it is non-dimensionalized by $(q_{sed})_N/(h_S/C_i)$. This scaling is important to keep in mind when looking at Figure 3.9; though it appears that the peak deposition rate in the upstream river becomes very large as $F_f \to 0$, this rate is normalized by the normal flow sediment load, which becomes very small at low discharges. Therefore, there will be a peak in the dimensioned deposition rate at a nonzero value of the river discharge, corresponding to a maximum in the product of $(q_{sed})_N$ and d_*.

The location of the peak deposition in the upstream river scales with the hydraulic transition length L_t (Chatanantavet *et al.*, 2012), whereas the peak deposition in the salt wedge is very near the toe and therefore scales with the estuary length L_e. The rate of sediment deposition is proportional to the rate of bed aggradation. Based on hydraulic modeling of the Mississippi, Chatanantavet *et al.* (2012) identified the location of maximum channel aggradation associated with the backwater zone as a mechanism that potentially sets the channel avulsion scale. According to this view, the channel filling associated with deposition in the backwater zone is what eventually initiates channel avulsion. The upper two panels of Figure 3.9 indicate that for low normal flow Froude numbers ($F_N <\sim 0.2$, $S_0 <\sim 1.2(10^-4)$) the peak depositional rate in the salt wedge exceeds that in the upstream river above a critical value of the freshwater Froude number. (This value is indicate in Figure 3.9.) This suggests that the salt wedge introduces a second length scale associated with large depositional rates and rapid channel filling on geological timescales. This effect is most pronounced only for low to moderate bottom slopes. For steep rivers, the peak depositional rate in the upper river always greatly exceeds that in the salt wedge. Morphodynamic modeling like that conducted by Chatanantavet *et al.* (2012) is necessary to determine the

implications of this second deposition length scale on geological time scales.

3.5 Discussion and Conclusions

We have developed a hydraulic model of sediment transport in highly stratified estuaries and coupled it to a hydraulic model of the hydrodynamics and sediment transport in the upstream river. The salt wedge sediment model is based on the dynamics of a sediment plug that is deformed by and advected with the mean flow while settling into the retentive salt wedge with a uniform settling velocity (see Figure 3.3a, Section 3.3.2). While we have neglected the complexities of tidal variations in the length and structure of the estuary on daily and fortnightly (i.e., tidal) timescales, we have retained the key mechanistic features of along-flow sediment transport in a salt wedge estuary. These are 1) the decoupling of the flow from the river bed and the associated reduction in bed stress and particle suspension (e.g. Fugate & Chant, 2005); 2) the suppression of turbulence in the flow over the salt wedge and associated reduction in the capacity of the turbulence to keep particles in suspension (Kostaschuk *et al.*, 1992; Geyer, 1993; Nijs *et al.*, 2010); 3) flocculation, resulting in enhanced settling velocities for fine sediments (e.g. Geyer *et al.*, 2004), and 4) the reduction in particle residence time caused by flow acceleration over the salt wedge, and the resultant reduction in the local deposition rate. The model is one-dimensional and quasi-steady, making it computationally unintensive and ideal for morphodynamic applications, with model times on the order of 10^3 years.

As a first step towards characterizing the general influence of the salt wedge on sediment dynamics in the lower river, we applied a flux balance to the estuarine and upstream river regions (see Figure 3.3b) in order to determine the relative change in export to the shelf and net deposition in the lower river caused by the salt wedge. We found that export is enhanced significantly by the salt wedge in steep rivers at moderate to low discharges; however, enhancement occurs only when the backwater is extreme and there is likely to be little export with or without the salt wedge (Section 3.4.1). The net deposition in the lower river is enhanced by salt wedge formation in low-grade rivers, having slopes smaller than

10^{-4}. There are two distinct signals of the salt wedge in the net deposition: 1) a peak in the deposition enhancement (D/D_0) occurring at the value of F_f for which the salt wedge becomes fully retentive ($f_D = 1$), and 2) an increase in deposition or reduction of erosion for very shallow slopes ($S_0 <\sim 6(10^{-5})$) associated with salt wedge intrusion during normal flow or drawdown events. Both effects decrease rapidly with increasing bottom slope / normal flow Froude number.

The results of the export and deposition calculations suggest that the estuary has a negligible effect on the bulk characteristics of sedimentation in the lower river over much of the parameter space. This is because the estuary typically occupies a small fraction of the hydraulic transition zone; even though the salt wedge dramatically alters the sediment transport in the estuary, this often affects only a small fraction of the sediment that enters the lower river. However, in low-grade rivers (slopes on the order of 10^{-5}), the salt wedge can become quite extensive, with a length approaching the backwater length. In this case, the salt wedge can potentially significantly enhance deposition in the lower river (see Figure 3.6). An example is the Mississippi, which has a bottom slope of $\sim 4.5(10^{-5})$; the backwater length in the Mississippi is on the order of 500 km (Lamb *et al.*, 2012). Maximum salt wedge intrusion lengths in the Mississippi also approach 400 to 500 km (Rattray & Mitsuda, 1974). In this case, the salt wedge has the potential to significantly modify the volume of sediment retained in the lower river. Additionally, the salt wedge alters the sedimentation patterns in the vicinity of the mouth, and it acts as an effective trap of sediment, preventing export up to moderately large values of the river discharge (on the order of the one year flood in the Mississippi, see Section 3.4.1). Our results suggest that the role of the salt wedge in modifying the net volumetric sediment balance across the hydraulic transition zone and estuary in low-grade rivers like the Mississippi, as well as the modification of sedimentation processes in the vicinity of the river mouth caused by salt wedge intrusion, cannot be excluded entirely in a morphodynamic context.

In order to determine the potential of the salt wedge to cause localized channel bed aggradation, we compared the magnitude of the peak depositional rate in the upstream

river to that in the salt wedge (Figure 3.9, Section 3.4.3). The location of the peak in the upstream deposition scales with the hydraulic transition length, whereas the location of the peak deposition in the salt wedge scales with the estuary length. We found that, at small to intermediate bottom slopes ($S_0 <\sim 1.2(10^{-4})$), the peak deposition in the salt wedge can exceed the peak deposition in the upstream river above a certain value of the freshwater Froude number that increases with increasing F_N. This suggests that, in low to moderate grade rivers ($\leq\sim 1.5(10^{-4})$), the estuary length L_e is possibly a second length scale (in addition to the transition length L_t) associated with localized channel filling. Chatanantavet *et al.* (2012) suggested that the peak in deposition and channel aggradation associated with the backwater zone may set the avulsion length scale in the Mississippi. The present results suggest that deposition in the salt wedge may be sufficiently localized near the toe to also be relevant to the avulsion process. Morphodynamic modeling that captures the influence of bed evolution on the salt wedge is necessary to determine the potential for a geological signature of the salt wedge deposition peak.

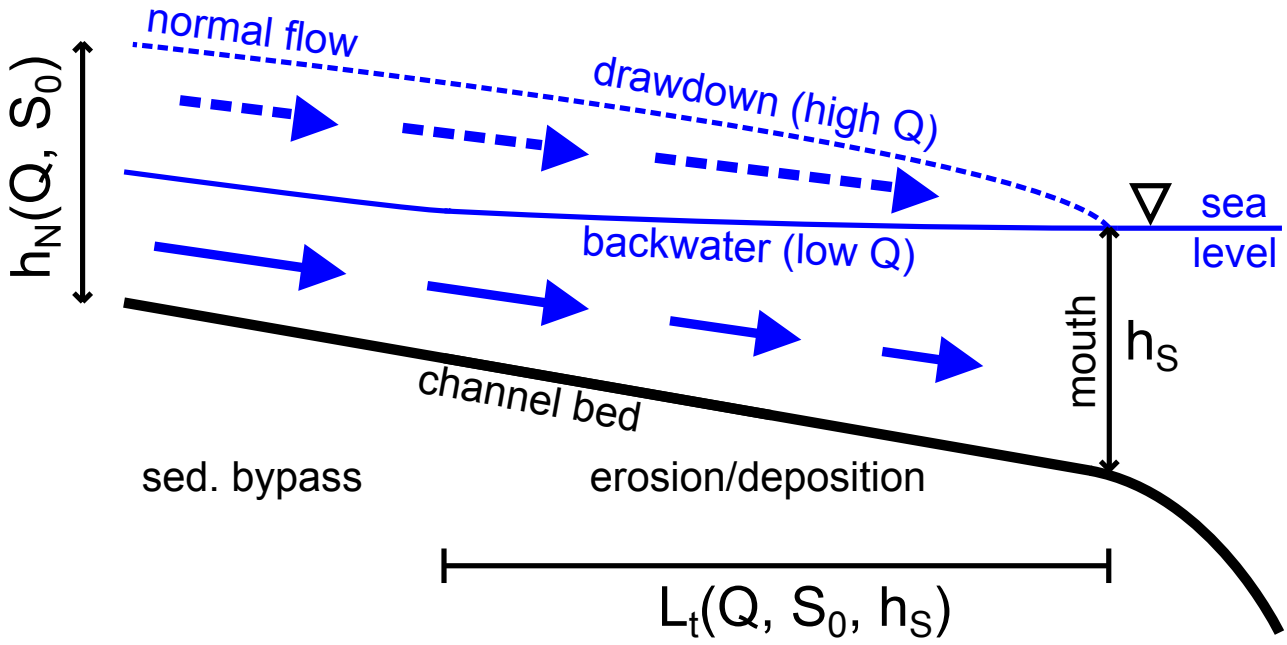

Figure 3.1: Schematic illustrating the free surface and mean flow profiles in the hydraulic transition and normal flow zones for backwater and drawdown events. The transition length is designated L_t and is a function of river discharge Q, bed slope S_0, and the shoreline depth h_S. Normal flow and net sediment bypass exist upstream of the hydraulic transition zone. Whether the hydraulic transition zone is in backwater (deceleration, deposition) or drawdown (acceleration, erosion) is determined by the ratio of the normal depth h_N to the shoreline depth h_S.

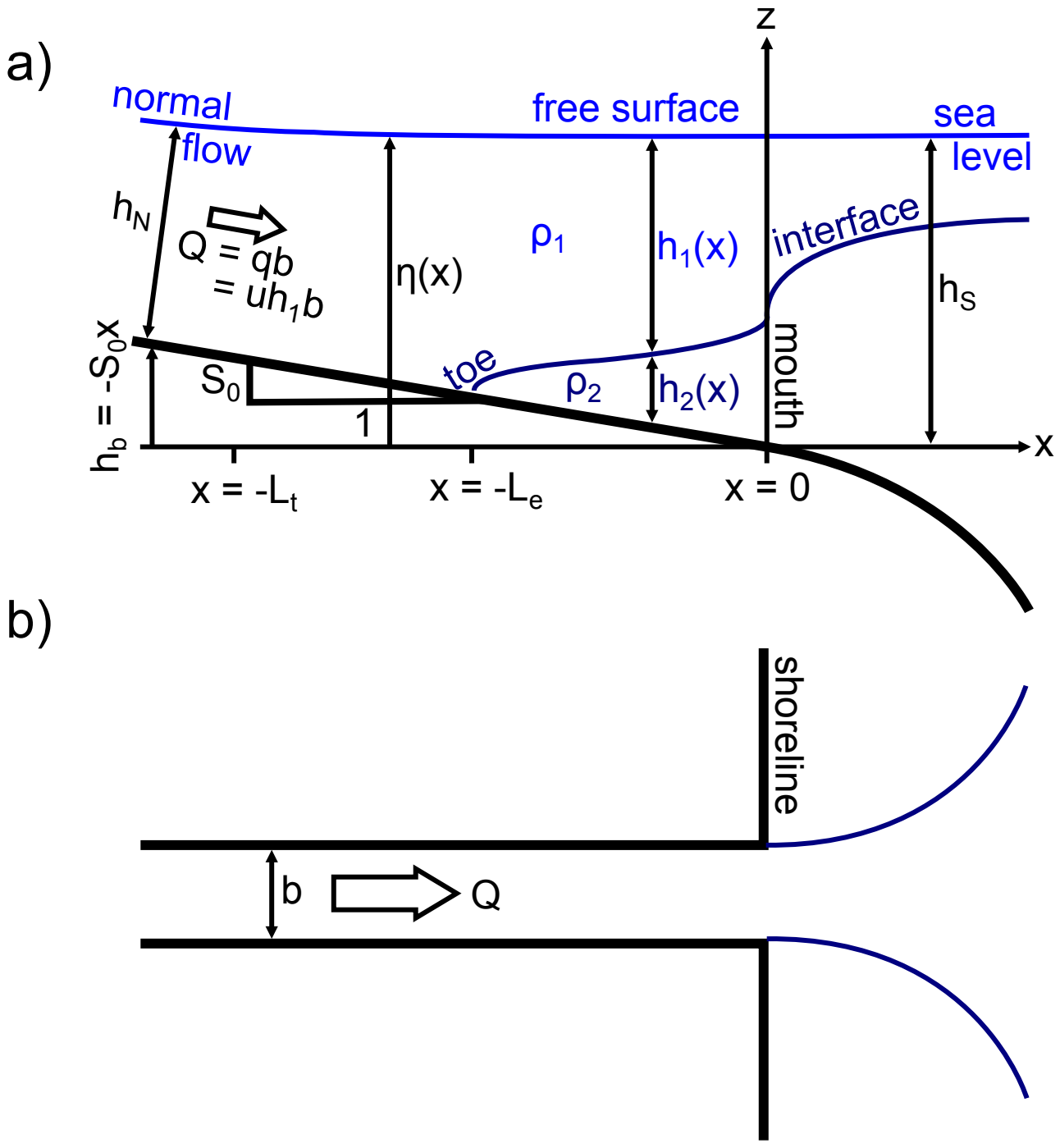

Figure 3.2: Schematic illustrating the a) side and b) plan view geometry of the hydrodynamic model. Also indicated are all independent and dependent hydrodynamic variables. The interface indicated in the Figure is that between fresh and saltwater; the intrusion landward of the mouth is the salt wedge.

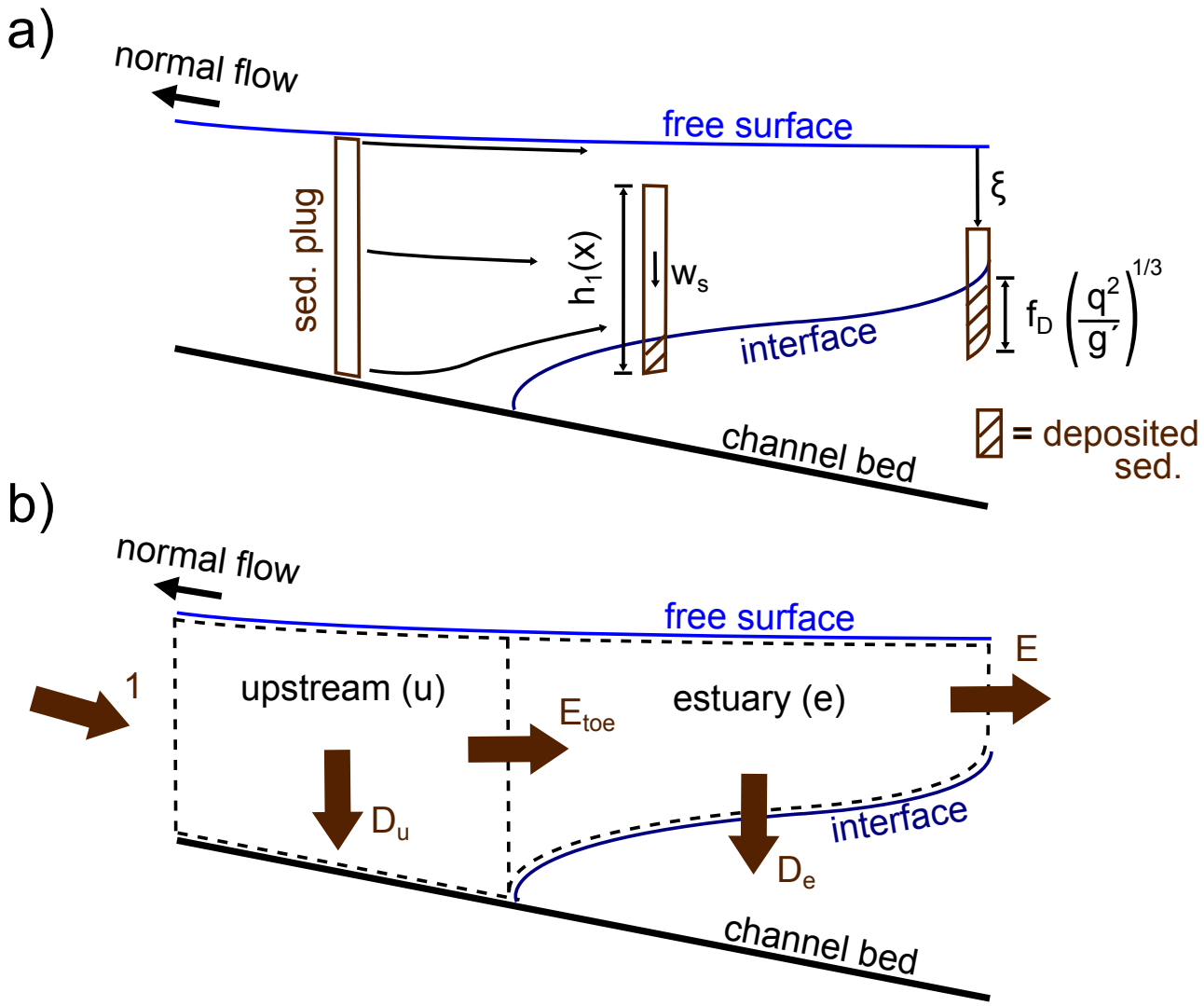

Figure 3.3: a) Schematic illustrating the salt wedge sediment model. The sediment is modeled as a homogeneous plug of settling velocity w_s. The height of the plug is assumed to be the local freshwater layer thickness $h_1(x)$, accounting for the tendency of the sediment to be advected over the salt wedge. The ratio of distance settled by the plug ξ to the freshwater depth at the mouth $h_1(x = 0) = (q^2/g')^{1/3}$ gives the deposition fraction f_D in the estuary. b) Schematic illustrating the upstream and estuary control volumes; also shown is the sediment flux into the upstream river (numerically unity because it is normalized by the normal flow flux), the deposition flux in the upstream river (D_u), the export of sediment from the upstream river to the salt wedge (E_{toe}), the deposition flux in the estuary (D_e), and the export to the shelf E.

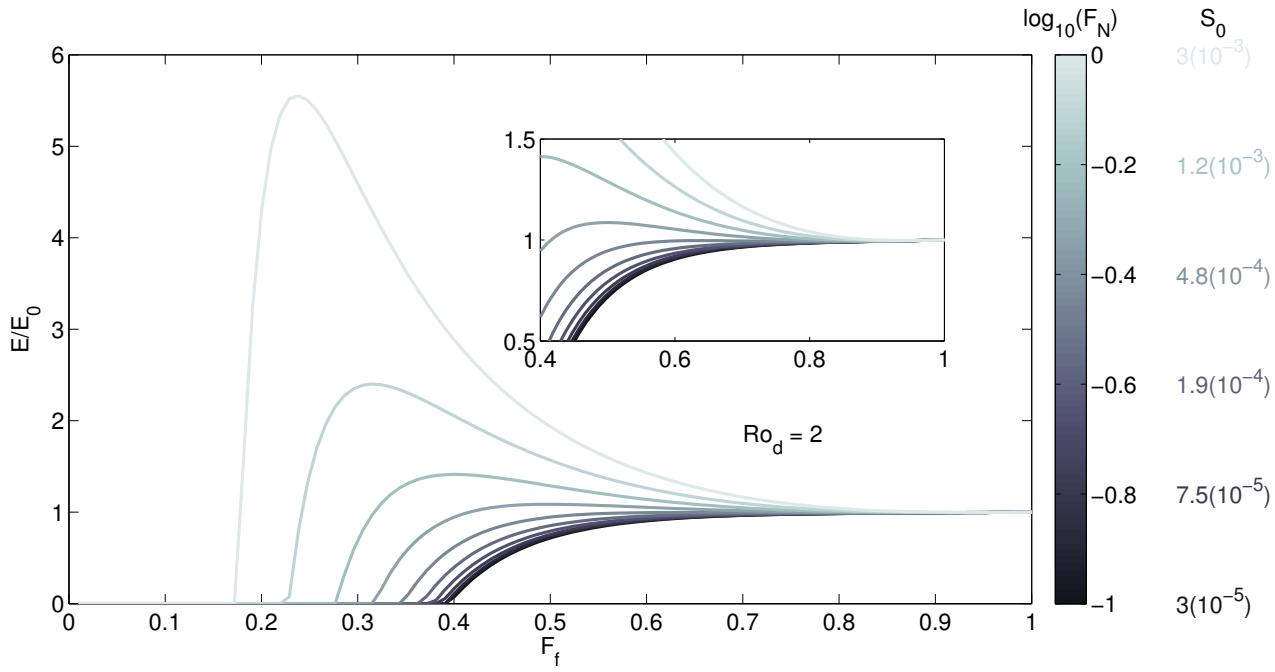

Figure 3.4: Export from the channel to the shelf E normalized by the export predicted if salt wedge formation is neglected E_0 as a function of freshwater Froude number, which varies directly with the river discharge Q. The curves are colored by the value of F_N, and the corresponding approximate value of the slope S_0 is shown next to the colorbar, assuming $C_b = 3(10^{-3})$. All curves are calculated assuming $Ro_d = 2$, as noted in the Figure. The inset plot shows the same curves with the axes truncated, indicating that export is enhanced for $F_N >\sim 0.4$ (see text).

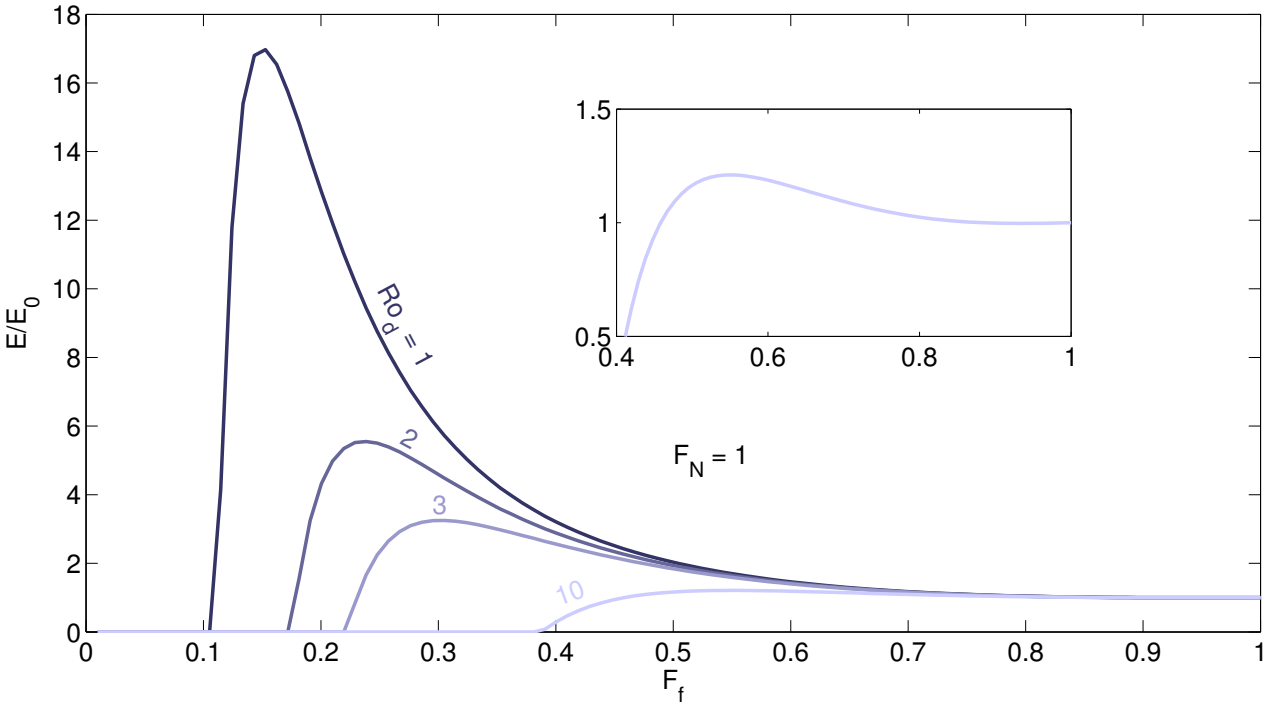

Figure 3.5: Export from the channel to the shelf E normalized by the export predicted if salt wedge formation is neglected E_0 as a function of freshwater Froude number. Each curve corresponds to a different value of the densimetric Rouse number, Ro_d; from top to bottom, $Ro_d = 1$, 2, 3, 10. All curves are calculated for $F_N = 1$, as noted in the Figure. The inset plot shows the $Ro_d = 10$ curve, indicating that export is enhanced even at this value of Ro_d when $F_N = 1$.

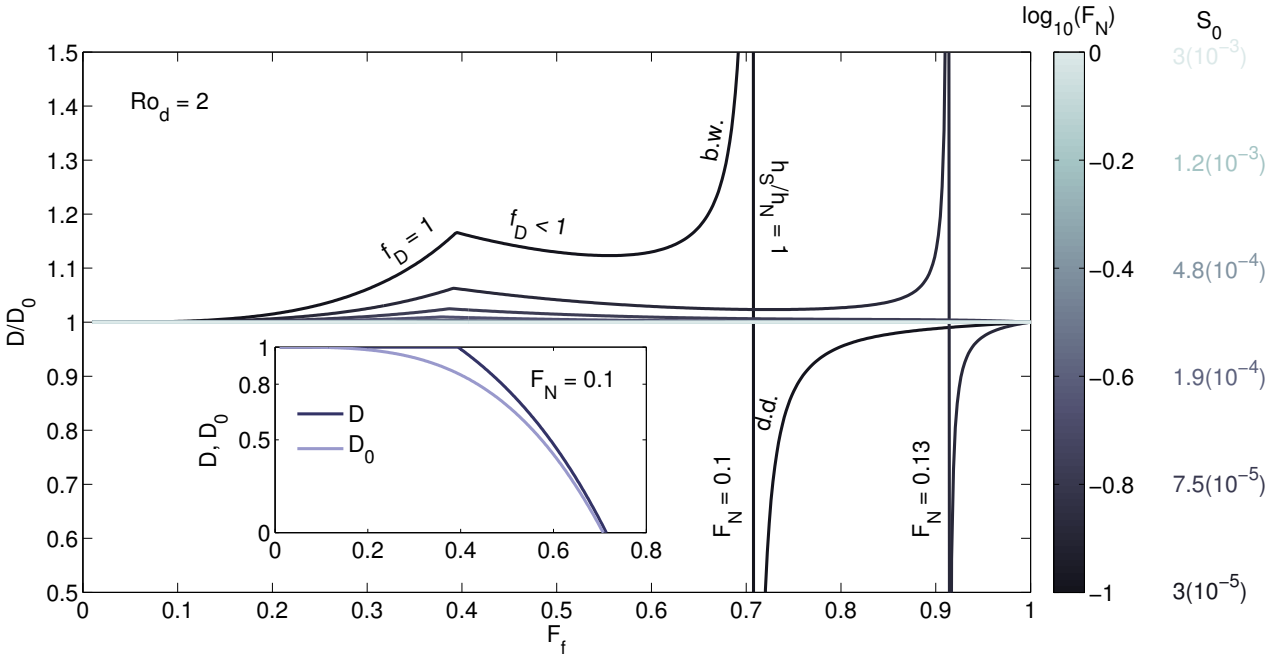

Figure 3.6: Deposition in the lower river (hydraulic transition zone and estuary) D normalized by the deposition predicted if salt wedge formation is neglected D_0 as a function of freshwater Froude number. The curves are colored by F_N, and the corresponding approximate value of the slope S_0 is shown next to the colorbar, assuming $C_b = 3(10^{-3})$. All curves are calculated assuming $Ro_d = 2$, as noted in the Figure. The values of F_N corresponding to the two curves showing the greatest modification of deposition are shown next to the vertical discontinuities in these curves (lower right). On the $F_N = 0.1$ curve, the regions where the salt wedge is fully depositional ($f_D = 1$) and is not fully depositional ($f_D < 1$), as well as where the river transitions from backwater (b.w.) to drawdown (d.d.) at $h_S/h_N = 1$, are indicated. The inset shows the deposition normalized by the normal flow sediment flux with and without the salt wedge D, D_0 for $F_N = 0.1$.

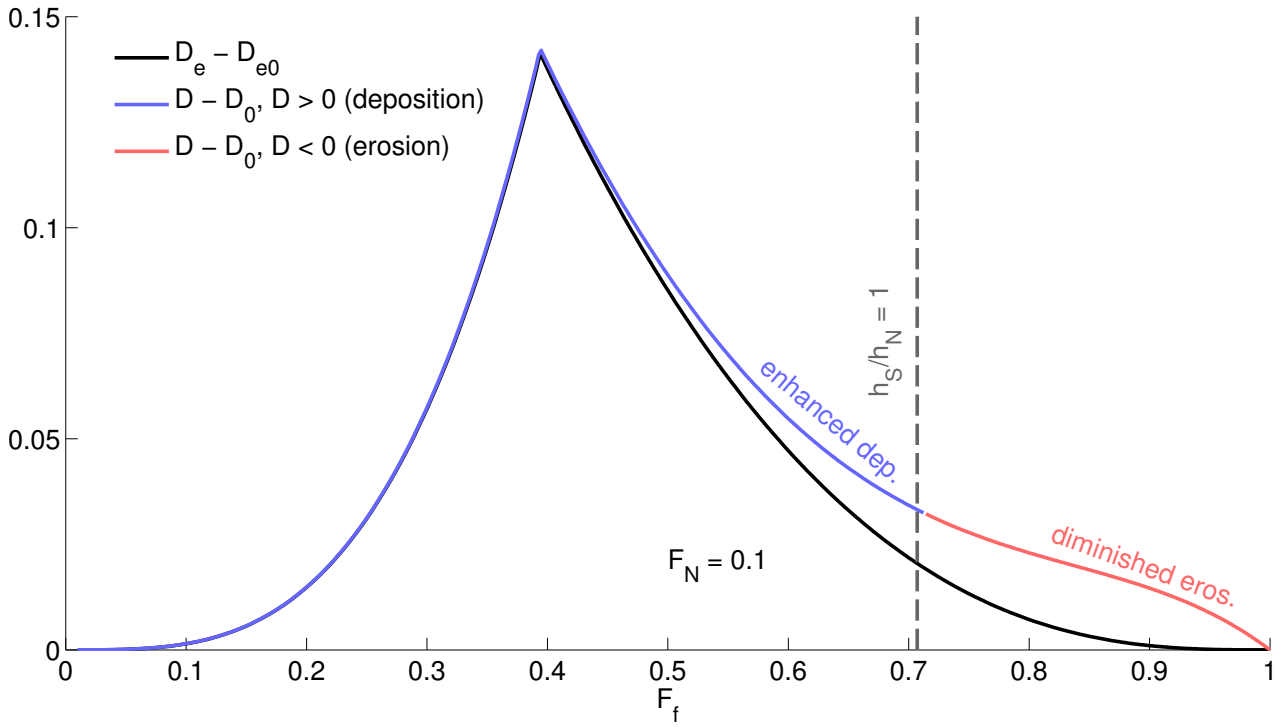

Figure 3.7: Plots of the difference in total deposition in the lower river and deposition in the estuary caused by estuary formation, $D - D_0$ and $D_e - D_{e0}$, respectively. The total deposition anomaly ($D - D_0$) curve is colored according to whether the river is net depositional (blue, $D > 0$) or erosional (red, $D < 0$). Labeled are regions of enhanced deposition and diminished erosion *outside of the estuary*. The vertical dashed gray line indicates the the value of F_f for which $h_S/h_N = 1$, which would indicate transition from backwater to drawdown (with increasing F_f / Q) if no salt wedge formed. These curves are calculated for $F_N = 0.1$, as indicated.

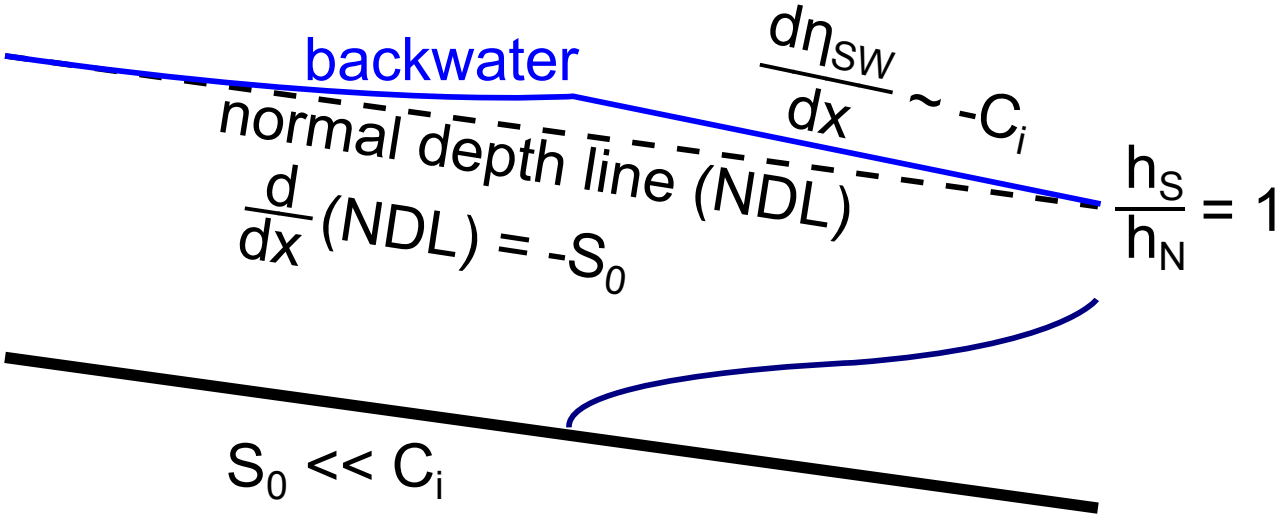

Figure 3.8: Schematic illustrating the mechanism by which a profile that would otherwise be in normal flow can be forced into backwater by an intruding salt wedge. The free surface slope scales as $-C_i$, whereas the normal depth line (NDL) has a slope of $-S_0$. Deposition outside of the salt wedge can be enhanced by this mechanism for shallow slopes ($S_0 \ll C_i$). The same principle applies if the profile would otherwise be in drawdown (i.e., if $h_S/h_N < 1$).

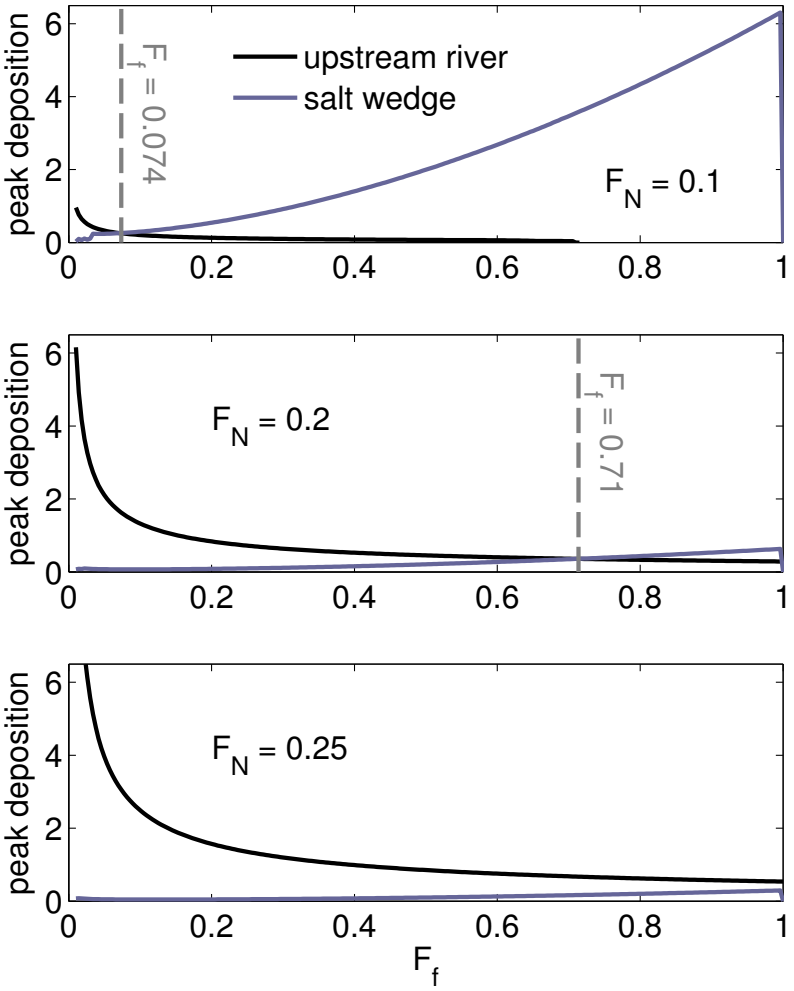

Figure 3.9: The magnitude of the peak normalized deposition in the upstream river and in the salt wedge versus F_f for three values of F_N (indicated in each panel). The location of the peak in the upstream river scales with the hydraulic transition length L_t, whereas that in the salt wedge scales with the estuary length L_e. In the first two panels, the deposition peak in the salt wedge exceeds that in the upstream river above a value of F_f indicated in the plot by a vertical dashed line.

Chapter 4

EXPERIMENTAL SIMULATION OF THE SALT WEDGE AND PLUME

4.1 Introduction

The experimental study presented in this Chapter aims to characterize 1) the length that ocean water intrudes into the river in a highly stratified salt wedge estuary in a sloped channel; and 2) the structure of the plume at high discharges (for which the estuary is expelled from the river) in order to inform morphodynamic theory and modeling efforts.

The length of intrusion of the estuary into the river is a parameter of fundamental importance to water quality managers and ecologists (Geyer & Ralston, 2011). Additionally, the magnitude of the dependence of the estuary length on the river discharge is a diagnostic parameter used to characterize the dynamics of the estuary in the field (McKeon *et al.*, 2014). This dependence is characterized by an exponent n in a power law of the form $L \sim Q^{-n}$. Previous analytical and experimental work has found that $n = 2$ to 2.5 (Schijf & Schönfeld, 1953; Keulegan, 1966); however, field and numerical studies consistently measure n in salt wedge estuaries to be in the range 0.2 to 0.6 (Ward, 1976; Ralston *et al.*, 2010; McKeon *et al.*, 2014). Furthermore, the salt wedge intrusion length is anticipated to be a morphologically important length scale in river bed evolution and deltaic morphology, as detailed in Chapter 2. For these reasons, we attempt here to determine the extent to which bottom slope modifies n and to confirm the analytical predictions presented in Chapter 2 for intrusion length as a function of discharge in a sloped estuary.

Morphodynamic models of delta progradation depend critically on the plume dynamics during high discharge events for at least two reasons. In the first place, the model of subaqueous canyon formation seaward of the river mouth suggested in the delta morphology

literature (see review by Jerolmack, 2009) depends on the formation of a rapidly depositional bottom attached and decelerating plume, in contrast to the initially accelerating plume that is discussed in the plume literature (see, e.g., Hetland, 2010; Kilcher *et al.*, 2012; Horner-Devine *et al.*, 2015). Which of the two scenarios occurs for a particular outflow is determined by the freshwater Froude number $F_f = q/\sqrt{g' h_S^3}$, where $q \equiv Q/b_0$ is the specific river discharge, Q is the volumetric river discharge, b_0 is the channel width, $g' \equiv (\Delta\rho/\rho_2)g$ is the reduced gravity, $\Delta\rho \equiv \rho_2 - \rho_1$ is the density anomaly between ocean and freshwater, and h_S is the depth of the ocean at the shoreline (see Figure 4.1). Plume bottom detachment, termed liftoff, can be forced offshore if $F_f > 1$ (see, e.g., Geyer & Ralston, 2011), but whether a plume can remain bottom attached for a significant distance from the mouth depends on the offshore evolution of the plume cross-sectional area, which determines the location of the liftoff point, and therefore on the evolution of the plume spreading profile with increasing discharge.

Secondly, it has been noted that the export of sediment to the shelf and the erosion of sediment in the lower river is determined by the formation of a drawdown zone in the vicinity of the river mouth (Lane, 1957; Chatanantavet *et al.*, 2012; Lamb *et al.*, 2012). Such a region forms when the river normal depth, the depth to which the river tends in the upstream direction, exceeds the water surface elevation at the river mouth. This results in convergence of the free surface and channel bed, flow acceleration, and sediment erosion. The magnitude of this effect depends critically on the difference between the normal depth and the free surface elevation at the shoreline η_S, but the variation of η_S with discharge is presently unknown. Results from a numerical study of the Columbia River plume presented by McCabe *et al.* (2009) suggest that the increase in surface elevation directly seaward of the mouth at high discharges may be significant.

We detail in this Chapter experiments performed simulating a sloped river discharging at a constant flowrate into a quiescent salty basin. In Section 4.2 we give a brief review of the hydraulic theory as it applies to the salt wedge, as well as theoretical background pertaining to the plume spreading rate and liftoff. We describe the experimental apparatus

and our processing methods in Section 4.3. In Section 4.4 we detail our observations of the salt wedge length, as well as the plume spreading profile and liftoff point. We discuss and summarize our results in Section 4.5.

4.2 Theoretical Background

The theoretical description of the salt wedge is given in Chapter 2. Briefly, we review the derivation and results here. Figure 4.1 shows the salt wedge model geometry and the independent and dependent model variables; it is reproduced from Figure 2.2 in Chapter 2 for convenience. The flow is modeled as two distinct immiscible layers, each of uniform density, interacting only via shear stress at the interface τ_i, parameterized as $\tau_i = C_i \rho u^2$. In this relationship, C_i is a quadratic interfacial drag coefficient, assumed spatially uniform, ρ is the fluid density, and u is the uniform along-channel velocity of the upper layer. We drop the subscript 1 because the salt wedge is assumed arrested so that the lower layer velocity is zero. We apply conservation of mass and momentum to this scenario to find

$$q \equiv \frac{Q}{b} = u h_1 \tag{4.1}$$

$$u\frac{du}{dx} + g\frac{d\eta}{dx} + C_i\frac{u^2}{h_1} = 0 \tag{4.2}$$

$$g\frac{d\eta}{dx} - g'\frac{dh_1}{dx} - C_i\frac{u^2}{h_2} = 0. \tag{4.3}$$

Non-dimensionalization of the continuity and momentum equations reveals that, in the case of a sloping estuary of uniform width, the non-dimensional intrusion length $L_* = C_i L/h_S$ is a function of the freshwater Froude number F_f, the normalized stratification, $\Delta\rho/\rho_2$, and the non-dimensionalized slope-limited maximum intrusion length, C_i/α. Recall also that the dimensioned maximum intrusion length is h_S/α. The influence of $\Delta\rho/\rho_2$ was found to be slight, resulting in a variation in L_* of only a few percent for a factor of 2 change in $\Delta\rho/\rho_2$. Thus, L_* is, to a good approximation, a function of F_f and C_i/α. It was found the the exponent n decreased rapidly with decreasing C_i/α and decreasing F_f.

The theory gives $L_* = 0$ for $F_f = 1$, consistent with two layer hydraulics (Armi & Farmer, 1986; Geyer & Ralston, 2011). For freshwater Froude numbers ≥ 1, the salt wedge is expelled from the channel. In this case, a liftoff front forms, as sketched in Figure 4.2. For a freshwater Froude number of exactly one, the liftoff front will be at the river mouth. In general, liftoff occurs at the point where the plume area decreases to such a value that the internal Froude number $Fr_i = u/\sqrt{g'h_1} = 1$, where u is the mean plume velocity and h_1 is the plume thickness. The initial value of the internal Froude number is equal to F_f when $F_f \geq 1$. When the plume leaves the confines of the river channel, it spreads laterally and vertically, with the vertical spreading set by the slope of the coastal shelf since the plume remains bottom attached. Thus, the location of the liftoff front, and whether or not it can be forced significantly offshore, depends critically on the rate of lateral spreading in the bottom-attached plume. There are several forcing mechanisms that drive this lateral spreading: the buoyancy of the plume, lateral turbulent entrainment of ambient oceanic fluid, and the resistance to spreading offered by the shelf. The rate of lateral spreading and the location of the liftoff front depends critically on the interplay of these mechanisms as it determines the rate of bottom attached spreading. However, there has been little work examining the spreading dynamics of the plume during high flow events, for which $F_f > 1$ to $O(10)$.

For subcritical outflows ($F_f < 1$), the lateral spreading has been observed to be driven by the buoyancy of the plume and to equal the interfacial longwave speed, $c = \sqrt{g'h_1}$, which is also the velocity of a buoyant gravity current in an infinitely deep ambient fluid (e.g. Hetland, 2010; Yuan & Horner-Devine, 2013). In this case, the spreading angle of the plume is given by twice the ratio of the lateral spreading velocity c to the mean offshore plume velocity, u. Recognizing that $Fr_i \equiv u/c$, this gives

$$\left(\frac{db}{dx}\right)_{buoyant} = \frac{2}{Fr_i}. \tag{4.4}$$

This equation, when combined with the anticipated evolution of the Froude number for subcritical and supercritical outflows, gives characteristic spreading profiles for buoyantly-

spreading plumes. This is illustrated in Figure 4.3. The subcritical plume is forced by the hydraulic transition at the river mouth to become supercritical, resulting in an initial increase in the internal Froude number and convergence of the plume width profile in accordance with Equation 4.4. The Froude number reaches a peak, after which point the vertical entrainment of low momentum fluid causes a decrease in Fr_i and a diffuse transition to $Fr_i < 1$. The decrease in Froude number results in divergence of the plume. Accordingly, there is anticipated to be a transition in the curvature of subcritical plumes (from negative to positive, convergent to divergent) that indicates the location of the peak Froude number.

Supercritical plumes start at a large value of the internal Froude number, $Fr_i(x = 0) = F_f$, the Froude number decreases as the plume expands laterally and vertically. This results in divergence of the plume width profile. When the area is reduced enough that $Fr_i = 1$, liftoff occurs and the Froude number increases and then decreases in a manner analogous to the subcritical plume. In this case, there are anticipated to be two transitions in the curvature of the width profile, a transition from convergence to divergence associated with the location of the peak internal Froude number, and an earlier transition from divergence to convergence associated with plume liftoff.

The description of the plume spreading based on the assumption of buoyantly driven spreading becomes less accurate as the Froude number increases. Eventually, F_f becomes large enough that the momentum of the plume dominates over the buoyancy forcing and the turbulence generated at the lateral margins of the bottom attached plume cause the entrainment of ambient fluid. In this case, the spreading is like a wall bounded planar jet and is anticipated to be narrow and constant, $(db/dx)_{jet} = S_{jet}$. This transition from plume-like to jet-like behavior results in a plume area that does not increase as rapidly offshore and is anticipated to force the liftoff further offshore. These experiments will investigate the transition from plume-like to jet-like plume behavior, as well as the relationship between the spreading profile and the plume liftoff front.

4.3 Experimental Methodology

The experimental setup is sketched in Figure 4.4. The top panel shows the plan view, and the bottom panel shows the side view. Freshwater is pumped from the source tank F to a filling basin A at the upstream end of the experimental channel. The flowrate into A is controlled by a pump and flowmeter. After an initial filling period, the discharge from A matches that into the channel. The channel is 10 m long, 10 cm wide, and 20 cm tall. The flow into the channel undergoes a very short initial supercritical adjustment period, approximately 10 cm long. The flow in the channel feeds at its downstream end into a large basin, filled with salty water, that is 2.5 m wide, 4 m long, and 0.5 m tall, forming a buoyant plume. The freshwater flow passes initially over a reflective shelf D that is suspended in the receiving basin. The shelf is sloped with a mean slope of $\alpha_{shelf} = 0.05$ to simulate inflow onto the coastal shelf. An overflow weir E at the far end of the receiving basin is adjusted initially to match the set water height in the basin. The overflow weir collects the buoyant freshwater during the run and this water is pumped by three drainage ports to a discharge sump. The channel elevation at the upstream end can be adjusted in 0.5 cm increments allowing us to set the river slope α. Aluminum track running over the channel and plume C support a motorized cart B that carries a sonic altimeter H, used to measure the water surface elevation, and a camcorder G, which takes video of the flow in the channel during the salt wedge runs, when it is illuminated from underneath by uniform intensity LED panels. These videos are used in the optical thickness method (OTM) as applied to the salt wedge, detailed below. During runs where we want to image the plume, the flow is illuminated by an external light source J. This light passes through the plume, is reflected by the shelf, and recorded by a Point Grey Grasshopper camera I that is suspended above the receiving basin. These images are used in the OTM analysis of the plume spreading and thickness.

Our experimental independent variables are the river discharge Q, the channel bottom slope α, the density of the salt water, which we adjust to set the normalized stratification $\Delta\rho/\rho_2$, and the height in the salty receiving basin, which is the imposed shoreline depth

h_S. We measure the free surface elevation $\eta(x)$ using the sonic altimeter, the elevation of the density interface in the salt wedge and plume $h_i(x)$ and the width profile of the plume $b(x)$ using OTM, and the location of the liftoff front visually by illuminating the flow in the receiving basin from the side using a uniform intensity LED panel like those placed under the channel. Experimental parameters for all of the salt wedge runs are listed in Table 4.1 and for all of the plume runs in Table 4.2.

During salt wedge runs, for which we obtain profiles of the free surface and density interface in the channel, the salt water is dyed with food coloring (see Figure 4.5). Before the run, a video along the channel is taken with the channel filled with undyed freshwater and the LED panels on. A video is also taken during the run. The ratio of the along-channel intensity profiles during the run, $I(x)$, and before the run, $I_0(x)$, is related exponentially to the thickness of the dyed layer:

$$\frac{I}{I_0} = ae^{-bh(x)} + c. \tag{4.5}$$

This is the basis of the optical thickness method (OTM). The coefficients a, b, and c are obtained by taking the ratio of intensity images of a cuvette that is filled with dyed and undyed water. The uniform variation of fluid depth in the cuvette allows us to construct a curve of the intensity ratio versus the dyed layer thickness, and this curve is described effectively by an exponential fit of the form of Equation 4.5. This method is detailed in Yuan *et al.* (2011); Yuan & Horner-Devine (2013). It is important to note that OTM will give an equivalent dyed layer thickness. This coincides with the real layer thickness only if there is no mixing. While this is obviously not the case here, the mixing in this highly stratified and low energy system is quite small, and the behavior of the equivalent layer thickness is sufficient to characterize the structure of the two-layered system. The measured interfacial elevation is used to quantify the effects of the channel bottom slope on the intrusion length and to compare our theoretical predictions for the length and structure of the salt wedge to the data.

Figure 4.5 shows a profile of the salt wedge obtained during a run (the orange layer). It is apparent in this Figure that there is very little mixing between salt and freshwater and

the two layers remain very distinct, in agreement with our analytical assumptions. Also apparent are wispy instabilities along the length of the interface. These instabilities have the characteristic structure of Holmboe instabilities (e.g., Hogg & Ivey, 2003); tendril-like wisps extending upward from the lower layer to the upper layer were observed to extend from the cusps of elongated interfacial waves. Holmboe instabilities are associated with the generation of turbulence, indicating that the flow is not laminar.

During the plume runs, the freshwater is dyed (see Figure 4.6). When applying the OTM, it is necessary to dye the thinner fluid layer to get meaningful results; this is the freshwater plume seaward of the mouth and the salt wedge landward of the mouth. Before the run, we take video of the reflective shelf in the basin while it is filled with undyed water. We take video during the run as well. The plume steady state is identified visually and the ratio of the light intensity fields during the run and before the run are averaged over the plume steady state. The plume thickness is obtained using Equation 4.5 and a calibration obtained using the procedure described above for the salt wedge runs. The lateral profile of the plume thickness is observed to be Gaussian in shape, as was observed in previous experiments described by Yuan & Horner-Devine (2013) using a similar setup. The profile of the standard deviation of a Gaussian fit to the lateral thickness profile $\sigma(x)$ gives a metric of the plume width. Here we use a coefficient of proportionality of 2 between the plume width and the standard deviation, $=2\sigma$ because this was observed to effectively characterize the location of the lateral front between fresh and ambient salty water. Yuan & Horner-Devine (2013) used a coefficient of proportionality of 4 based on considerations of freshwater flux conservation; however, this was found to overestimate the width of the plume significantly here.

Liftoff was observed visually for several of the runs. During these runs, the plume was illuminated from the side by an LED panel. Markings at every centimeter along the side of the tank allowed us to measure the location of the liftoff front. Images from one such run are shown in Figure 4.6. One feature apparent in this Figure that is typical of all of the observed liftoff fronts is a separation between the location of the hydraulic liftoff, apparent

from the curvature of the interface, and the upstream-most extent of salt water penetration beneath the plume. Hydraulic theory predicts that salt water cannot extend underneath the plume landward of the liftoff front; however, this was not the case here, possibly owing to the highly energetic jet-like nature of the discharges causing partial flow separation from the shelf. This zone extends 4 to 5 cm here; however, it was observed to extend as much as 10 to 15 cm in other runs. Our ability to consistently locate the liftoff front was also hindered by a low period oscillation observed in the location of the front, with an amplitude on the order of 5 cm, and lateral variation in the liftoff location, apparent when comparing images from a camera that had been focused on the plume centerline (like Figure 4.6) to those from a camera that had not. This uncertainty makes the visual estimates unreliable and leads us to infer the location of the liftoff front indirectly from the shape of the plume width profile.

We have not included any analysis of the free surface profiles in this Chapter. It was found that uncertainty in the profiles due to the imperfect matching of joining sections of track and a global setup in the receiving basin set by the hydraulics of the overflow into the drainage weir together resulted in uncertainty in the measurement that was significantly larger than any apparent signal of discharge-dependent superelevation in the vicinity of the river mouth.

4.4 Results

4.4.1 Salt Wedge Intrusion Length

Here we present our results for the dependence of the intrusion length on the freshwater Froude number and bottom slope, and a comparison of our experimental results to the theoretical predictions presented in Poggioli & Horner-Devine (2015). The optical thickness method was used to measure the salt wedge profile for four different channel slopes and for six to eight discharges for each slope, in the range of 25 to 135 liters/minute. From these profiles the intrusion length was inferred from the point where the equivalent salt water thickness went to zero. The bottom slope was varied by more than an order of magnitude, between

$\alpha = 1.1(10^{-3})$ and $13.6(10^{-3})$, in order to robustly test the dependence of the salt wedge intrusion length on the channel bottom slope. For each run, the shoreline depth was $h_S = 15$ cm, the normalized stratification was $\Delta\rho/\rho_2 = 0.01$, and the freshwater Froude number was varied only by varying the discharge. Figures 4.7a and c show the measured interface profiles as a function of the upstream distance ($= -x$ in our coordinate system) for $\alpha = 1.1(10^{-3})$ and $13.6(10^{-3})$ and four different freshwater Froude numbers each. Three of the four profiles are at the same value of F_f for both bottom slopes ($F_f = 0.62$, 0.48, and 0.35) allowing a direct comparison and assessment of the effect of bottom slope on the intrusion. We observe that the larger bottom slope reduces the intrusion length by an amount that becomes larger as the intrusion length increases (i.e., as F_f decreases), and that the sensitivity of the salt wedge length to F_f is therefore correspondingly decreased with increasing bottom slope.

Figures 4.7b and d show the salt wedge thickness h_2 normalized by the initial thickness at the mouth $h_{20} = h_S(1 - F_f^{2/3})$, predicted based on the imposed shoreline depth and freshwater Froude number, versus the upstream distance $-x$ normalized by the measured intrusion length L. Because the channel intrudes into the plume basin approximately 11.5 cm and we cannot illuminate the flow in this region, we are unable to measure the initial thickness. We compare this to the normalized profile predicted by the hydraulic theory for $F_f = 0.35$. The normalized profile is a function of the freshwater Froude number; however, the variation of the normalized curves with F_f is dwarfed by the full vertical variation in the normalized profile, as well as by the noise in the experimentally measured curves. We therefore plot only for the intermediate value of F_f. For the lower slope, the model does very well for roughly the last half of the intrusion, but the profiles deviate seaward of this point. There is considerable spread and noise in the profiles for the larger slope, with the highest F_f run falling above the theoretical curve and the lower F_f runs falling below the curve. These runs are sorted by F_f in a manner consistent with the theory; however, the difference between the profiles at different values of F_f is much more pronounced than in the theoretical results. The deviation appears to be spatially dependent; when looking at the comparison for $\alpha = 1.1(10^{-3})$ (Figure 4.7b), the $F_f = 0.62$ and (especially) the $F_f = 0.48$ curves appear

to deviate from the theoretical profile closer to the toe (in the normalized plot) than the higher F_f profiles; the former are confined to a region within 3 m from the channel mouth. Additionally, the plots presented in Figure 4.7d for $\alpha = 13.6(10^{-3})$ all deviate from the theoretical curve except very near the toe; each of these curves is ≤ 3 m long. This suggests the possibility that the measurement becomes less reliable closer to the mouth, or at least for shorter intrusions, though the reason for this is unclear. An alternative possibility would be mixing or a buildup of freshwater in the vicinity of the mouth resulting in a reduced $\Delta\rho/\rho_2$; however, this would result in deviation in the opposite direction and is not consistent with the convergence of the measured curves and theoretical curve that is apparent especially in Figure 4.7b. It is uncertain what causes this deviation; however, it does not appear to be related to a change in $\Delta\rho/\rho_2$; if it did, this would quantitatively, though not qualitatively, modify our results.

In Figure 4.8 we plot the measured values of the intrusion length normalized by the shoreline depth versus the freshwater Froude number for all four slopes. In the upper panel, the plot is presented on linear axes, and the sort of the curves with bottom slope, and the dramatic reduction of the sensitivity of the intrusion length to discharge with increasing α is readily apparent. Though the curves appear to collapse for $F_f \geq\sim 0.7$, below this, they diverge rapidly, with the lowest slope runs showing a much greater sensitivity of the intrusion length to F_f, and a much larger maximum intrusion, than any of the other slopes. The lower panel plots these same profiles on logarithmic axes to allow us to quantify the magnitude of the dependence of L on F_f using an exponent n in a locally-valid power law of the form $(L/h_S) \sim F_f^{-n}$. This exponent is equivalent to the negative of the slope of the curve in logarithmic space and is how the scaling of the estuary length with discharge is quantified in the literature. For the smallest and largest bottom slopes considered, we show linear fits (in logarithmic space) to successive groups of three points and the associated exponent n. We show this for freshwater Froude numbers in the range $0.4 < F_f < 0.55$ for both slopes and for the last three points at $\alpha = 13.6(10^{-3})$. In the former case, the increase in the slope by a factor of approximately 12 results in a reduction of the exponent from 2.75 to

1.86. This confirms that, for a given value of the freshwater Froude number, the value of n decreases with increasing bottom slope. Examining the curves in Figure 4.8, we see that they diverge even more as the freshwater Froude number becomes smaller, indicating this effect, the reduction of n with increasing α, becomes more pronounced at lower freshwater Froude numbers. This potentially accounts for the deviation of n in real salt wedge estuaries from the theory of Schijf & Schönfeld (1953). Typical freshwater Froude numbers are on the order of 0.01 to 0.1 in the field (Poggioli & Horner-Devine, 2015). Based on the above observed trend, we would expect n to deviate significantly from Schijf & Schönfeld (1953) for values of F_f this small, likely even at the small bottom slopes encountered in estuaries, typically in the range of $10^{-5} < \alpha < 10^{-3}$. The potential for reduction of n to values typical of real estuaries under the influence of bottom slope is supported by the observation that the last three points in the curve corresponding to $\alpha = 13.6(10^{-3})$ have a mean slope of $n = 0.7$, close to the upper limit of $n = 0.6$ observed in a numerical model of the Merrimack River estuary (Ralston *et al.*, 2010).

Looking back again at the curves in Figure 4.8, we can estimate an upper limit on the intrusion length where the three highest slope curves deviate from flat-bottom behavior by estimating where they deviate from the shallowest-slope curve; this value appears to decrease with increasing bottom slope, as we would expect, and is smaller than $L/h_S = 10$, or $L = 1.5$ m for each of the three slopes. We can compare this to the slope-limited maximum intrusion length $L_0 = h_S/\alpha$ for each of these three slopes: $L_0 = 26$, 16, and 11 m. Thus, the critical intrusion length at which the behavior of L with F_f begins to deviate from the flat estuary behavior described by Schijf & Schönfeld (1953) is on the order of 10% or less of the maximum intrusion length. For a river like the Mississippi, with a bottom slope on the order of 10^{-5}, this gives a critical intrusion length on the order of 100 km; for reference, intrusion lengths in the Mississippi can reach 400 or more km upstream of Head of Passes (Rattray & Mitsuda, 1974). For a river like the Duwamish in Seattle, USA, with a bottom slope on the order of 10^{-3}, this gives a critical intrusion length of only a few meters. Thus, it is likely that the influence of bottom slope is a key contributor to the decreased sensitivity of the intrusion

length to river discharge that is consistently measured in the field.

The solution presented in Poggioli & Horner-Devine (2015) produces curves that are qualitatively similar to those observed. However, agreement cannot be obtained between the experiments and theory if C_i is assumed constant. While a constant value of approximately $C_i = 4(10^{-4})$ appropriate to the field has been obtained via analytical, numerical, and observational methods (Karelse *et al.*, 1974; Sorgard *et al.*, 1990; Sorgard, 1991; MacDonald & Geyer, 2004; Poggioli & Horner-Devine, 2015), it has been repeatedly observed that, at laboratory scales, C_i is a decreasing function of the upper layer Reynolds number $Re \equiv uh_1/\nu = q/\nu$, where $\nu = 10^{-6}$ m^2/s is the kinematic viscosity of water. Laboratory flows are typically at values of Re in the range $10^2 < Re < 10^4$, whereas environmental flows are typically in the range of $10^5 < Re < 10^7$ (Karelse *et al.*, 1974). We test whether the solution presented in Poggioli & Horner-Devine (2015) accurately represents the model data by calculating the interfacial drag coefficient from the observed intrusion length and assessing if the values so obtained, when plotted against Re, collapse to a form that is consistent with previous observations of C_i in the lab. Figure 4.9 presents our results for C_i versus Re, along with an exponential fit indicating $C_i \sim Re^{-1.3}$ ($R^2 = 0.82$), and Figure 4.10 plots this data along with previous laboratory and field estimations, and a laminar solution derived by Ippen & Harleman (1952), all compiled in the extensive review by Karelse *et al.* (1974, Figure 2.3). The C_i values do indeed collapse when plotted against Re, and our data shows a high degree of overlap with that collected by Averkiev & Kind (1965) and Hendrikse (1965). Our inferred values of C_i depend on $Re^{-1.3}$, a somewhat steeper slope than the theoretical predictions of Ippen & Harleman (1952) based on laminar theory ($C_i \sim Re^{-1}$). Additionally, the slope of our data is visibly steeper than that of the data collected by Averkiev & Kind (1965) and Hendrikse (1965) (see Figure 4.10). However, our data are clearly consistent with previous observations, and more generally with the observation that C_i is a strong function of Re in this range of Reynolds numbers; furthermore, our values for C_i collapse and do not show any significant trends with the bottom slope, and a single fit to all of the C_i data, combined with the theory presented in Poggioli & Horner-Devine (2015) provide good agreement with

the observed L versus F_f curves.

In examining Figure 4.10, it is interesting to note that there appear to be two distinct branches of the C_i versus Re curve at values of $Re < 10^5$–that based on the extensive data compiled by Riddell (1970) and roughly corresponding with the theoretical predictions of Ippen & Harleman (1952), and another based on the data of Averkiev & Kind (1965); Hendrikse (1965); Zanotti (1965); and the present study. Perhaps this is to do with a transition from laminar to transitionally turbulent flow at a Reynolds number that is dependent on ambient disturbances to the flow, but this hypothesis is impossible to address without more detailed knowledge of the experimental apparatus of each of the above mentioned studies. Interestingly, while Hendrikse (1965); Zanotti (1965); and Riddell (1970) infer their values for C_i from the shape of the salt wedge interface, as we do here, Averkiev & Kind (1965) infer theirs from turbulent velocity correlations obtained via photographic measurements of the velocity field. As a final point, we note that, though it is sometimes asserted that experiments of this type conducted at $Re \leq 10^4$ are essentially laminar (e.g. Sorgard, 1991), our observations of the turbulent deformation of the saltwater-freshwater interface indicate that this is not the case in the present study; our flow was at least transitionally turbulent.

Figure 4.11 shows theoretical curves based on the solution presented in Poggioli & Horner-Devine (2015) and our slope-independent fit of the C_i versus Re curve. Allowing for C_i to vary in this manner gives good fits of the experimental data to the theory; the theoretical predictions are consistent with the sorting of the data based on the bottom slope. We stress that, though we are using a fit of C_i with Re inferred from our model in our model fits, 1) the calculated C_i values were observed to collapse and showed no clear relationship with bottom slope, confirming that the present theory accurately characterizes the dependence on α, and 2) C_i has been consistently observed to vary strongly with Re in the range of Reynolds numbers considered in the present experiments. Bottom slope has a significant effect on the magnitude of the intrusion length, and on its sensitivity to the river discharge, an effect that is felt for intrusion lengths as small as 1/10 of the slope-limited value, and which may account for the deviation of field observations from theory developed for flat

estuaries (Schijf & Schönfeld, 1953; Ward, 1976; Ralston *et al.*, 2010; McKeon *et al.*, 2014; Poggioli & Horner-Devine, 2015). The influence of bottom slope is successfully characterized by the solution presented in Poggioli & Horner-Devine (2015) when it is recognized that C_i varies significantly with Re for $Re <\sim 10^5$.

4.4.2 Plume Spreading and Liftoff

Figures 4.12 and 4.13 show the plume width profiles obtained for runs with $h_S = 6$ and 4 cm, respectively, and 5 (Figure 4.12) or 10 (Figure 4.13) different values of the freshwater Froude number, F_f, all supercritical; recall that, for a supercritical freshwater Froude number, the inflow internal Froude number $F_i(x = 0) = F_f$. The widths and offshore distances are normalized by the channel width, b_0. These shoreline depths correspond to inflow aspect ratios of $R_A \equiv b_0/h_S = 1.67$ and 2.5. Generally, in both cases, the width profiles sort with F_f, becoming narrower as F_f increases. In Figure 4.12, the lowest F_f run, $F_f = 1.6$, is convergent over nearly the entire length of the field of view, consistent with liftoff at the mouth and a supercritical plume with an internal Froude number that increases in the offshore direction. For each of the runs with larger values of F_f, however, there is a distinct region of divergence and then a transition to convergence. The location of these curvature transitions, $L_{curvature}$, were assessed visually for each run and are indicated in Figures 4.12 and 4.13 by black points along each curve for which $L_{curvature} > 0$. This transition is consistent with the dynamic transition from decreasing to increasing Fr_i at the liftoff front (see Figure 4.3) and moves offshore with increasing F_f, also consistent with liftoff dynamics.

In the case of the $F_f = 2.4$ run with $R_A = 1.67$ (Figure 4.12) and the $F_f = 3.0$ run with $R_A = 2.5$ (Figure 4.13, the initial divergence is great enough that the convergent portion of the plume inherits an initial width that is greater than the width obtained by the plume that is convergent from the mouth. That is, comparing the $F_f = 1.6$ and $F_f = 2.4$ curves in Figure 4.12, and the $F_f = 1.6$ and 3.0 curves in Figure 4.13, we see that the higher Froude number curve crosses the lower Froude number curve during its period of initial divergence near the mouth. This suggests that an initially divergent, bottom attached region can sometimes

result in a near-field plume that is wider than a subcritical plume, or a plume for which liftoff is very neart (within 1 to 2 channel widths, based on Figures 4.12 and 4.13) the mouth.

Apparent in both Figures is the existence of three distinct types of plume width profile. For $F_f = 1.6$ ($R_A = 1.67$, 2.5, both Figures), the plume is convergent from the mouth seaward. This is consistent with liftoff at the mouth, forcing the plume to shoal and accelerate, and Fr_i to increase. Eventually, we anticipate that these plumes will become divergent as the peak Fr_i is reached (see Figure 4.3), and entrainment begins to overcome the effect of shoaling (Hetland, 2010). This is observed in Figure 4.12, but not Figure 4.13. This is not an aspect ratio effect, but is instead consistent with the fact that the initial area available for entrainment to the plume, $(A_{entrainment})_0 \sim (b_0 + h_S)\Delta x$, where Δx is a small length from the river mouth, is larger in the first set of runs, for which $h_S = 6$ cm, than in the second set of runs, for which $h_S = 4$ cm. For a given F_f and b_0, there is more area available to entrain water and slow down the plume in the set of runs with the larger shoreline depth. This potentially explains why the $F_f = 1.6$ run transitions to divergence when $h_S = 6$ cm but not when $h_S = 4$ cm (Figures 4.12 and 4.13, respectively).

As F_f is increased, the plume is no longer initially convergent, and we enter the transitional regime. These profiles are characterized by initial divergence, within 2 to 4 channel widths of the mouth, and a transition to convergence beyond that. The transitional runs for $R_A = 2.5$ are shown in Figure 4.14. We see that, for the runs with the highest two values of F_f (4.0, 4.5), the curves, and $L_{curvature}$ do not sort with F_f. We will see below, Figure 4.15, that this is consistent with a rapid transition in plume behavior around a critical value of F_f that is sensitive to experimental conditions.

This rapid transition in plume behavior is apparent in Figure 4.12, and the final, jet-like regime characteristic of values of F_f above some critical value, is seen clearly in the five highest F_f profiles shown in Figure 4.13. The jet regime is characterized by a nearly linear initial spreading rate S_{jet} that persists far offshore, resulting in profiles that collapse over much of their length. This is not an artifact of the length of the field of view; there is a value (or narrow band of values) of F_f that can be associated with the transition. To see

this, note that the runs shown in Figure 4.12 are evenly spaced in F_f space; however, the transition from transitional to jet-like behavior is not. There is clearly a rapid change in plume behavior at a value of F_f between 3.2 an 4.1. The same observation holds in Figure 4.13. In this case, the transitional value of F_f is between 4.0 and 5.0.

We can see this even more clearly by plotting $L_{curvature}/b_0$ versus F_f, Figure 4.15. In this Figure, we see a clear step-like jump in the location of the liftoff front, as indicated by $L_{curvature}$, near a critical value of F_f that falls between 4 and 4.5. The overlap of the two regions is a byproduct of the failure of the highest two F_f runs to sort in Figure 4.14. This corresponds to a pronounced difference in the spreading profile and may indicate that the processes governing the critical value of F_f is sensitive to experimental conditions. The structure of this plot for the runs with $R_A = 1.67$ is qualitatively similar, again showing evidence of a critical F_f, but is not shown here because there are only four nonzero values of $L_{curvature}$.

A possible candidate for the critical F_f is the value for which the initial buoyant spreading rate $(db/dx)^0_{buoyant} = 2/F_f$ is equal to the jet spreading rate S_{jet}. This would give $(F_f)_{trans} = 2/S_{jet}$; based on observed values of S_{jet} for $R_A = 1.67$ and 2.5, this gives $(F_f)_{trans} = 2.4$ and 6.1. This is below the transition region for the $R_A = 1.67$ runs and above the transition region for the $R_A = 2.5$ runs. Additionally, even if the initial buoyant spreading rate falls within the "entrainment envelope"–i.e., $2/F_f \leq S_{jet}$, the plume should still rapidly diverge from this jet-like profile. This persistant jet-like structure offshore, and the associated reduction in buoyant spreading that keeps the runs above the critical value of F_f from diverging rapidly from S_{jet}, must be associated with a rapid increase in the entrainment of the ambient fluid through the lateral margins of the bottom attached plume. The critical F_f, $(F_f)_{trans}$, must be the value where the outflow is energetic enough to sustain enough turbulent entrainment at the lateral margins that the buoyancy spreading is reduced and the jet spreading is dominant. This value must increase significantly as the aspect ratio increases because an increasing aspect ratio indicates there is more fluid in the bulk of the plume that must be diluted by entrainment through the lateral margins, and this must take correspondingly

more energetic mixing, associated with a higher value of F_f. This agrees with the observed dependence of $(F_f)_{trans}$ on R_A and suggests that the value of $(F_f)_{trans}$ may be a strongly increasing function of the aspect ratio.

Finally, we observe the dependence of S_{jet} on aspect ratio in Figure 4.16. We plot the last two runs from Figure 4.12 and the last five runs from Figure 4.13. We fit a straight line to each set of runs, sorted by R_A, over the first 2 channel widths. The Figure indicates that there is a factor of 2.5 reduction in the jet spreading rate spreading rate as R_A goes from 1.7 to 2.5, a 50% increase. This suggests a strong, nonlinear dependence of S_{jet} on the inflow aspect ratio.

4.5 Discussion

In these experiments, we have successfully measured intrusion length L in a sloped channel for several values of the bottom slope α, varying over an order of magnitude. These results have 1) demonstrated that the sensitivity of the intrusion length to the river discharge Q, characterized by an exponent n in a power law of the form $L \sim Q^{-n}$, is highly reduced by nonzero bottom slope. Furthermore, this reduction of n was observed to occur for intrusion lengths as small as 1/10 of the slope-limited maximum intrusion, $L_0 = h_S/\alpha$. We obtained values of n approaching those observed in the field (0.7 here versus 0.6 in Ralston *et al.* (2010) and 2 to 2.5 in the flat estuary theory (Schijf & Schönfeld, 1953)), and our results are consistent with the theoretical predictions of Poggioli & Horner-Devine (2015) when the interfacial drag coefficient is allowed to vary with Re. This is inline with previous observations, which have consistently shown a strong Re dependence for C_i in the range of Reynolds numbers covered here, and our data falls within the range of previous measurements (Karelse *et al.*, 1974). Our results here, combined with those discussed in Poggioli & Horner-Devine (2015) give compelling evidence that the reduction of sensitivity of the intrusion length to discharge in salt wedge estuaries compared to flat estuary theory and experiments is caused by non-zero channel bottom slope.

Our spreading rate experiments have corroborated our picture of the evolution of the

plume spreading structure with increasing values of the freshwater Froude number F_f. For runs where liftoff is observed to be at the mouth ($F_f = 1.6$ in the present experiments), the plume is convergent starting at the mouth, eventually transitioning to divergence. This is consistent with a plume that is initially critical and has an increasing internal Froude number. It is anticipated that the same profile shape will characterize subcritical runs, which adjust to internal Froude number of 1 at the mouth, but this has not been directly investigated here. Above a critical value of F_f the profiles very nearly collapse to a uniform spreading rate, consistent with entrainment-driven lateral spreading. Intermediate between these extremes, we observed transitional runs which were initially divergent, transitioning within 1 or 2 channel widths of the mouth to convergence. These plumes evolve in a manner consistent with buoyancy-driven spreading, and the length scale associated with the transition in curvature provides an indication of the liftoff location. Both the critical value of F_f for transition to a jet-like outflow, $(F_f)_{trans}$, and the jet spreading rate, S_{jet} were observed to depend significantly on the aspect ratio. In the case of $(F_f)_{trans}$ this dependence on aspect ratio is anticipated to persist for all values of R_A, no matter how large, and to be significant.

Our experimental results provide evidence that the plume may transition to a narrow, bottom-attached jet like outflow at sufficiently large values of F_f. However, the nature of this transition, in particular the value of F_f at which it occurs and the jet spreading rate are highly dependent on the inflow aspect ratio.

However, our quantitative observations of the transition region between plume-like and jet-like spreading, as well as the magnitude of the entrainment-driven spreading rate, are likely to be strongly dependent on the outflow aspect ratio $R_A = b_0/h_S$. Further experiments examining this dependence is necessary; however, experimental simulations cannot hope to achieve aspect ratios characteristic of real systems ($O(100 - 1000)$), and field measurements are unlikely to be conducted when the plume is in a jet-like state because this can occur, if at all, only for extreme flood events, where field observation is not practical. The jet spreading rate is significant when compared to the results reported by Lamb *et al.* (2012), who showed that a spreading rate $S_{jet} \geq\sim 0.05 - 0.1$ is necessary to ensure that there is

not significant buildup of fluid at the river mouth during high discharge. Fluid buildup would modify the drawdown profile in the lower river, resulting in less erosion in the lower river and therefore less export to the shelf and deposition offshore of the mouth. This will have important quantitative effects on predictictions of the morphological evolution of river deltas. The values of S_{jet} observed here are $O(0.1-1)$ and were found to decrease rapidly with increasing aspect ratio, indicating that values on the order of $0.05 - 0.1$ are plausible in the field. However, our results also indicate that the transition to a jet-like outflow depends on the ability of the entrainment at the lateral margins of the bottom attached plume to modify the bulk plume properties in the plume interior. This suggests that $(F_f)_{trans}$ may increase substantially with R_A as the ratio of the volume of the plume bulk interior to the volume of the lateral plume margin increases. In addition to further laboratory work examining the sensitivity of the spreading rate and transition freshwater Froude numbers to aspect ratio, numerical modeling is possibly a way to further extend these observations to values of R_A consistent with the field. This is necessary to determine if jet-like outflows can occur in nature, when they can occur, the quantitative influence of their frequency of occurence on delta evolution, and if they are narrow enough to cause significant fluid buildup at the river mouth, modifying erosional patterns in the lower river and the sediment availability to the shelf and the region just seaward of the river mouth.

Table 4.1: Salt wedge run parameters. $L_0 \equiv h_S/\alpha$ is the slope-limited maximum intrusion length.

Run ID	α	Q (l/min)	$\Delta\rho/\rho_2$	h_S (cm)	F_f	L_0 (m)
SW1	$1.1(10^{-3})$	30, 38, 45, 53, 61, 68, 76	0.01	15	0.28, 0.35, 0.42, 0.48, 0.55, 0.62, 0.69	140
SW2	$5.7(10^{-3})$	32, 45, 53, 57, 68, 76	0.01	15	0.29, 0.42, 0.48, 0.52, 0.62, 0.69	26
SW3	$9(10^{-3})$	23, 38, 45, 53, 61, 64, 76	0.01	15	0.21, 0.35, 0.42, 0.48, 0.55, 0.59, 0.69	17
SW4	$13.6(10^{-3})$	23, 31, 38, 45, 53, 61, 68, 76	0.01	15	0.21, 0.28, 0.35, 0.42, 0.48, 0.55, 0.62, 0.69	11

Table 4.2: Plume run parameters. $R_A \equiv b_0/h_S$ is the inflow aspect ratio. A horizontal line across all columns indicates a change in h_S (and therefore R_A).

Run ID	α	Q (l/min)	$\Delta\rho/\rho_2$	h_S (cm)	F_f	R_A (m)
P1	$1.1(10^{-3})$	23	0.01	4	1.5	2.5
P2	$1.1(10^{-3})$	45	0.01	4	3.0	2.5
P3	$1.1(10^{-3})$	53	0.01	4	3.5	2.5
P4	$1.1(10^{-3})$	61	0.01	4	4.0	2.5
P5	$1.1(10^{-3})$	68	0.01	4	4.5	2.5
P6	$1.1(10^{-3})$	76	0.01	4	5.0	2.5
P7	$1.1(10^{-3})$	83	0.01	4	5.5	2.5
P8	$1.1(10^{-3})$	91	0.01	4	6.0	2.5
P9	$1.1(10^{-3})$	114	0.01	4	7.5	2.5
P10	$1.1(10^{-3})$	136	0.01	4	9.0	2.5
P11	$1.1(10^{-3})$	45	0.01	6	1.6	1.67
P12	$1.1(10^{-3})$	68	0.01	6	2.5	1.67
P13	$1.1(10^{-3})$	91	0.01	6	3.3	1.67
P14	$1.1(10^{-3})$	114	0.01	6	4.1	1.67
P15	$1.1(10^{-3})$	136	0.01	6	4.9	1.67

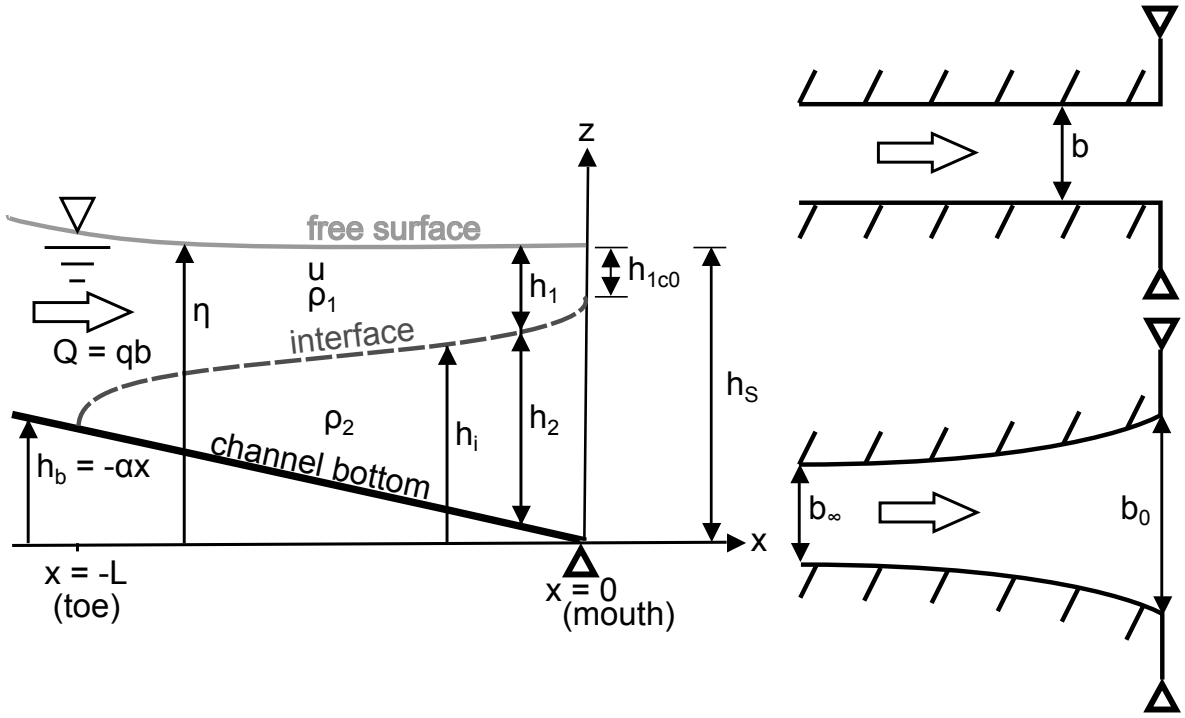

Figure 4.1: The geometry of the salt wedge model and all independent and dependent variables, reproduced from Figure 2.2 in Chapter 2.

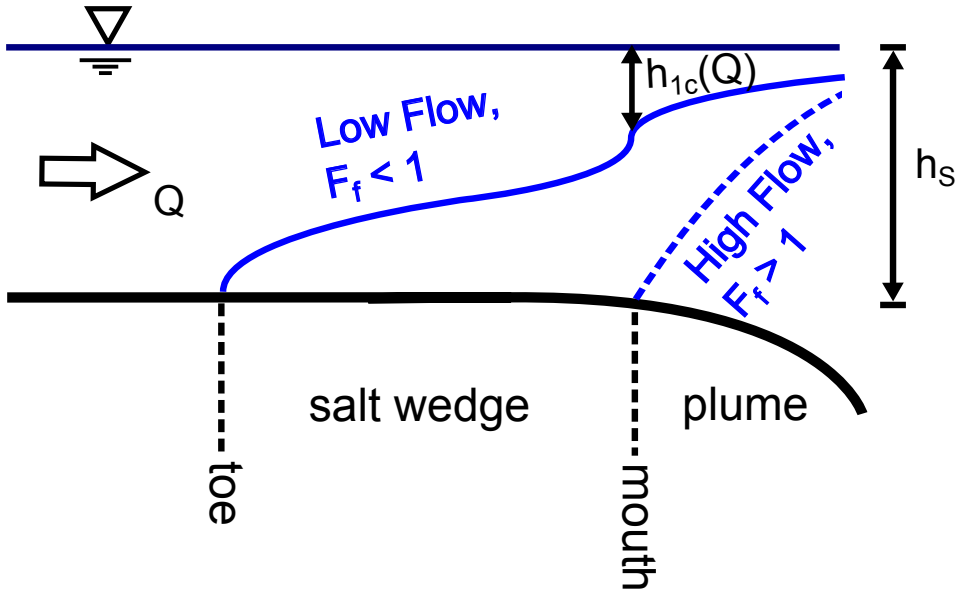

Figure 4.2: A schematic side view representation of the two possible modes of freshwater detachment from the channel bed or shelf: for low flow, $F_f < 1$, a salt wedge intrudes into the river channel. In this case, the intrusion is subcritical and the upper layer thickness at the mouth is forced to the critical upper layer thickness, $h_{1c} = (q^2/g')^{1/3}$. For high flow, $F_f > 1$, a liftoff front is forced at the mouth or, if discharge is high enough, on the coastal shelf.

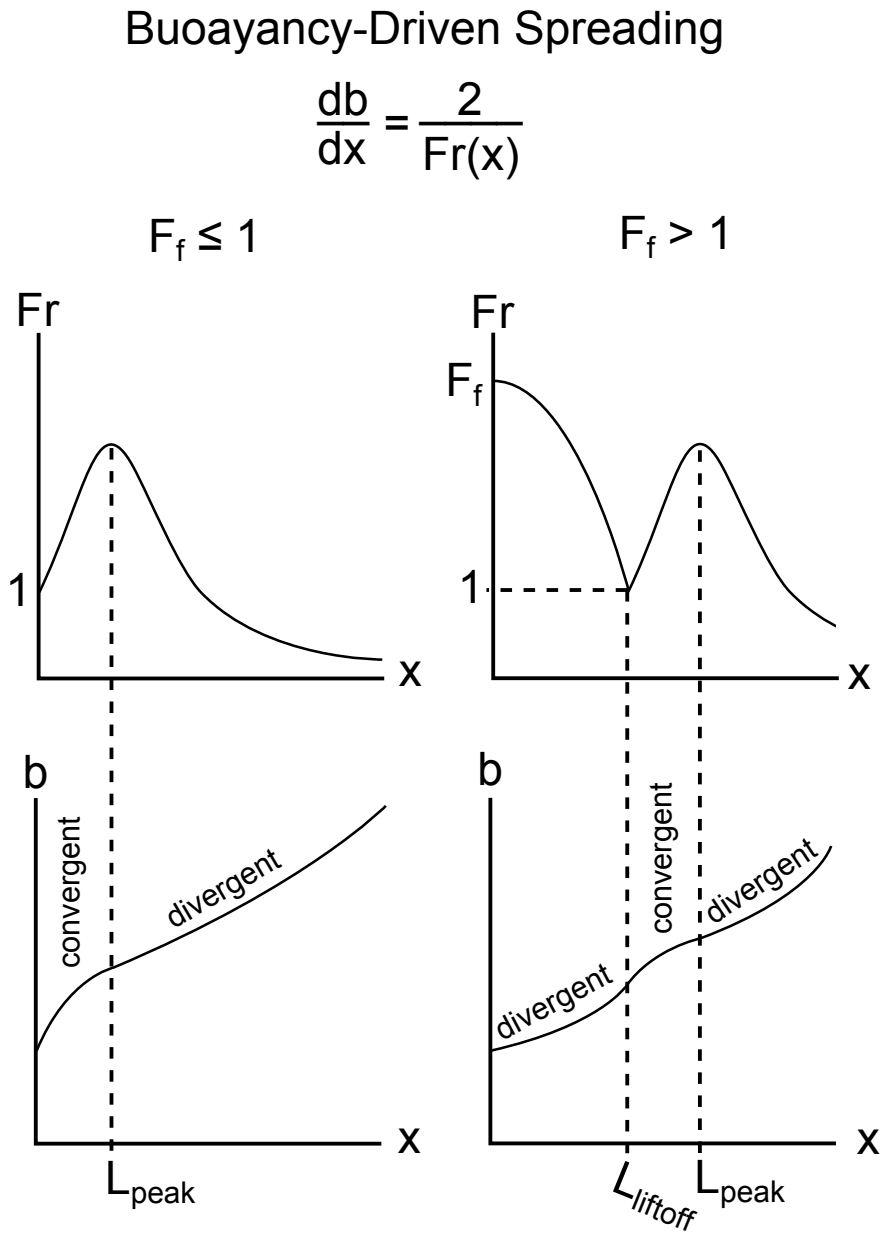

Figure 4.3: A sketch of the anticipated Froude number and plume width profiles anticipated for subcritical ($F_f \leq 1$) and supercritical plumes ($F_f > 1$). The spreading profiles are inferred from the assumption of buoyancy driven spreading, in which the plume expands laterally as a gravity current. This assumption becomes less applicable for higher F_f plumes as bottom friction in the region before liftoff and lateral entrainment begin to dominate the spreading.

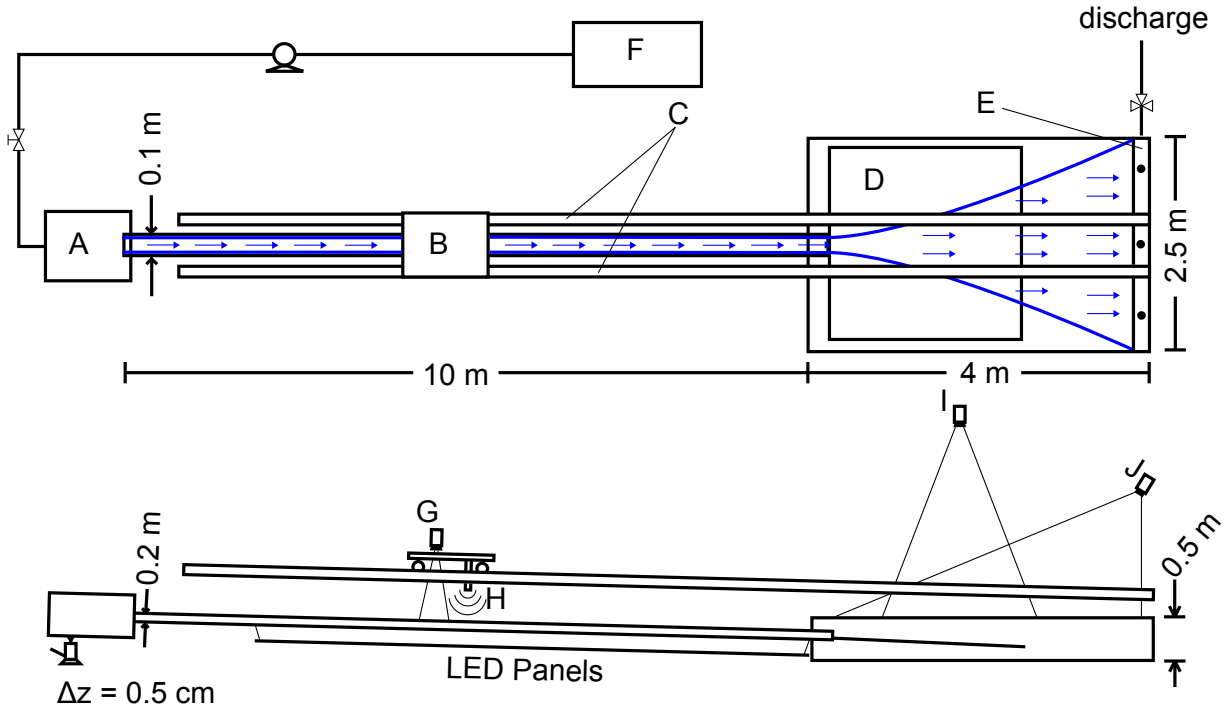

Figure 4.4: A sketch of the experimental setup in plan (top) and side view (bottom). The setup and procedure is described in the text.

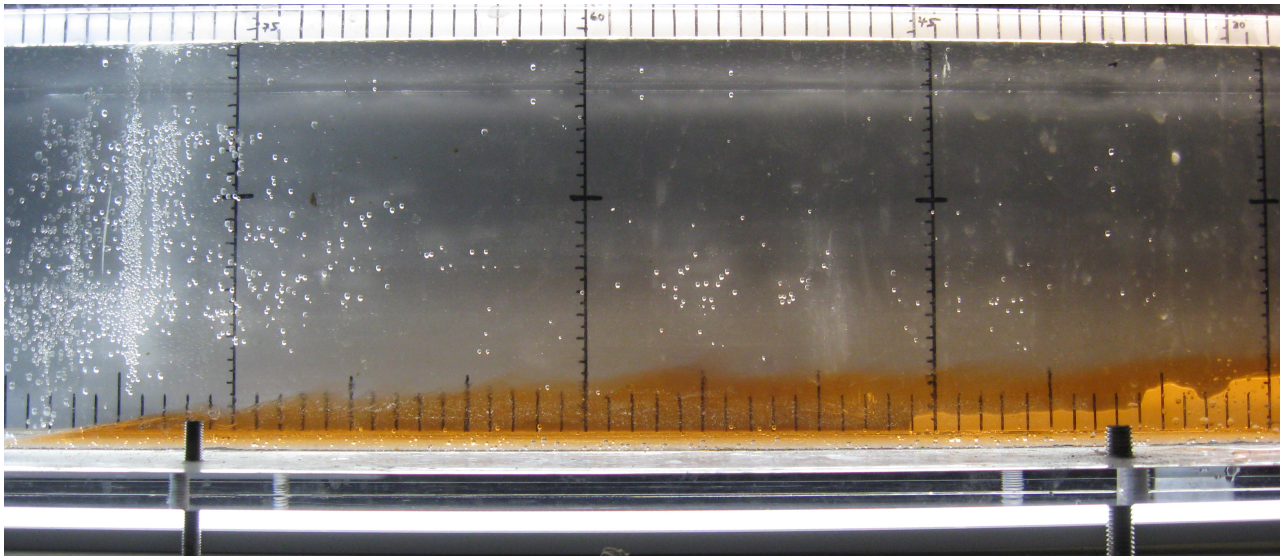

Figure 4.5: Side image of the salt wedge for a flow of 70 liters/minute, a shoreline depth of 15 cm, and a bottom slope of $\alpha = 9(10^{-3})$.

Figure 4.6: Side image of the liftoff front for a flow of 70 liters/minute and a shoreline depth of 4 cm. The labeled along-flow gradings indicate distance from the mouth. Apparent are both the hydraulic liftoff at approximately 22 cm, and the upstream-extent of saltwater penetration underneath the plume, at approximately 18 cm.

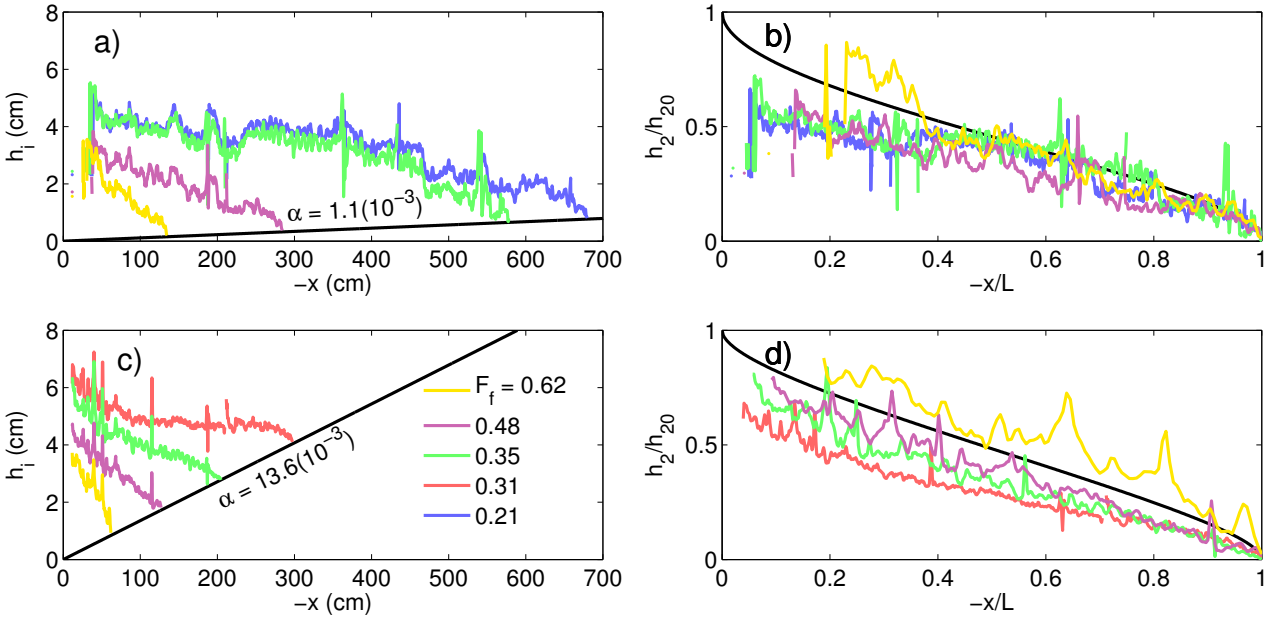

Figure 4.7: a, c) Measured salt wedge profiles for four values of the freshwater Froude number F_f for $\alpha = 1.1(10^{-3})$, panel a), and $\alpha = 13.6(10^{-3})$, panel c). The value of F_f is indicated by the color of the profile. Note that only three of the four values of F_f coincide between panels; the lowest F_f is different for the two slopes. b, d) The salt wedge profiles shown in a) and c) normalized vertically by the predicted initial thickness at the mouth and horizontally by the measured intrusion length. Also shown in panels b) and d) are the normalized profiles predicted from the results of Poggioli & Horner-Devine (2015) for $F_f = 0.35$ (black line) and an Re-dependent value of C_i (see text).

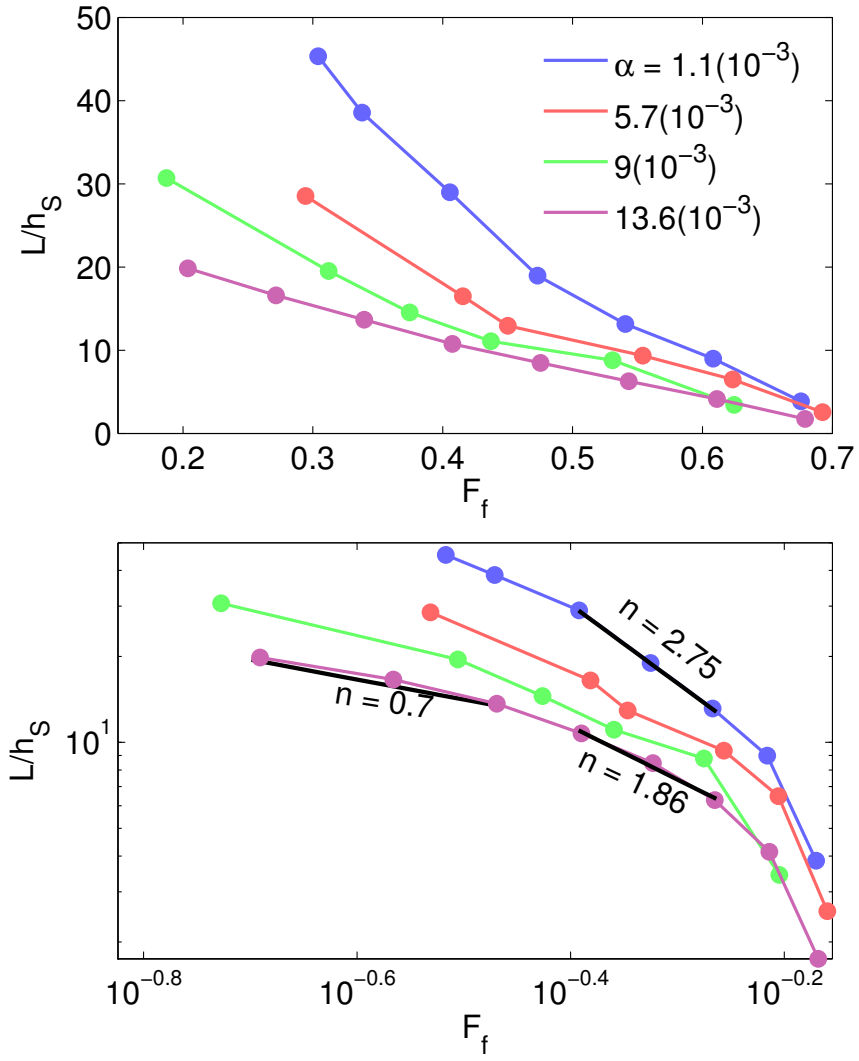

Figure 4.8: (top) The measured variation of intrusion length L, normalized by shoreline depth h_S, with freshwater Froude number F_f for all four of the bottom slopes investigated. (bottom) The same data plotted on logarithmic axes. Also shown in the bottom panel for the shallowest and steepest slopes are linear fits (in log-space) to groups of three points, with the associated exponent $n = -d(log_{10}L)/d(log_{10}F_f)$ in a relationship of the form $(L/h_S) \sim F_f^{-n}$. Fits are shown for the last three points in the highest slope run and three points in the range $0.4 < F_f < 0.55$ for $\alpha = 1.1(10^{-3})$ and $13.6(10^{-3})$.

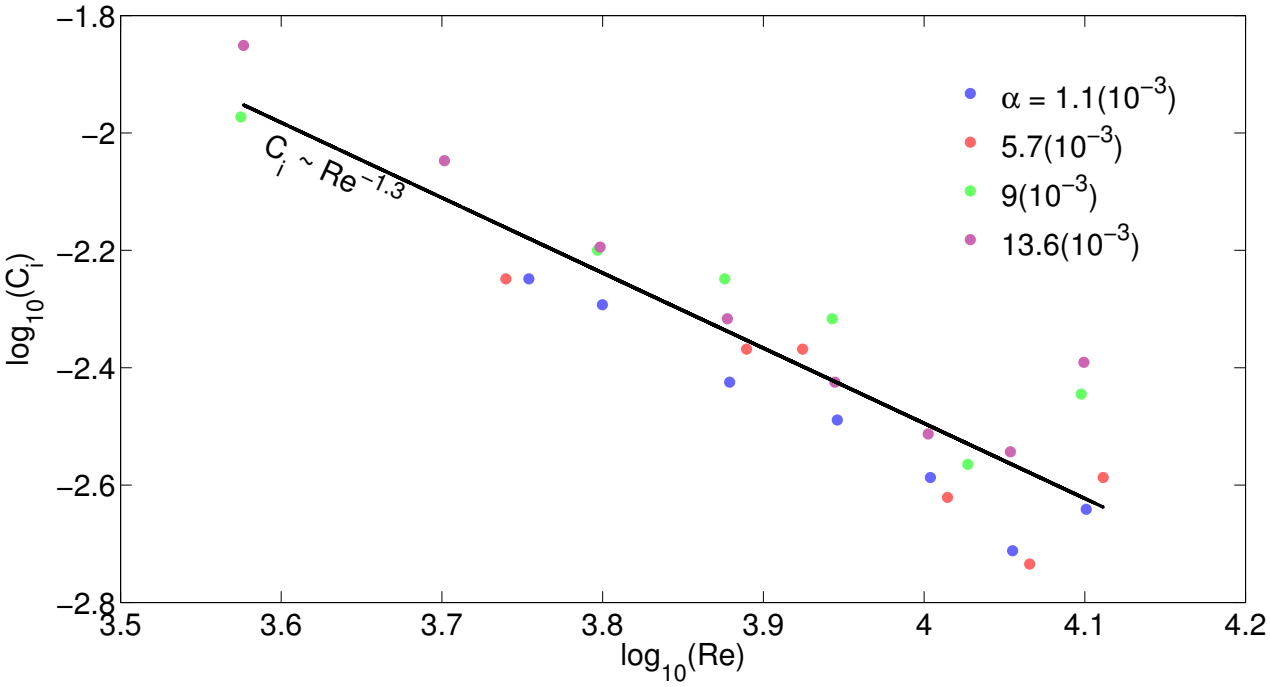

Figure 4.9: An interfacial drag coefficient inferred from a fit to the solution presented in Poggioli & Horner-Devine (2015) versus upper layer Reynolds number Re. Also shown is a power law fit to the C_i versus Re curve, indicating a dependence of C_i on $Re^{-1.3}$. Points are colored by bottom slope.

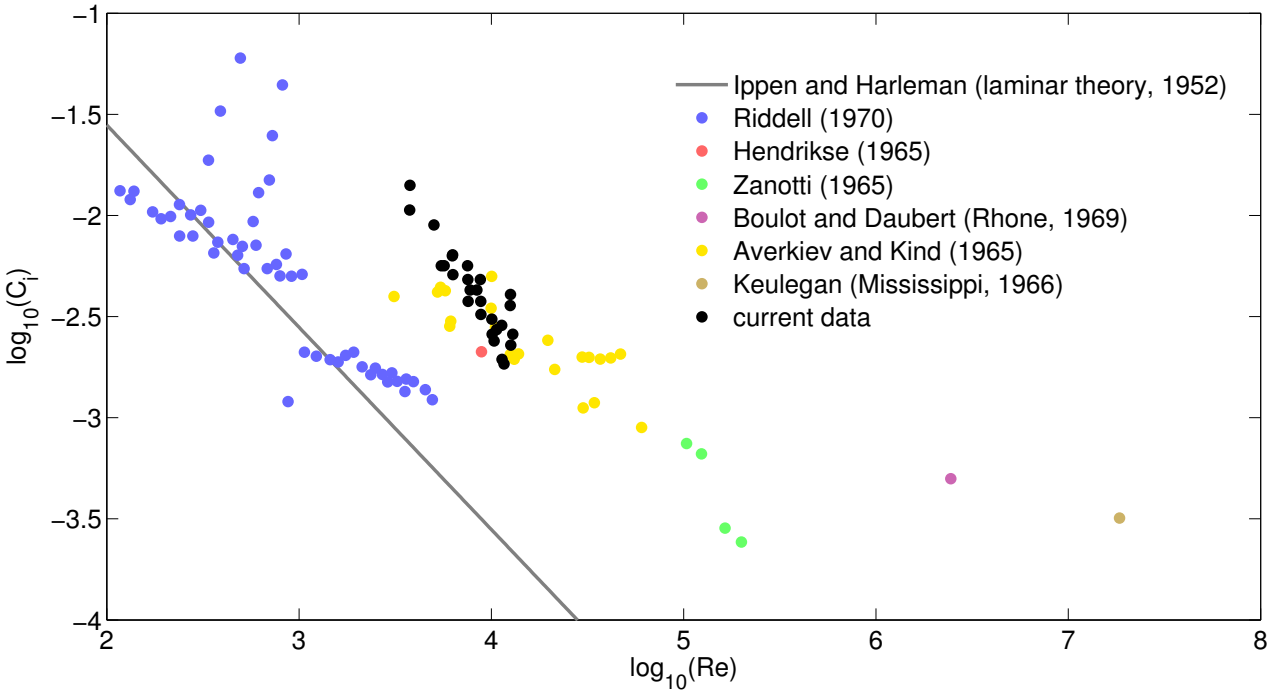

Figure 4.10: Comparison of the interfacial drag coefficient inferred in the present study (black) to data from previous laboratory and field studies, as well as the theoretical solution for laminar flow from Ippen & Harleman (1952), as compiled by Karelse *et al.* (1974, Figure 2.3).

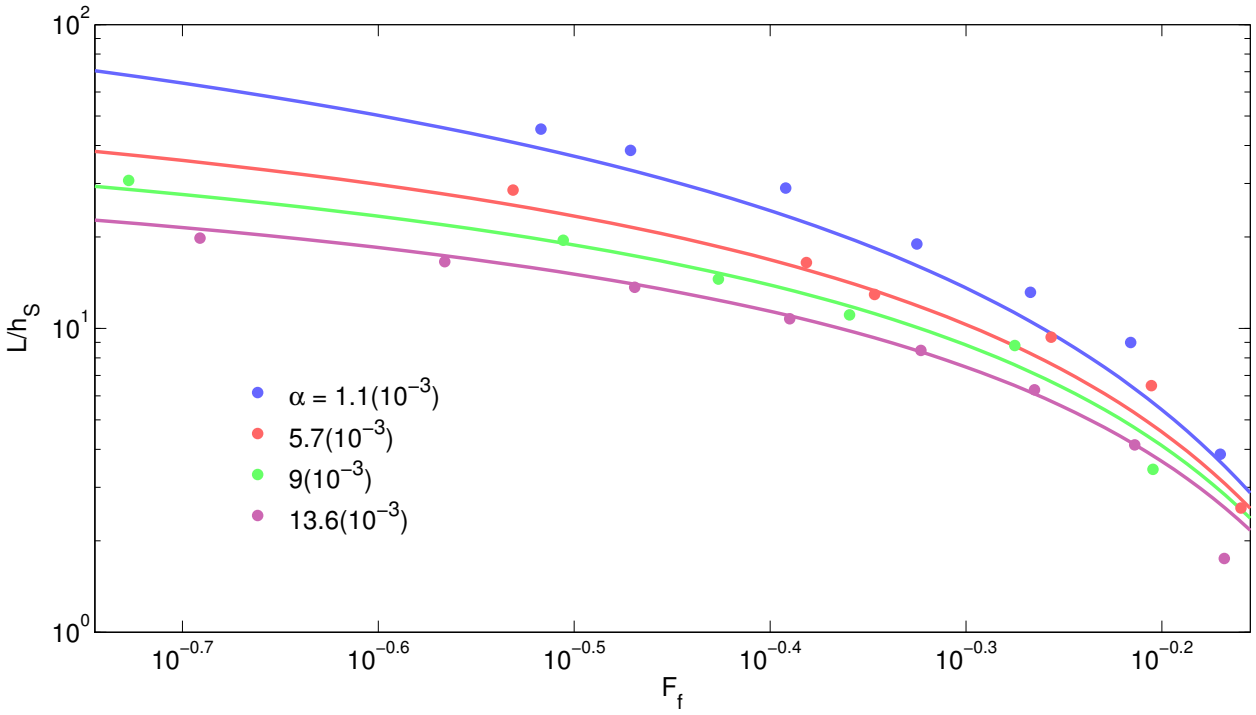

Figure 4.11: Measured L/h_S versus F_f for all four bottom slopes (points), compared to the solution of Poggioli & Horner-Devine (2015) (solid lines) using the fit of the C_i versus Re curve shown in Figure 4.9.

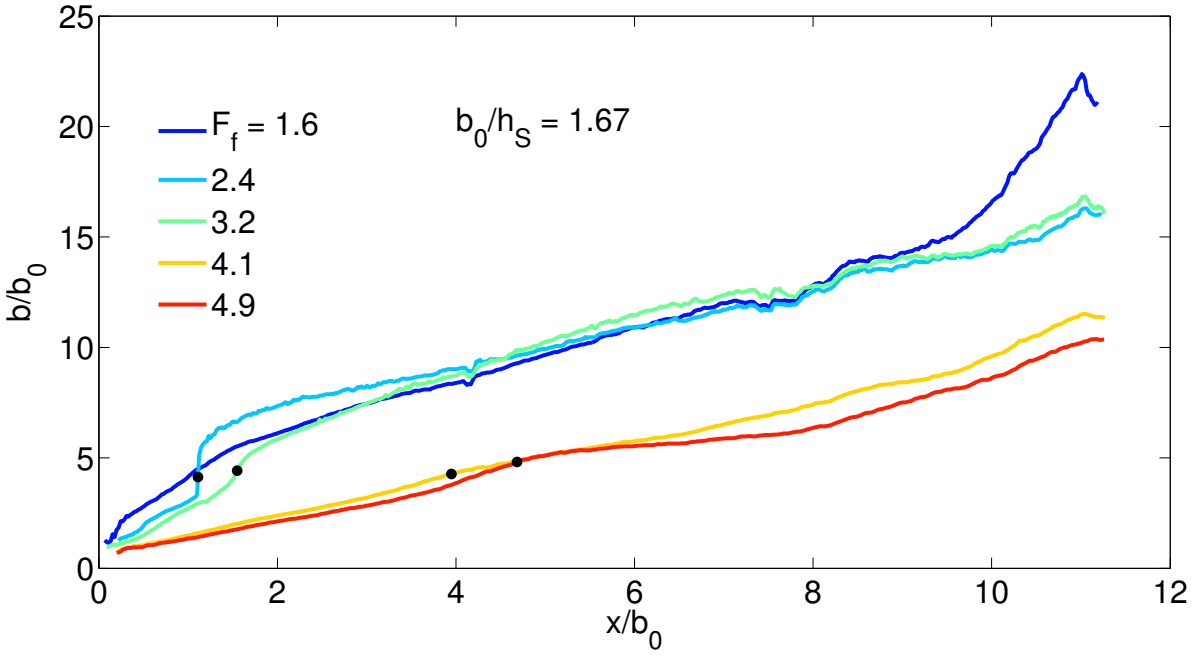

Figure 4.12: Profiles of the plume width inferred from Gaussian fits to the lateral plume thickness profile obtained at each along-shore cross-section for runs with an aspect ratio of $R_A = 1.67$. The width b was calculated as twice the standard deviation σ. The freshwater Froude number corresponding to each profile is noted in the legend. Both the offshore distance and the plume width are normalized by the initial plume width b_0. The black points indicate the location of $L_{curvature}$ for each profile (see the text), or the point where the plume transitions from divergent to convergent.

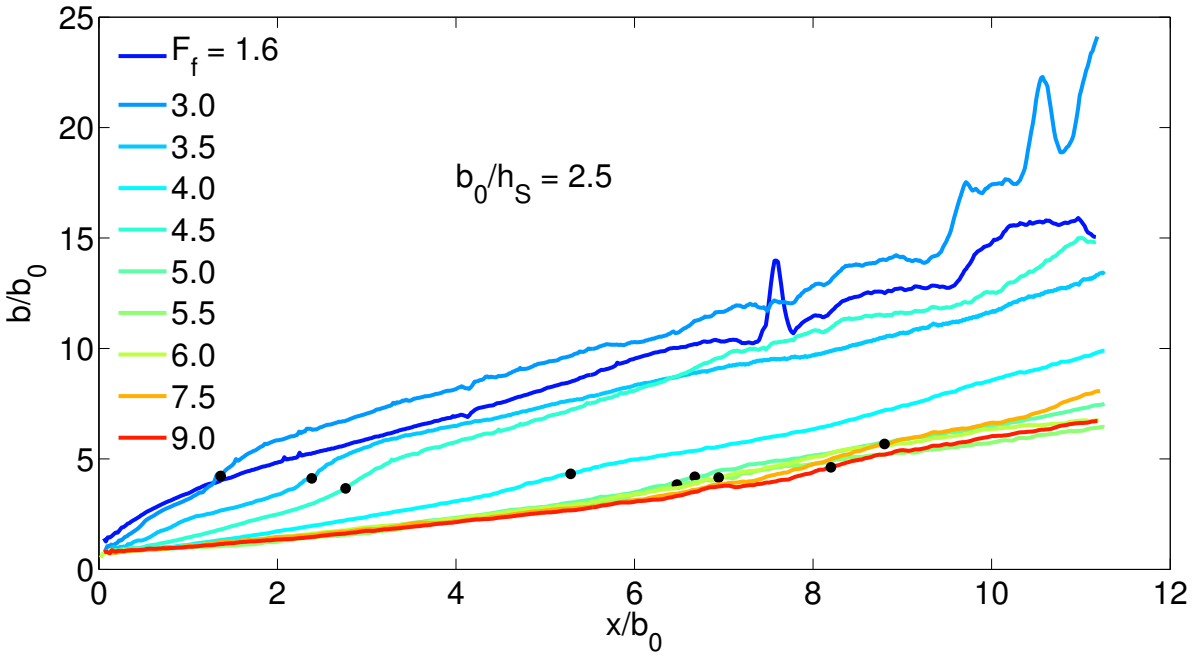

Figure 4.13: Profiles of the plume width for runs with an aspect ratio of $R_A = 2.5$. The offshore distance and width are normalized by b_0, and the black points indicate the location of $L_{curvature}$ for each profile.

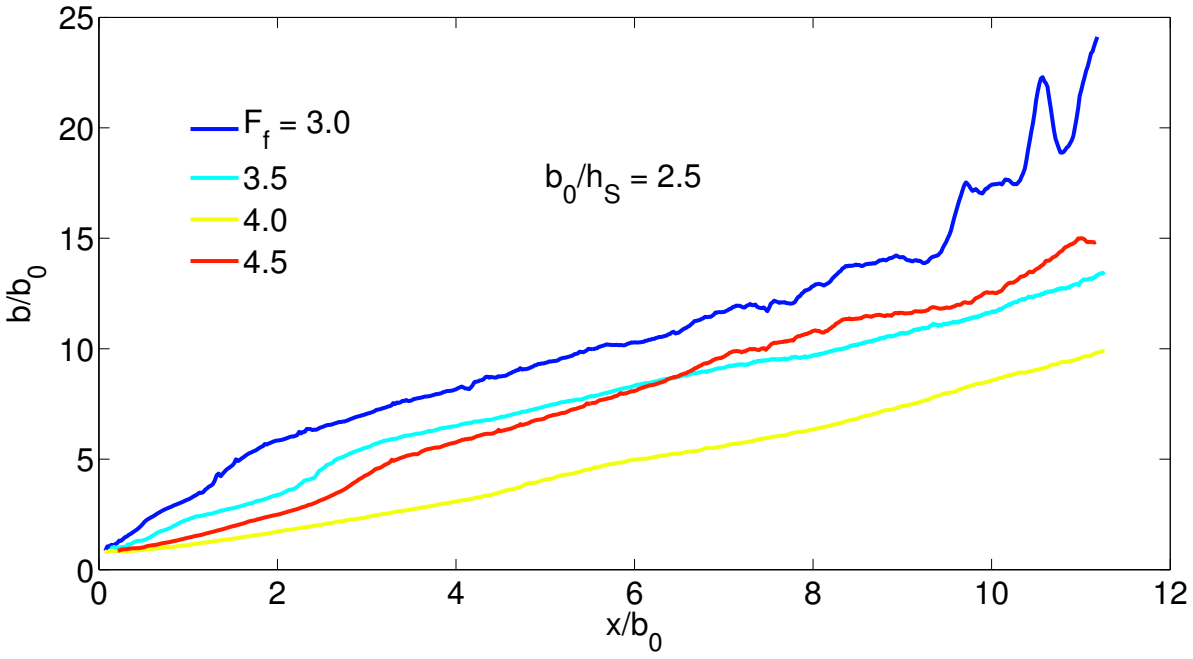

Figure 4.14: Transitional plume width profiles for runs with an aspect ratio of $R_A = 2.5$. The offshore distance and width are normalized by b_0.

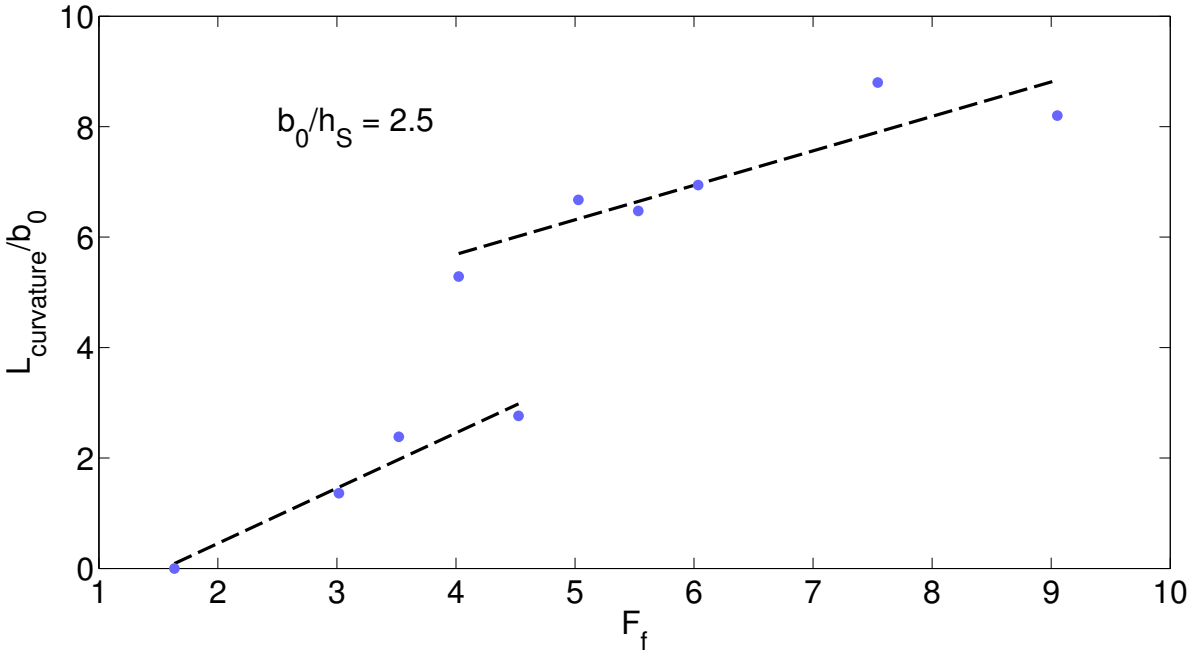

Figure 4.15: Liftoff location (inferred from $L_{curvature}$ versus freshwater Froude number. $L_{curvature}$ is normalized by b_0.

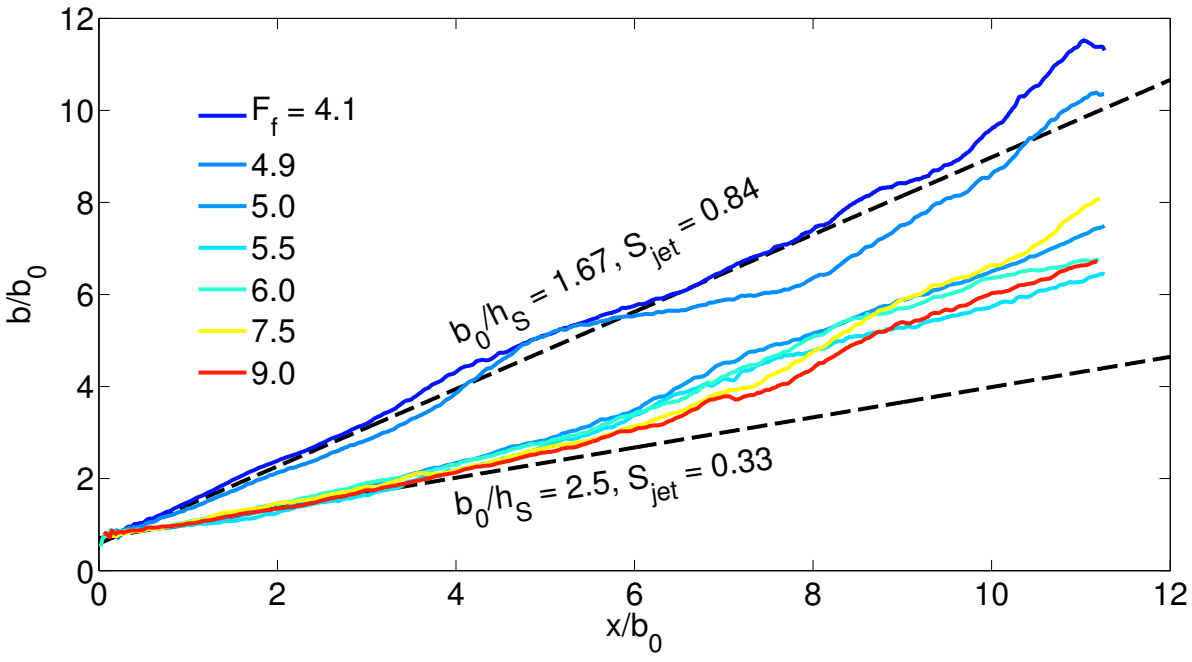

Figure 4.16: Comparison of jet spreading rate S_{jet} for $R_A = 1.67$, 2.5.

Chapter 5

CONCLUSIONS

The primary contribution of this thesis is the analytical (Chapter 2) and experimental (Chapter 4) confirmation that bottom slope accounts for the discrepancy between flat bottom theory and field observations for the sensitivity of the estuary length to river discharge in salt wedge estuaries.

Getting the intrusion length right was a necessary first step to developing a simple hydraulic model of sediment transport in the salt wedge that is appropriate for morphological contexts, where simplicity is necessary, given model times on the order of (10^3) years or more. Such a model was developed in Chapter 3, and we quantified some of the anticipated effects of salt wedge formation on the volumetric balance of sediment in the lower river. While the effect of the salt wedge on sediment export was found likely to be negligible, the salt wedge was found to have the capacity to significantly modify the volume and location of sediment deposition in shallow rivers. Furthermore, our results indicate that there is a peak in the rate of sediment deposition, and therefore in bed aggradation, in the lower river at the estuary toe. Above a critical value of the freshwater Froude number that varies with the normal flow Froude number, the peak in the depositional rate associated with the toe exceeds that associated with sediment deposition as the flow enters the backwater zone. Previous studies (Chatanantavet *et al.*, 2012; Lamb *et al.*, 2012) have suggested that the backwater length may be a geologically important length scale, possibly setting the avulsion length scale in natural systems. The results of Chapter 3 indicate that the intrusion length may, for similar reasons, be an important length scale on geological timescales.

In Chapter 4, we have also presented observations of the evolution of the plume spreading profile with freshwater Froude number. Our results corroborate theory based on the buoyancy

driven spreading of the plume for low values of F_f and suggest that the plume transitions to a jet-like outflow with a constant spreading rate driven by lateral entrainment that may remain bottom attached for a significant distance offshore. We hypothesized additionally that all subcritical plume width profiles should collapse to a single profile, since the outflow is forced to adjust to a value of the internal Froude number of 1 at the mouth. However, we were not able to process data that would have confirmed this hypothesis. Additionally, while we were able to quantify the transition from plume-like to jet-like behavior and the entrainment-driven spreading rate, these values are very likely to be highly sensitive to the outflow aspect ratio. In our experiments, as is typical, we were constrained to values of R_A on the order of unity. However, in the field, R_A is $O(100)$ to $O(1000)$. This does not alter our qualitative conclusions about the evolution of the plume with F_f; however, it is likely to dramatically alter our quantitative conclusions.

Additionally, data was taken for Chapter 4 that was intended to test the variation of the free surface elevation at the mouth with river discharge, and the influence of the river hydraulics on the plume structure. We were unable to draw any meaningful conclusions from this data due to experimental and processing difficulties, and it is was not presented in this thesis. However, this does not suggest that a signal does not exist. The variation of η_S with Q is important for quantifying the magnitude of erosion in the lower river during high discharge drawdown events, and the variation of plume structure with hydraulic state in the river may be potentially important for the river morphology community but is also of fundamental interest for our understanding of the basic science of the system. Previously, to my knowledge, no work has been done to coherently link the river and estuary hydraulics in a rigorous theoretical manner. If a signal of the river hydraulics was observed in the plume structure, this would go a long way in motivating development of theory linking the river and estuary/plume hydraulics.

I offer the following recommendations that I think are logical and necessary next steps based on the work presented in this thesis:

- Test the implications of salt wedge formation on geological time scales by implementing the model presented here in a single river system on geological time scales. An ideal candidate is the Mississippi because it is the subject of previous such study neglecting salt wedge formation (Chatanantavet *et al.*, 2012; Lamb *et al.*, 2012), it is of a very shallow grade where we expect the influence of the salt wedge to be most pronounced, and the salt wedge has been observed to intrude a distance comparable to the backwater length.

- Refined measurement of the free surface elevation in the plume during high discharge runs that accounts for the difficulties noted in Chapter 4. This would test both for any dependence of η_S on Q, as well as on F_N, a proxy for the hydraulic state of the upstream river.

- Further measurement of the plume spreading profile at subcritical and supercritical values of F_f and at different aspect ratios to determine if subcritical runs do collapse, and how sensitive the transition from plume to jet behavior and the entrainment-driven spreading rate is to aspect ratio.

- Development of theory linking the river and estuary/plume hydraulics, possible based on the work presented by Lawrence (1992), who extended the work of Armi and Farmer Armi (1986); Armi & Farmer (1986) to include variations of the free surface and the couple of barotropic and baroclinic hydraulics.

Appendix A

SEDIMENT MODEL–DERIVATION OF F_D, E, AND E_{TOE}

In this Appendix we use the model described in Section 3.3.2 to derive equations for the fraction of sediment deposited in the estuary–the deposition fraction f_D–the export of sediment to the shelf E, and the flux of sediment from the upstream river into the salt wedge E_{toe} (see Figure 3.3).

We define ξ as the vertical distance settled by a particle of settling velocity w_s. We assume that the sediment travels as a vertically uniform plug and can be characterized by a single mean settling velocity. Therefore, ξ corresponds also to the distance settled by the sediment column into the salt wedge (see Figure 3.3a). Mathematically, $w_s = D\xi/Dt$, where $D()/Dt$ indicates a material derivative, in this case a derivative following the sediment column as it is advected by the flow. The flow velocity may be written as $u = Dx/Dt$. Therefore,

$$\frac{D\xi}{Dx} = \frac{D\xi}{Dt}\frac{Dt}{Dx} = \frac{w_s}{u}. \tag{A.1}$$

We integrate from $x = -L_e$ to 0 to find the distance the sediment column has settled into the salt wedge at the mouth of the estuary:

$$\xi = \int_{-L_e}^{0} \frac{w_s}{u} dx. \tag{A.2}$$

We assume that the sediment tends to be advected by the mean flow; if it were not settling, the height of the sediment column would equal the local thickness of the freshwater layer. Therefore, the fraction of sediment that has been settled out of the water column at the mouth of the river is equal to the ratio of the distance settled by the sediment column, ξ, to the layer thickness at the mouth, $h_1 = (q^2/g')^{1/3}$ (see Section 3.2.2, Figure 3.3). We use this consideration, along with fluid continuity, $u = q/h_1$, to derive an expression for the

deposition fraction f_D in terms of an integral of the upper layer thickness:

$$f_D = w_s \left(\frac{g'}{q^5}\right)^{1/3} \int_{-L_e}^{0} h_1 dx. \tag{A.3}$$

We non-dimensionalize h_1 by h_S and x and L_e by h_S/C_i, as we did in Section **??**. We also utilize the definition of the freshwater Froude number $F_f = q/\sqrt{g' h_S^3}$. Non-dimensionalization produces

$$f_D = \frac{Ro_d}{F_f^{5/3}} \int_{-L_{e*}}^{0} h_{1*} dx_*, \tag{A.4}$$

where $Ro_d \equiv w_s/C_i\sqrt{g' h_S}$ is a scale of the ratio of the settling velocity to the friction velocity $u_f \equiv \sqrt{\tau/\rho}$ in the estuary and is here termed the densimetric Rouse number (see Section 3.3.2). Equation A.4 gives the fraction of sediment entering at the toe that is deposited by the time the flow reaches the mouth; if it is instead integrated to an arbitrary point x, it can be used to calculate the profiles of sediment flux and deposition over the estuary. Since a deposition fraction greater than one is not meaningful, Equation A.4 is properly written

$$f_D = \min\left(\frac{Ro_d}{F_f^{5/3}} \int_{-L_{e*}}^{0} h_{1*} dx_*, 1\right). \tag{A.5}$$

In the following, as in the rest of the paper, we normalize all fluxes by the normal flow specific sediment flux, $(q_{sed})_N$. To determine the export to the shelf E, we must multiply $1 - f_D$ by the flux into the estuary E_{toe}. We can find E_{toe} by applying the Engelund & Hansen (1967) formula (Equation 3.13) at the toe of the salt wedge:

$$E_{toe} = \left(\frac{h_1^{toe}}{h_N}\right)^{-5} = E_0 \left(h_{1*}^{toe}\right)^{-5}, \tag{A.6}$$

where $E_0 = (h_S/h_N)^{-5}$ is the sediment flux to the shelf in the absence of estuary formation (found using Equation 3.13), and h_{1*}^{toe} is the water depth at the toe normalized by h_S. In general, a subscript 0 denotes a quantity calculated by neglecting estuary formation. The export to the shelf is therefore:

$$E = (1 - f_D)E_{toe} = (1 - f_D)E_0(h_{1*}^{toe})^{-5}. \tag{A.7}$$

BIBLIOGRAPHY

Armi, L. 1986. The hydraulics of two flowing layers with different densities. *J. Fluid Mech.*, **163**, 27–58.

Armi, L., & Farmer, D. M. 1986. Maximal two-layer exchange through a contraction with barotropic net flow. *J. Fluid Mech.*, **164**, 27–51.

Averkiev, A. G., & Kind, K. J. 1965. *Etudes Expeimentales de Certaines Caracteristique des Courants de Densit.* AIRH congres, Leningrad.

Blum, M. D., & Törnqvist, T. E. 2000. Fluvial responses to climate and sea-level change: A review and look forward. *Sedimentology*, **47**, 2–48.

Bresse, J. A. C. 1860. *Cours de Mécanique Appliquée: Hydraulique.* 2 edn. Mallet-Bachelier, Paris.

Chatanantavet, P., Lamb, M. P., & Nittrouer, J. A. 2012. Backwater controls on avulsion location in deltas. *Geophys. Res. Lett.*, **39**.

Chatwin, P. C. 1976. Some remarks on the maintenance of the salinity distribution in estuaries. *Estuarine Coastal Mar. Sci.*, **4**, 555–566.

Chow, V. T. 1959. *Open-Channel Hydraulics.* McGraw-Hill.

Dawson, W. A., & Tilley, L. J. 1972. *Measurement of salt-wedge excursion distance in the Duwamish River Estuary, Seattle, Washington, by means of the dissolved-oxygen gradient.* Water Supply Paper 1873-D.

Engelund, F., & Hansen, E. 1967. *A Monograph on Sediment Transport in Alluvial Streams.* Teknisk Forlag, Copenhagen.

Fugate, D. C., & Chant, R. J. 2005. Near-bottom shear stress in a small, highly stratified estuary. *J. Geophys. Res.*, **110**.

Geyer, W. R. 1993. The importance of suppression of turbulence by stratification on the estuarine turbidity maximum. *Estuaries*, **16**.

Geyer, W. R., & Farmer, D. M. 1989. Tide-induced variation of the dynamics of a salt wedge estuary. *J. Phys. Oceanogr.*, **19**, 1060–1072.

Geyer, W. R., & MacCready, P. 2014. The estuarine circulation. *Annu. Rev. Fluid Mech.*, **46**, 175–197.

Geyer, W. R., & Ralston, D. K. 2011. The dynamics of strongly stratified estuaries. *Pages 37–51 of:* Wolanski, E., & McLusky, D. (eds), *Water and Fine Sediment Circulation*, 1 edn. *Treatise on Estuarine and Coastal Science*, vol. 2. Elsevier.

Geyer, W. R., Hill, P. S., & Kineke, G. C. 2004. The transport, transformation and dispersal of sediment by buoyant coastal flows. *Cont. Shel Res.*, **24**, 927–949.

Harleman, D. R. F. 1961. Stratified flow. *Pages **26**–1–**26**–21 of:* Streeter, V. L. (ed), *The Handbook of Fluid Dynamics*. McGraw-Hill.

Hendrikse, M. 1965. *The effect of resistance bars upon an arrested salt wedge*. M.Phil. thesis, Mass. Inst. Tech.

Hetland, R. D. 2010. The effects of mixing and spreading on density in near-field river plumes. *Dyn. Atmos. Oceans*, **49**, 37–53.

Hickey, B. M., Kudela, R.M., Nash, J. D., Bruland, K. W., Peterson, W. T., MacCready, P., Lessard, E. J., Jay, D. A., Banas, N. S., Baptista, A. M., Dever, E. P., Korso, P. M., Kilcher, L. K., Horner-Devine, A. R., Zaron, E. D., McCabe, R. M., Peterson, J. O., Orton, P. M., Pan, J., & Lohan, M. C. 2010. River Influences on Shelf Ecosystems: Introduction and synthesis. *J. Geophys. Res.*, **115**.

Hogg, A. McC., & Ivey, G. N. 2003. The Kelvin-Helmholtz to Holmboe instability transitioni n stratified exchange flows. *J. Fluid Mech.*, **477**, 339–362.

Hordoir, R., Polcher, J., Brun-Cottan, J. C., & Madec, G. 2008. Towards a parameterization of river discharges into ocean general circulation models: A closure through energy conservation. *Clim. Dyn.*, **31**.

Horner-Devine, A. R., Jay, D. A., Orton, P. M., & Spahn, E. Y. 2009. A conceptual model of the strongly tidal Columbia River plume. *J. Mar. Sys.*, **78**, 460–475.

Horner-Devine, A. R., Hetland, R. D., & MacDonald, D. G. 2015. Mixing and transport in coastal river plumes. *Ann. Rev. Fluid Mech.*, **47**, 569–594.

Hotchkiss, R. H., & Parker, G. 1991. Shock fitting of aggradational profiles due to backwater. *J. Hydraul. Eng.*, **117**, 1129–1144.

Ippen, A. T., & Harleman, D. R. F. 1952. Steady-State Characteristics of Subsurface Flow. *Pages 79–93 of:* Ippen, A. T. (ed), *Estuary and Coastline Hydrodynamics*, 1 edn. McGraw-Hill.

Jerolmack, D. J. 2009. Conceptual framework for assessing the response of delta channel networks to Holocene sea level rise. *Quat. Sci. Rev.*, **28**, 1786–1800.

Karelse, M., Vreugendhil, C. B., Delvigne, G. A. L., & Breusers, H. N. C. 1974. *Momentum and mass transfer in stratified flows.* Tech. Report. R880. Delft Hydraul. Lab., Delt, Netherlands.

Keulegan, G. H. 1957. *Form characteristics of arrested saline wedge.* NBS Report 5482.

Keulegan, G. H. 1966. The mechanism of an arrested saline wedge. *Pages 546–574 of:* Ippen, A. T. (ed), *Estuary and Coastline Hydrodynamics.* McGraw-Hill.

Kilcher, L., Nash, J. D., & Moum, J. N. 2012. The role of turbulence stress divergence in decelerating a river plume. *J. Geophys. Res.*, **117**.

Kostaschuk, R. A., Church, M. A., & Luternauer, J. L. 1992. Sediment transport over salt-wedge intrusions: Fraser River estuary, Canada. *Sedimentology*, **39**, 305–317.

Lamb, M. P., Nittrouer, J. A., Mohrig, David, & Shaw, John. 2012. Backwater and river plume controls on scour upstream of river mouths: Implications for fluvio-deltaic morphodynamics. *J. Geophys. Res.*, **117**.

Lane, E. W. 1957. *A Study of the Shape of Channels Formed by Natural Streams Flowing in Erodible Material*. U.S. Army Corps of Eng., Mo. River Div., Omaha, Nebr.

Lawrence, G. A. 1992. The hydraulics of steady two-layer flow over a fixed obstacle. *J. Fluid Mech.*, **254**, 605–633.

Lerczak, J. A., Geyer, W. R., & Ralston, D. K. 2009. The temporal response of the length of a partially stratified estuary to changes in river flow and tidal amplitude. *J. Phys. Oceanogr.*, **39**, 915–933.

MacCready, P., & Banas, N. S. 2011. Residual circulation, mixing, and dispersion. *Pages 75–89 of:* Wolanski, E., & McLusky, D. (eds), *Water and Fine Sediment Circulation*, 1 edn. *Treatise on Estuarine and Coastal Science*, vol. 2. Elsevier.

MacDonald, D. G., & Geyer, W. R. 2004. Turbulent energy production and entrainment at a highly stratified estuarine front. *J. Geophys. Res.*, **109**.

McCabe, R. M., MacCready, P., & Hickey, B. M. 2009. Ebb-tide dynamics and spreading of a large river plume. *J. Phys. Oceanogr.*, **39**.

McKeon, M. A., Horner-Devine, A. R., & Giddings, S. N. 2014. Seasonal changes in structure and dynamics in an urbanized salt wedge estuary. *Estuaries Coasts*. In revision.

Monismith, S. G., Kimmerer, W., Stacey, M. T., & Burau, J. R. 2002. Structure and flow-induced variability of the subtidal salinity field in northern San Francisco Bay. *J. Phys. Oceanogr.*, **32**, 3003–3019.

Nash, D. B. 1994. Effective sediment-transporting discharge from magnitude-frequency analysis. *J. Geol.*, **102**, 79–95.

Nijs, M. A. J. De, Winterwerp, J. C., & Pietrzak, J. D. 2010. The effects of the internal flow structure on SPM entrapment in the Rotterdam Waterway. *J. Phys. Oceanogr.*, **40**.

Poggioli, A. R., & Horner-Devine, A. R. 2015. The sensitivity of salt wedge estuaries to channel geometry. *J. Phys. Oceanogr.* in press.

Pratt, L. J. 1986. Hydraulic control of sill flow with bottom friction. *J. Phys. Oceanogr.*, **16**, 1970–1980.

Rahmstorf, S. 1995. Bifurcations of the Atlantic thermohaline circulation in response to changes in the hydrologic cycle. *Nature*, **378**.

Ralston, D. K., Geyer, W. R., & Lerczak, J. A. 2010. Structure, variability, and salt flux in a strongly forced salt wedge estuary. *J. Geophys. Res.*, **115**.

Rattray, Jr., M., & Mitsuda, E. 1974. Theoretical analysis of conditions in a salt wedge. *Est, Coast. Mar. Sci.*, **2**, 375–394.

Riddell, J. F. 1970. Densimetric exchange flow in rectangular channels, IV The arrested salt wedge. *La Houille Blanche*, **25**, 317–329.

Savenije, H. H. G. 2005. *Salinity and Tides in Alluvial Estuaries.*

Schijf, J. B., & Schönfeld, J. C. 1953. Theoretical considerations on the motion of salt and fresh water. *Pages 321–333 of: Proc. Minnesota Int. Hydraul. Con.* Univ. Minn., Minneapolis, MN.

Snow, R. S., & Slingerland, R. L. 1987. Mathematical modeling of graded river profiles. *J. Geol.*, **95**, 15–33.

Sorgard, E. 1991. A numerical, three-layered, stationary salt wedge model. *J. Geophys. Res.*, **96**, 12739—12754.

Sorgard, E., Martinsen, T., & Aas, E. 1990. Drag coefficient at a stationary salt wedge. *J. Geophys. Res.*, **95**, 7337–77345.

Stommel, H., & Farmer, H. G. 1952. Abrupt change in width in two-layer open channel flow. *J. Mar. Res.*, **11**, 205–214.

Sturm, T. W. 2010. *Open Channel Hydraulics*.

Syvitski, J. P. M, & Saito, Y. 2007. Morphodynamics of deltas under the influence of humans. *Global Planet. Change*, **57**, 261–282.

Syvitski, J. P. M., Kettner, A. J., Overeem, I., Hutton, E. W. H., Hannon, M. T., Brakenridge, G. R., Day, J., Vörösmarty, C., Saito, Y., Giosan, L., & Nicholls, R. J. 2009. Sinking deltas due to human activities. *Nat. Geosci.*, **2**, 681–686.

UN-OCEANS. *UN Atlas of the Oceans: Human Settlements on the Coast*. Available online at http://www.oceansatlas.org/servlet/CDSServlet?status=ND0xODc3JjY9ZW4mMzM9KiYzNz1rb3M .

Valle-Levinson, A. 2011. Classification of estuarine circulation. *Pages 37–51 of:* Wolanski, E., & McLusky, D. (eds), *Water and Fine Sediment Circulation*, 1 edn. *Treatise on Estuarine and Coastal Science*, vol. 1. Elsevier.

Ward, P. 1976. Seasonal salinity changes in the Fraser River estuary. *Can. J. Civ. Eng.*, **3**, 342–348.

Wright, L. D. 1977. Sediment transport and deposition at river mouths–Synthesis. *Geol. Soc. Am. Bull.*, **88**, 857–868.

Yuan, Y., & Horner-Devine, A. R. 2013. Laboratory Investigations of the Impact of Lateral Spreading on Buoyancy Flux in a River Plume. *J. Phys. Oceanogr.*, **43**, 2588–2610.

Yuan, Y., Avener, M. A., & Horner-Devine, A. R. 2011. A two-colored optical method for determining layer thickness in two interacting buoyant plumes. *Exp. Fluids*, 1235–1245.

Zanotti, A. 1965. Il cuneo salino nei canali cou sfocio in mare. *Energia Elettrica*, **7**, 462–473.